Toward Characterization of the Epoch of Reionization with Redshifted 21 cm One-point Statistics

by

Piyanat Kittiwisit

A Dissertation Presented in Partial Fulfillment
of the Requirements for the Degree
Doctor of Philosophy

Approved April 2019 by the
Graduate Supervisory Committee:

Judd D. Bowman, Chair
Christopher E. Groppi
Nathaniel R. Butler
Daniel C. Jacobs
Evan Scannapieco

ARIZONA STATE UNIVERSITY

May 2019

ABSTRACT

One of the most fundamental questions in astronomy is how the Universe evolved to become the highly structured system of stars and galaxies that we see today. The answer to this question can be largely uncovered in a relatively unexplored period in the history of the Universe known as the Epoch of Reionization (EoR), where radiation from the first generation of stars and galaxies ionized the neutral hydrogen gas in the intergalactic medium. The reionization process created "bubbles" of ionized regions around radiating sources that perturbed the matter density distribution and influenced the subsequent formation of stars and galaxies. Exactly how and when reionization occurred are currently up for debate. However, by studying this transformative period we hope to unravel the underlying astrophysics that governs the formation and evolution of the first stars and galaxies.

The most promising method to study reionization is 21 cm tomography, which aims to map the 3D distribution of the neutral hydrogen gas using the 21 cm emission lines from the spin-flip transition of neutral hydrogen atoms. Several radio interferometers operating at frequencies below 200 MHz are conducting these experiments, but direct images of the observed fields are limited due to contamination from astrophysical foreground sources and other systematics, forcing current and upcoming analyses to be statistical.

In this dissertation, I studied one-point statistics of the 21 cm brightness temperature intensity fluctuations, focusing on how measurements from observations would be biased by different contaminations and instrumental systematics and how to mitigate them. I develop simulation tools to generate realistic mock 21 cm observations of the Hydrogen Epoch of Reionization Array (HERA), a new interferometer being constructed in the Karoo desert in South Africa, and perform sensitivity analysis of

the telescope to one-point statistics using the mock observations. I show that HERA will be able to measure 21 cm one-point statistics with sufficient sensitivity if foreground contaminations can be sufficiently mitigated. In the presence of foreground, I develop a rolling foreground avoidance filter technique and demonstrate that it can be used to obtain noise-limited measurements with HERA. To assess these techniques on real data, I obtain measurements from the legacy data from the first season observation of the Murchison Widefield Array (MWA) and perform additional high-precision radio interferometric simulations for comparison. Through these works, I have developed new statistical tools that are complementary to the power spectrum method that is currently the central focus of the majority of analyses. In addition to confirming power spectrum detections, one-point statistics offer additional information on the distribution of the 21 cm fluctuations, which is directly linked to the astrophysics of structure formation.

In the loving memory of my father Taninchai (1957–2015), whose never-ending curiosity, generosity, and love of food have always been parts of me.

To my beloved mother Supapan, whose perseverance and open-mindedness have taught me how to overcome hardship as I search for the remaining me.

And to my sister Issaraporn, whose compassion and spirit of adventure are my inspiration for the future.

ACKNOWLEDGMENTS

This dissertation is the culmination of my work over several years, and I could not have done it without the love and support of many people to whom I owe many thanks. First, I would like to thank my family and relatives, especially my parents, Taninchai and Supapan, and sister Issaraporn, who have always supported me with love and kindness since I moved from home 18 years ago to pursue a study, and later a career, in science.

I would like to thank my academic advisor, Prof. Judd Bowman, for giving me an invaluable opportunity to become a part of this cutting-edge research and for patiently teaching me the art of radio astronomy. I can only hope to contribute to science as much as you have already done.

I am deeply in debt to Prof. Christopher Groppi, who is also one of my PhD committee members. Chris, as how he would like to be called, holds an amazing aptitude for understanding the struggle of the graduate students. His guidance and encouragement helped me to overcome many difficulties beyond the technical aspects of research and enabled me to be confident in myself.

Thank you to my other PhD committee members, Prof. Daniel Jacobs for saying things that need to be said when no one else was willing to say them, Prof. Evan Scannapieco for giving me an opportunity to discover radio astronomy, and Prof. Nathaniel Butler for continual support. I am also very thankful for the warm support from the faculty and staff in SESE: Paul Scowen, Phil Mauskopf, Cassie Bowman, Karen Knierman, Enrique Vivoni, Patrick Young, Steve Desch, Lindy Elkins-Tanton, Becca Dial, Becky Polley, Meg Hufford, and Ric Alling.

Thank you to the postdocs whom I have worked with – Adam Beardsley, Nithya Thyagarajan, and Steven Murray – for always being patient and helpful with my endless

questions. It has also been a pleasure to work with the other members of the Low-frequency Cosmology Lab past and present: Matt Kolopanis, Nivedita Mahesh, Tom Mozdzen, Mru Krishna, Bharat Gehlot, Raul Monsalve, and Jackie Monkiewicz. I am also greatly appreciative for the opportunity to work with the HERA and MWA collaborations as a whole.

I am extremely grateful to have found a very supportive network of friends and colleagues in Arizona. Thank you to Caleb Wheeler and Natalie Hinkel for being my first two and true friends in the United State. Thank you to Kimberly Ward-Duong, Brian Svoboda, and Kristina Davis for always being kind and encouraging. Thank you to Emilie Dunham, Nari Miller, Kristen Whitney, Sam Gordon, Edward Buie, and Marko Neric for warmly welcoming me and kindly listening to my worry during the tough time. Every moment that I have spent with everyone of you – the meals that we have cooked and shared together, the hikes that we have finished or gotten lost together, the conquering of Mt. Humphreys, the Saturday coffee before the looming deadline at Gold Bar, the weird sci-fi movie, the camp fire in a 70-degree whether – was a joy of my daily life and my true happiness.

I am also very lucky to have known a small but generous and kind group of Thais in Arizona. Thank you P'Own, P'Lek, P'Chok, P'Pik, P'Jib, P'Tong, P'Kwan, P'Chot, P'Re, P'Ja, Metin, Ceyda, Ada, Caitlin, P'Jung, Mike, Justin, Jayden, and Gift for friendship and generous support. Also, thank you to Tarn and Miki for keeping in touch.

Lastly, I am very grateful to have been a Thai scholar under the Development and Promotion of Science and Technology Talents Project (DPST), who has provided me with generous funding, scientific network, and opportunities to study science. I am looking forward to contribute back to scientific development of our home country.

TABLE OF CONTENTS

LIST OF TABLES

LIST OF FIGURES

PREFACE

Driven by the desire to understand the underlying physics behind the formation and evolution of the first stars and galaxies, over the past two decades astronomers have been looking for a way to study the Epoch of Reionization (EoR), an era where radiation from these first-generation of luminous objects ionized and transformed the Universe into its current transparent state. The early development in the EoR study can be traced back to a few theoretical works in the late 1990s, which proposed that the EoR can be directly observed by mapping the 21 cm emission lines from the neutral hydrogen gas at frequency below 200 MHz. By the end of the 2000s, three radio interferometers operating in that frequency range have been built with primary goals to probe this signal.

The beginning of a research project that later developed into this dissertation can be traced back to approximately around the time of the first light of these instruments. Around August of 2011, I have just finished my summer research and study in Germany, where I learned about radio astronomy for the first time. When I got back to Tempe, I received an email from Prof. Judd Bowman asking if I would be interested in doing my PhD research in radio astronomy. I was a young graduate student looking for a project, and he was a new faculty member looking for a graduate student. I walked into Judd's office, and he handed me a research proposal that he was a co-investigator, which was just funded. I remember he said that this was going to be a challenging project with perhaps 50/50 chance of success – he was not joking. I had to confess that I did not understand much of the significance of the project or

the science behind it, but I took Judd's offer, partly because I desperately needed a project.

Our goal at the time was to develop a template of realistic mock observations of the EoR and supplied it to other scientists who were developing statistical analysis for this data. Despite, I very much enjoyed learning Python, writing codes, and looking at fuzzy images. About two years into the projects, I was able to patch together a software pipeline that generate a movie of the mock observations, with galaxies flying across the sky. I was overjoyed but also realized that our goal was not going to be succeeded as the calculation showed that will take tens of years to simulate the mock observations that we wanted.

That was when I forced myself to also undertake the role of a theorist, performing one-point statistical analysis on the data from the simulation that I developed. The following three years after that were very much struggles as my knowledge on the underlying science and technical aspects of radio astronomy was still minimal, and statistics, let alone mathematic, had never been my strong point. At the same time, I started to feel disconnected as my focus had shifted to something different from the focus of our research group. Then, my first paper was rejected.

But because of these challenges, I had developed a niche in one of the most cutting-edge field of research in astronomy, studying problems that lie at the boundaries of astrophysical theory, observation, and statistics. This dissertation will take you through the journey of this highly interdisciplinary problem.

Chapter 1

INTRODUCTION

In 1927, Belgian astronomer and Catholic priest Georges Lemaître proposed a theory based on Albert Einstein's general theory of relativity that the Universe might be expanding. He subsequently showed in 1931 that this expansion could be traced back in time to an originating single point at a finite time in the past with infinite temperature and density – the singularity. Lemaître's theory is what later became known as the Big Bang theory for the origin of the Universe. Immediately after the Big Bang, the Universe would have undergone a rapid expansion and, by about 370,000 years, its temperature would have decreased below 3000 K to allow electrons, protons and neutrons to recombine into the primordial baryonic matter that consisted of approximately 75% hydrogen and 25% helium. This event would decouple the photons from the rest of the baryons, allowing them to propagate freely into the intergalactic medium (IGM) as the cosmic microwave background radiation (CMB). To the present-day observer, this radiation would appear to come from a spherical surface with a radius equal to the distance that the photons had travelled since they was last scattered when the hydrogen and helium were recombined, often known as the last scattering surface. In 1964, Arno Penzias and Robert Wilson, American radio astronomers who were working at Bell Lab at the time, discovered an excess microwave signal in their satellite communication system that can be detected with a fixed amplitude and frequency from any direction of the sky at any time. This signal was later confirmed to be the CMB. Penzias and Wilson's discovery not only provided an evidence for the Big Bang theory but also marked the beginning of the field of observational cosmology.

Today, advancement in telescope technology and engineering have allowed astronomers to measure the CMB and obtain constraints on the cosmological parameters with unprecedented precision through satellite-based microwave observatories such as COBE, WMAP and recently Planck. Large optical and infrared ground-based observatories, as well as the Hubble space telescope, have also provided detailed observation of galaxies and traced their evolution back in time from today to as early as 700 million years after the Big Bang. However, the period between 370,000 to 700 million years after the Big Bang remained unexplored. Observations have shown that the present-day Universe consists of a highly structured system of stars of galaxies, whereas the CMB observations show smooth fluctuations of matter density at the last scattering surface. Clearly, the Universe must have evolved in someway from that primordial density fluctuations into stars and galaxies that we see today during those unexplored million of years.

The cosmological epoch that immediately followed the release of the CMB at the surface of the last scattering is known as the Dark Ages. The decoupling of the CMB photons from the baryons left the IGM with no other sources of radiation and ushered the Universe into a period of darkness that consisted only of dark matter and primordial baryonic matter formed during the recombination. The primordial matter density field during the Dark Ages is predicted to obey Gaussian statistics – consisting of many small underdense and overdense regions with smooth transition between them and an overall density distribution that agrees with the standard normal probability curve. Only a few basic processes contributed to the evolution of the Universe during the Dark Ages: its expansion, the recombination of electrons and protons, the interaction between the CMB photons and the residual electrons, and gravity. Gravity would pulled matter toward the overdense regions as the Universe expanded. The

overdense regions would become incrementally denser and bigger, but still relatively compact in comparison to the underdense regions that would become less dense and get bigger as they were losing matter. This run-away process perturbed the density field, introducing non-Gaussianity to the matter density fluctuations. Over time, gravity would win over the counteracting force from the expansion of the Universe, causing the regions to collapse further and heat up. Eventually, they would become dense and hot enough to engage nuclear fusion of hydrogen. The first luminous objects formed through this mechanism and reintroduce non-CMB radiation to the Universe. This brief period during the formation of the first stars and galaxies are colloquially named the Cosmic Dawn, and it marks the beginning of the subsequent transitional epoch that span significant portion of the cosmic timeline.

1.1 The Epoch of Reionization

The first generation of objects that formed out of the collapsing matter density field are predicted to be short lived, massive stars or small quasars powered by accreting black holes. These objects emitted ultraviolet radiation that is strong enough to ionize the neutral hydrogen gas, creating ionized "bubbles" around the radiating sources. As more stars and galaxies were formed, ionized bubbles around neighboring sources grow and merge with each other and gradually fill the entire volume of the Universe, transforming gas in the IGM from neutral to ionized. This process is called the cosmic reionization, and the era during which it occurred is called the Epoch of Reionization (EoR). Figure 1 show an artistic rendering of the reionization process.

During EoR, astrophysics of gas and radiation became important. The era, thus, holds great details for answers to questions related to the formation of the first gen-

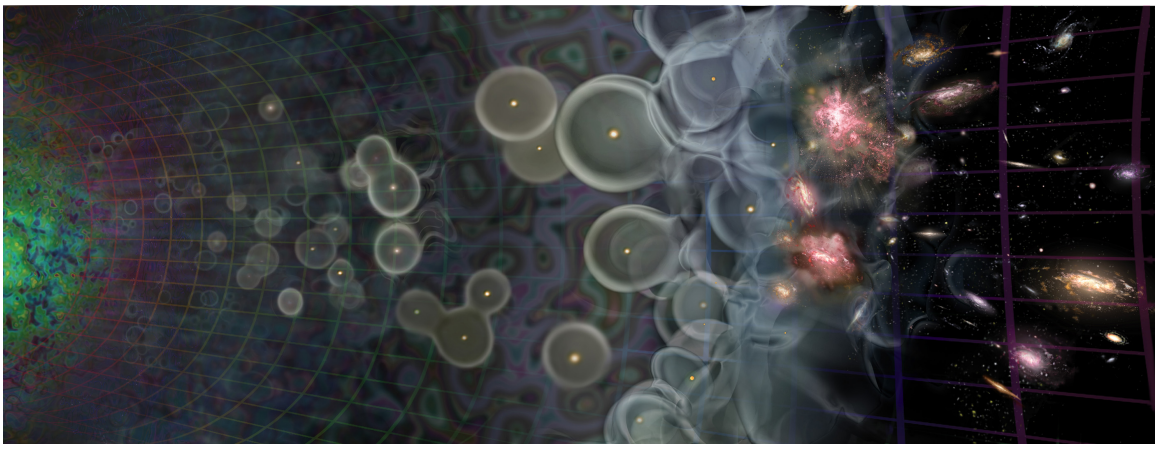

Figure 1. Artistic illustration of the cosmic timeline from the epoch of the last scattering of the CMB (left) through the modern-day galaxies (right). The reionization process during the EoR is illustrated as bubbles of ionized hydrogen surrounding the first stars and galaxies as the radiation sources. As more galaxies of the sources were formed, the bubble grow and merged and eventually ionized the whole IGM. The EoR, thus, contain crucial information in understanding the formation and evolution of stars and galaxies. Reprinted from Loeb (2006).

eration of stars and galaxies. Through which processes did the first stars form? How massive were they, and do fossils remain in the local Universe? When did heavy elements first form, and what processes distributed them? Did large-scale structured formed in a hierarchical manner as in the low redshift Universe? These are some of the many questions that could be answered by studying the EoR.

Although the EoR has never been observed, there are two primary sources of evidences on the existence of the epoch: (1) the measurement of optical depth for Thomson scattering from the CMB anisotropy fluctuations and (2) observations of the Lyman-α forest in the spectra of high-redshift quasars.

Although the mean temperature the CMB is isotropic at 2.725 K, there exists anisotropy fluctuations at tens of μK scale buried underneath the mean temperature. These anisotropies manifest the characteristic bumps in the CMB angular power spectrum, and they are sensitive to the Thomson scattering of the CMB photons by free

electrons along the line of sight. If reionization ended early, there would be more free electrons in the IGM between the surface of the last scattering and the present-day observers, increasing the optical depth for Thompson scattering. More CMB photons would be scattered out of the line of sight before they could reach the observer. This would erase small-scale anisotropies and generates large-scale polarization anisotropies in the CMB angular power spectrum. In other words, the CMB can provide limits on the epoch and duration of reionization by providing a measurement of the integrated optical depth to Thomson scattering. Recent measurements by the Planck satellite yield a very low value of the optical depth for Thompson scattering ($\tau \sim 0.056 \pm 0.007$), indicating that reionization is still progressing at $z \sim 7.9$ (Planck Collaboration et al., 2018).

The state of the IGM can also be studied through the analysis of the Lyman-α forest in the spectra of a background quasar or a young galaxy. This is an absorption phenomenon that occurs when UV photons with energy higher than 10.196 eV from a background object is being continuously redshifted as they propagate through the IGM and, at some intermediate point along the line of sight, reach 1216 Å in the local rest-frame to excite Lyman-α transition and be absorbed by the intervening neutral hydrogen gas. This produces a series of sharp absorption lines, called the Lyman-α forest, bluewards of the peak of the Lyman-α emission in the observed spectrum of the background object. The observed absorption lines can be used to chart the number density of neutral hydrogen as a function of redshift along a particular line of sight. For a high-redshift background object that may being residing in the EoR, the vast amount of neutral hydrogen in the IGM will completely absorb all UV photons, saturating the observed spectra bluewards of the Lyman-α emission peak, a feature called the Gunn-Peterson trough. This observation can, therefore, be used to set a

limit to the end of reionization, and recent observations have shown that reionization may have ended by $z \sim 6$ (Robertson et al., 2013, 2015).

Although the CMB and Lyman-α forest offers some insights into reionization, they suffer from several limitations. First, the CMB only provides integrated measurements of the column density of ionized gas with no information about the reionization history at different redshifts. On the other hands, the optical depth for absorption of Lyman-α photons is highly sensitive to the abundance of neutral hydrogen – even a very small fraction of neutral hydrogen ($> 10^{-3}$) will saturate the IGM absorption an produce the Gunn-Peterson trough. Therefore, it will be difficult to distinguish the Lyman-α forest results from during the middle and early stages of reionization. In addition, both probes offer little information on the spatial fluctuations of the matter density at different redshifts.

1.2 21 cm Line as a Probe to the EoR

To obtain better constraints on the EoR, astronomers have been looking for better astrophysical probes, and the 21 cm emission line is a the top candidate. This emission line is well-known in astronomy, and its history can be traced back to 1944. Hendrik van de Hulst, who was a graduate student at University of Utretcht at the time, was asked by Jan Hendrik Oort, one of the great Dutch astronomer at Leiden Observatory, to investigate which atomic spectral lines might be observable in radio frequencies. Hulst proposed that the emission from the hyperfine transition in the ground state of neutral hydrogen with the rest-frame frequency of 1420.4058 MHz (wavelength of 21.106 cm) should be detectable in astrophysical settings. The ground state of a neutral hydrogen atom is split into two energy levels due to the magnetic dipole

interaction between the electron and proton that causes their spin to either be parallel or antiparallel. The energy state of the atom is slightly higher when the spins are parallel. Thus, the electron will eventually flip to the antiparallel spin direction as the atom always wants to be in the lowest energy state possible. The 21 cm emission line is produced by this spontaneous decay of the electron, which is considered a forbidden transition due to an extremely small transition rate of 2.9×10^{-15} s^{-1} and a mean lifetime of the excited state of around 10 million years. However, the huge abundance of neutral hydrogen in the IGM allows this emission to be detectable.

As a probe of the EoR, the 21 cm emission has three enormous advantages in comparison to other probes. First, the 21 cm emission line is extremely narrow, allowing redshift information to be precisely extracted from the observed redshift of the emission lines throughout the entire history of reionization. Second, it directly probes the neutral hydrogen gas in IGM, which is the main contribution to the baryonic matter during reionization. Finally, as a forbidden transition, it is fairly weak; therefore, it is far from saturation and is thus sensitive to the early and middle stages of reionization. In principle, this line can be used to map the distribution of the neutral hydrogen gas as a function of redshift throughout the reionization history and beyond, allowing us to create a tomographic map of the neutral hydrogen history of the Universe.

Scott and Rees (1990), Madau et al. (1997), and Tozzi et al. (2000) were among the first to consider radiative transfer of 21 cm emission in astrophysical scenarios. The emergent radiation from a cloud of neutral hydrogen gas along a line of sight is made up of the 21 cm emission from the cloud and the illuminating background radiation from the CMB. This emergent radiation can be measured against the CMB from a (usually hypothetical) sightline freed of neutral hydrogen to obtain the the differential brightness temperature of the 21 cm emission from the neutral hydrogen gas along

the line of sight,

$$\delta T_b(r_\parallel) = \frac{T_S - T_\gamma(z)}{1+z}(1 - e^{-\tau_\nu}) \tag{1.1}$$

$$\approx 9 x_{HI}(r_\parallel)(1+\delta(r_\parallel))(1+z)^{1/2}\left[1 - \frac{T_\gamma}{T_S}\right]\left[\frac{H(z)/(1+z)}{\mathrm{d}v_\parallel/\mathrm{d}r_\parallel}\right] \ \mathrm{mK}. \tag{1.2}$$

In this expression, T_S is the *spin temperature* of the neutral hydrogen gas, which quantifies the relative number densities of neutral hydrogen atoms in the two hyperfine levels of the electronic ground state. T_γ is the temperature of the CMB background. All the other terms arise from the optical depth of the 21 cm line, τ_ν, which relates the brightness temperature to the neutral fraction of the hydrogen gas, x_{HI}, the fractional over-density of the local baryons, $(1+\delta)$, and the gradient of the proper velocity along the line of sight $(\mathrm{d}v_\parallel/\mathrm{d}r_\parallel)$.

There is one important implication from the expression of the differential brightness temperature – the observed signal will be seen as an emission if the spin temperature is higher than the CMB temperature and as an absorption otherwise. The former scenario is expected during the EoR, where non-ionizing radiation from stars and galaxies would heat up the neutral hydrogen gas, increasing its the kinetic energy and coupling the spin temperature to the kinetic temperature. The latter scenario is expected during the Dark Ages, where the IGM was still cold and had not been heated by radiation yet, as well as during the epoch right after the formation of the first star and galaxies where scattering of Lyman-α photons couples the spin temperature to the unheated kinetic gas temperature. In this dissertation, we will primarily be focusing on the emission signal during the EoR.

Figure 2, reprinted from Pritchard and Loeb (2012), illustrates the key features of this signal. The top panel shows the time evolution of the simulated 21 cm brightness temperature fluctuations as a function of redshift, with time after the Big Bang and

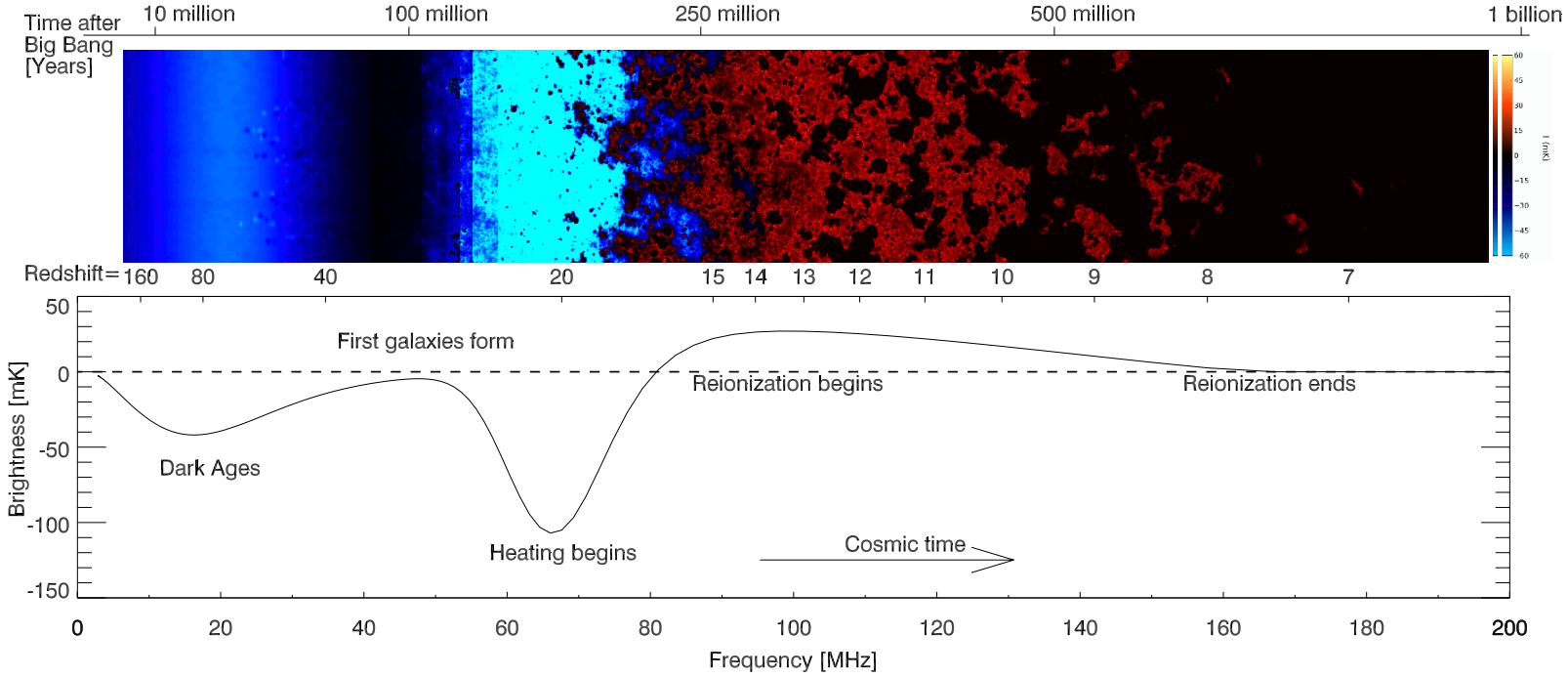

Figure 2. Time evolution of 21 cm signal. Top: Simulated 21 cm brightness temperature fluctuations from the beginning of the Dark Ages through the end of the reionization epoch. Coloration indicates the strength of the 21 cm brightness as it evolves through two absorption phases during the Dark Ages and the Cosmic Dawn and the emission phase during the EoR before the signal disappear after the IGM has been ionized. Bottom: Spatially averaged signal as a function of redshift. Reprinted from Pritchard and Loeb (2012).

observed frequencies indicated. The bottom panel show the spatially averaged signal through the different epochs.

1.3 Current Experiments, Challenges and Results

Tomographic mapping of redshifted 21 cm signal has not been possible until about two decades ago due to technological limitation. Such an observation would require a very sensitive radio interferometer that can detect the signal at sub-mK temperature at frequencies between 50 to 200 MHz. As a result, the design of the array would require hundreds to thousands of antennas distributed over large area to yield sufficient sky coverage, angular resolution and sensitivity. Accurate redshift-frequency mapping would also require observing not only with a narrow ($\lesssim$10 kHz) spectral channel but also over a large ($\sim$ 100 MHz) smooth frequency bandwidth, requiring substantial computing power for post-processing and data analysis. In addition, the observed frequency ranges cover the FM radio band. Radio telescopes targeting 21 cm tomography, thus, must be developed in a very secluded site freed from the human population to minimize radio interference. Thanks to the recent advancement in computer hardware and engineering and the establishment of remote observatory sites, such observing facilities are now possible. (For a comprehensive reference on the fundamental of radio interferometry, see, e.g., Thompson et al. 2017. For review on 21 cm tomography, see, e.g., Furlanetto et al. 2006; Morales and Wyithe 2010; Pritchard and Loeb 2012)

So far radio interferometers that have been conducted experiments aiming to map the 21 cm signal from the EoR include: the Murchison Widefield Array (MWA; Tingay et al., 2013), the Low Frequency Array (LOFAR; van Haarlem et al., 2013), the Giant

Metrewave Radio Telescope (GMRT; Paciga et al., 2013), and the Donald C. Backer Precision Array for Probing the Epoch of Reionization (PAPER; Parsons et al., 2010).

Analysis of the data from these experiments is extremely difficult due to a few interconnecting challenges,

- There will be contaminations from several sources, including Galactic foreground emission, extragalactic foreground sources, systematics in an interferometer's response, interference from radio communication, and the ionosphere. The two foreground sources are especially problematic as their emission can be up to 5 orders of magnitude brighter than the 21 cm signal, making it challenging to completely remove them from the data. This will likely prevent us from composing direct images of the neutral hydrogen distribution for the foreseeable future, and detections will have to rely on statistical analysis of data. Even then, contaminations will bias the statistical measurements.
- Optimal statistical measurements will not only require thorough understanding of the signal, the foreground and the instruments to model, calibrate and analyze the data but also significant efforts to develop the computational tools to do such tasks. Since every instrument is different, most of the tools have been purposely built for specific instruments, and often multiple tools performing the same tasks are developed in conjunction to validate different methods. For example, the MWA collaboration has developed two calibration and imaging software packages (Mitchell et al., 2008; Sullivan et al., 2012) and three power spectrum estimators (Dillon et al., 2015; Trott et al., 2016; Barry et al., 2019), which have been compared and contrast in (Jacobs et al., 2016). The development of these tools did not occur over the course of a few months by a few people but hav

involved years of coding, testing and iteratively refining of the final products by a team that includes tens of scientists and software engineers.

- As we have never observed the EoR before, our knowledge is limited to our current understanding of reionization physics, astrophysics of the foreground, and properties of our instruments, which could be confirmed, improved or challenged by new detections. The best example of this is the recent evidence for detection of an absorption profile centered at 78 MHz in the sky-averaged 21 cm signal by the Experiment to Detect the Global Epoch of Reionization Signature (EDGES) (Bowman et al., 2018). This absorption trough has long been predicted by theoretical simulation (see bottom panel of Figure 2), but the signal detected by EDGES is at least 2 times stronger and significantly narrower than the predicted signal. The detection has motivate many debates on both the theoretical prospects for the origin of the signal and the accuracy of the foreground model and the instruments used in the experiment (see, e.g., Barkana 2018; Feng and Holder 2018; Hills et al. 2018).

Nevertheless, there have been significant progress in the study of the statistics of the 21 cm brightness temperature fluctuations over the past decade, particularly through the power spectrum analysis. The reason for the strong interest in the power spectrum among the EoR community is not only because of our familiarity with the statistic from the analysis of the CMB experiments (Tegmark, 1997a,b) but also because of its potential as a statistics probe to the EoR. Fundamentally, a power spectrum of some density fluctuations is the Fourier transform of a two-points correlation function of that fluctuations, which can provide information on the magnitude of the fluctuations at different size scales. Early theoretical studies have shown that ionized "bubbles" of neutral hydrogen during reionization would imprint features into the

power spectrum of the 21 cm brightness temperature fluctuations, making it possible to distinguish them from fluctuations produced by the density perturbations. Therefore, the variation of the 21 cm power spectrum over ranges of redshift can be used to infer the evolution of the reionization process (Zaldarriaga et al., 2004; Furlanetto et al., 2004a,b; Zahn et al., 2007). The 21 cm power spectrum could also improve constraints on the fundamental cosmological parameters when jointly fit with data from the CMB experiments (McQuinn et al., 2006). Recent works have utilized Bayesian parameter inference to place constraints from 21 cm observations on a wide range of astrophysical parameters that govern the formation of the first stars and galaxies and the reionization process, such as the ionization efficiency of star-forming galaxies, the minimum halo virial temperature, and the mean free path hydrogen ionizing photons (Greig and Mesinger, 2015; Kern et al., 2017; Schmit and Pritchard, 2018).

Several upper limits of the 21 cm power spectrum have been made from the current generation of EoR experiements (see, e.g., Paciga et al. 2013; Parsons et al. 2014; Dillon et al. 2014, 2015; Ali et al. 2015; Jacobs et al. 2015; Beardsley et al. 2016; Patil et al. 2017; Kolopanis *et al.*, in prep.; and Berry *et al.*, in prep.), including robust characterization of the foreground contamination and instrumental systematics in the power spectrum (Morales et al., 2012; Hazelton et al., 2013; Jacobs et al., 2013; Liu et al., 2014; Thyagarajan et al., 2015a,b, 2016).

Lessons from the first generation of experiments have led to the design of the Hydrogen Epoch of Reionization Array , which is currently being built in the Karoo desert in South Africa. HERA will be a highly-packed, redundant-baseline array that is optimize for the power spectrum analysis while also retaining imaging performance on sub-degree scales. When completed, it will consist of 350, zenith-pointed, 14-meter dishes fed by dual-polarization dipoles, with most dishes closely packed into a hexagon

core approximately 300 meters in diameter and a small number of dishes spreading around the hexagon core to improve imaging performance. The MWA has also been recently upgraded to the Phase II (hearafter MWA-II; Wayth et al., 2018) with 128 additional antenna tiles in a close-packed hexagon arrangement as well as individually in the far outrigger to improve both the power spectrum and imaging sensitivity. The SKA (Square Kilometre Array; Mellema et al., 2013), which will be a multinational large scale radio observatory, is also scheduled to be built in the next decade. When completed, the SKA will be able to achieve high performance for both the power spectrum and direct imaging of the EoR. Statistical analysis of the EoR, nevertheless, will remain important for the next decade and beyond.

1.4 One-point Statistics of 21 cm Fluctuations

Despite the promising prospects on the detection of the 21 cm power spectrum with the upcoming, second-generation, experiments like HERA and the MWA-II, the cosmology and astrophysics communities have been actively looking for additional statistical probes to the EoR. Apart from the theoretical appeals for such studies, there are several constructive reasons that we may want to pursue them.

- **Additional Information.** Because the power spectrum only measures the amplitude of the 21 cm brightness temperature fluctuations at different scales, the underlying distribution of the neutral hydrogen cannot be probed (Furlanetto et al., 2004a). Morphological features of the ionized bubbles, such as their sizes and locations, also cannot be probed by the power spectrum. These characteristics of the fluctuations are important as they directly relate to the fundamental astrophysics of the reionization process and the formation of the first generation of

galaxies. Alternative statistics may allow probing of additional information that can be linked to these characteristics.

- **Confirmation.** Since we have never observed the EoR before, there could be many unknown systematics.[1] Alternative statistical probes to the EoR can provide extra layers of assurance by confirming the power spectrum detections.
- **Systematics.** Different statistics suffer differently from contamination and systematics. This means that one statistic may be more or less biased by noise or foreground contamination than another statistic. Thus, the uses of multiple statistics to analyze the same signal are good checks for unknown systematic effects. A joint analysis of multiple statistics could also provide better constraints on the reionization parameters.
- **Extension.** To confirm the Cosmic Dawn signal detected by EDGES (see the previous Section), the EoR community has been actively investigating additional upgrades to the current facilities and new concepts to extend 21 cm studies into the Cosmic Dawn epoch, accessible at lower frequencies where the foregrounds are even stronger. Alternative statistical probes could be more feasible than the power spectrum in such scenarios.

One promising alternative statistic to probe the EoR, which will be the main focus of this work, is the one-point probability distribution function (PDF) of the 21 cm brightness temperature fluctuations and its higher-order moments, collectively refer to as 21 cm one-point statistics. The two primary appeals of 21 cm one-point statistics are their simplicity and their direct sensitivity to the distribution of the 21 cm brightness temperature fluctuations and, thus, non-Gaussianity in reionization. As reionization

[1] We have seen this happened with an unrelated experiment in the past (BICEP2/Keck and Planck Collaborations et al., 2015).

progresses, ionized regions will form around groups of sources with high-energy UV radiation, causing the distribution of 21 cm intensity field to deviate from the nearly Gaussian underlying matter density field (Ciardi and Madau, 2003; Furlanetto et al., 2004b; Bharadwaj and Pandey, 2005; Cooray, 2006; Iliev et al., 2006; Mellema et al., 2006; Lidz et al., 2007). Since a power spectrum is not sensitive to the distribution of a signal, different underlying distributions of the 21 cm brightness temperature fluctuations could result in the same power spectrum. By also measuring one-point statistics, we can eliminate this concern, as well as proving information on the distribution and non-Gaussianity in reionization. We provide an overview summary of this particular statistics in the following few sections.

1.4.1 The 21 cm One-point PDF

Simply put, a 21 cm one-point PDF is a histogram calculate from all independent pixels in a map of 21 cm brightness temperature fluctuations, normalized to an integral of one. It can, therefore, provides information on the overall distribution of the 21 cm brightness temperature across the map, and hence the overall balance between ionized and neutral hydrogen gas in the observed fluctuations. It cannot, however, provide information on the spatial distribution of a specific ionized or neutral region, and the information that can be obtained is limited by the scale of the angular resolution of the telescope. Regardless, the additional information on the distribution of the signal that can be obtained from the 21 cm one-point PDF is very beneficial, especially to the study of non-Gaussianity in reionization.

To illustrate, one-point PDFs at different reionization epochs measured from a 21 cm full-sky model based on a simulation by Lidz and Malloy (2014) are shown in

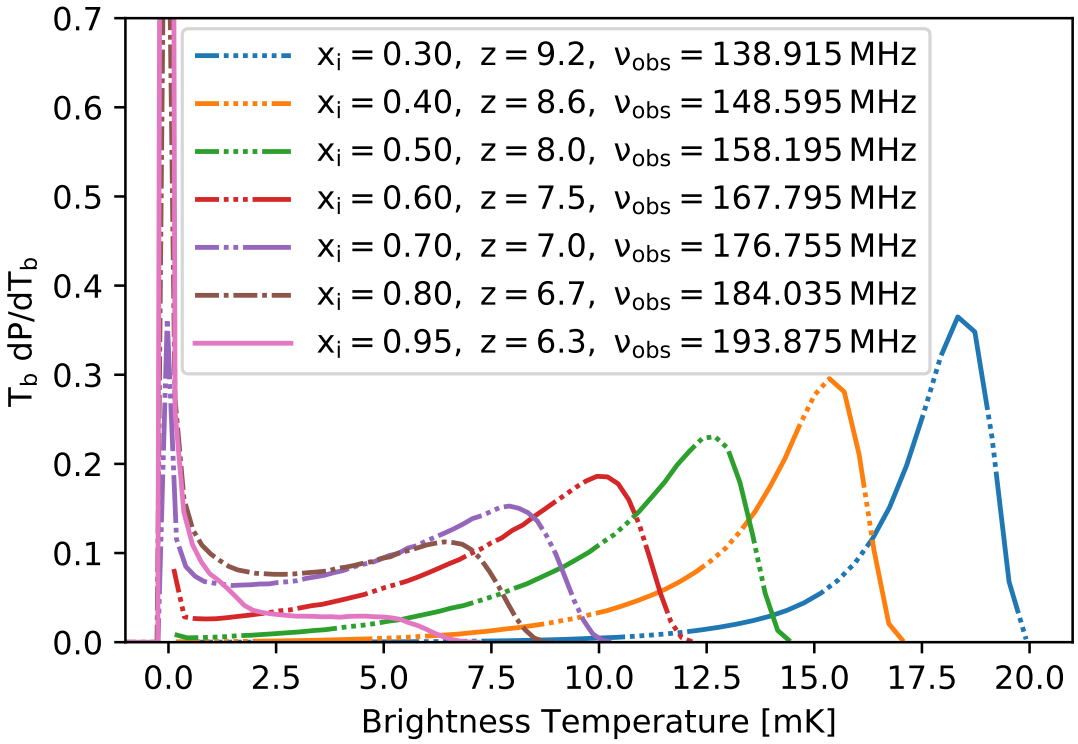

Figure 3. Brightness temperature PDF of the 21 cm lightcone sky model from $x_i = 0.3$ to 0.8, at every 0.1 step, and at $x_i = 0.95$ ionised fraction. The shape of the PDF changes from Gaussian-like to bi-modal to Delta-like function as reionization progresses and manifest the redshift evolution of the statistics shown in Figure 4.

Figure 3 (see Section 2.3 and Appendix B for discussion on how we construct this model).

Early in reionization ($x_i < 0.5$), the hydrogen gas is still mostly neutral with small pockets of cold spots that are beginning to grow into ionized regions. This results in a Gaussian-like PDF with a narrow peak located at higher brightness a long tail of low brightness that accounts for the cold spots. As reionization progresses, more of the neutral hydrogen gas will be excited and ionized. The peak of the PDF will drift toward the lower brightness temperature during this phase, and more density will be added to its left tail. At some point during the middle of reionization ($x_i = 0.6$), small

ionized region will form, and the PDF will start to develop a second peak at zero brightness that corresponds to the ionized regions. The zero peak will continue to grow as more ionized regions are formed, and eventually ($x_i \approx 0.7$) they will start to dominate the underlying fluctuations, shifting the PDF to become a bi-modal function. As more ionized regions form, the density of the zero peak that corresponds to the ionized regions increases. Finally, at the very end of reionization, when most of the sky exhibits no 21 cm signal and only a few isolated pockets of emission remain, the PDF becomes a Delta-like function, centering at zero with a long tail toward the warmer temperature.

This characteristic shift of the PDF from Gaussian-like to bi-modal to delta-like distribution has been shown in multiple simulation to be unique to the 21 cm signal during the EoR. In addition, details of the progression of this evolution, such as how fast the peak shift to lower intensity and how fast the zero peak develops, are also tied to astrophysics of reionization, providing opportunity to study and put constraints on reionization parameters.

1.4.2 Higher-Order 21 cm Moments

One problem that may render the 21 cm one-point PDF impractical in actual measurements is a known fact that an interferometer typically does not measure the mean of the observed intensity field due the the lack of a zero-spacing baseline. This will shift the mean of the measured PDF to zero, making it harder to distinguish different phases of reionization.

Fortunately, the shape of the PDF can be quantified around the mean of the distribution using statistical moments. Given a map with N number of pixel, pixel values

x_i and the mean value $\overline{x} = \sum_{i=0}^{N} x_i/N$[2], the p-th order central moment, m_p, is defined as,

$$m_p = \frac{1}{N}\sum_{i=0}^{N}(x_i - \overline{x})^p. \tag{1.3}$$

Variance (S_2), which most of us are familiar with, is the 2nd order central moments. The quantities that may be more of interests to the EoR studies are skewness (S_3) and kurtosis[3] (S_4), which are the 3rd and 4th central moments normalized by the variance.

$$S_2 = m_2, \tag{1.4}$$

$$S_3 = \frac{m_3}{(m_2)^{3/2}}, \tag{1.5}$$

$$S_4 = \frac{m_4}{(m_2)^2} - 3. \tag{1.6}$$

Following the above definitions[4], qualitatively, the mean describes the location of the distribution, and the variance describe the scale (or spread) of the distribution around its mean. These two quantities together are sufficient to fully describe a Gaussian distribution.

Both skewness and kurtosis describe the different properties of the shape of the PDF relative to a Gaussian distribution with the same variance. Skewness describes the symmetry of the distribution. A negative skewness indicates that the left tail of

[2]This definition is also a definition of the first-order raw moment. In other words, the mean is defined as the first raw moment in statistics.

[3]The exact term for the definition of the kurtosis given here is *Fisher's kurtosis* or *excess kurtosis*. Another definition, with no -3 term, is the Pearson kurtosis (Pearson, 1905). However, in physical sciences, the term kurtosis is generally refer to the excess kurtosi.

[4]Mean, variance, skewness and kurtosis can also be defined by using cumulants. In some cases theoretical treatments of problems in terms of cumulants are simpler than those using moments. The moments determine the cumulants in the sense that any two probability distributions whose moments are identical will have identical cumulants as well, and similarly the cumulants determine the moments.In particular, when two or more random variables are statistically independent.

the distribution (pointing toward negative values) is longer than the right tail (toward positive values) and that most mass of the distribution is concentrated on the right, whereas a positive skewness indicates the opposite. Kurtosis describes the heaviness of the tails of the PDF. A positive kurtosis indicates that more mass is concentrated on the tails of the distribution than around its peak, and a negative kurtosis indicates the opposite. A perfect Gaussian distribution is unique in that its skewness and kurtosis are both zero.[5] Therefore, non-zero skewness or non-zero kurtosis, or both, is a clear indication that the distribution is not a Gaussian.

Due to their sensitivity to non-Gaussianity in the PDF, skewness and kurtosis of 21 cm brightness temperature fluctuations can provide good checks for non-Gaussianity in reionization. The unique shape and evolution of the 21 cm brightness temperature PDF also give rise to distinct functions of 21 cm skewness and kurtosis over reionization redshift. With the addition of the variance of the 21 cm fluctuations, the three statistics can be used together to robustly identify different phases of reionization.

Figure 4 illustrate this point, where we show variance, skewness and kurtosis, calculated from the same model used in Figure 3, along with the ionized fraction of the model, as a function of frequency and redshift. In conjunction with the PDF in Figure 3, it is evident that each of the statistics follow a unique evolution that is complementary to one another to help identifying different phases of reionization. Namely, a Gaussian-like PDF with a long tail toward zero that takes place early in reionization can be identify with a negative skewness and a positive kurtosis. In contrast, the Delta-like PDF near the end of reionization yields both skewness and kurtosis with high positive values. A qualitative interpretation of skewness and kurtosis of a bi-modal distribution

[5]In theory, a non-Gaussian function with zero skewness and zero kurtosis can be formed, but, given the unique shape of the 21 cm brightness temperature PDF, it is unlikely that the PDF would be somehow contaminated to result in zero skewness and kurtosis measurements.

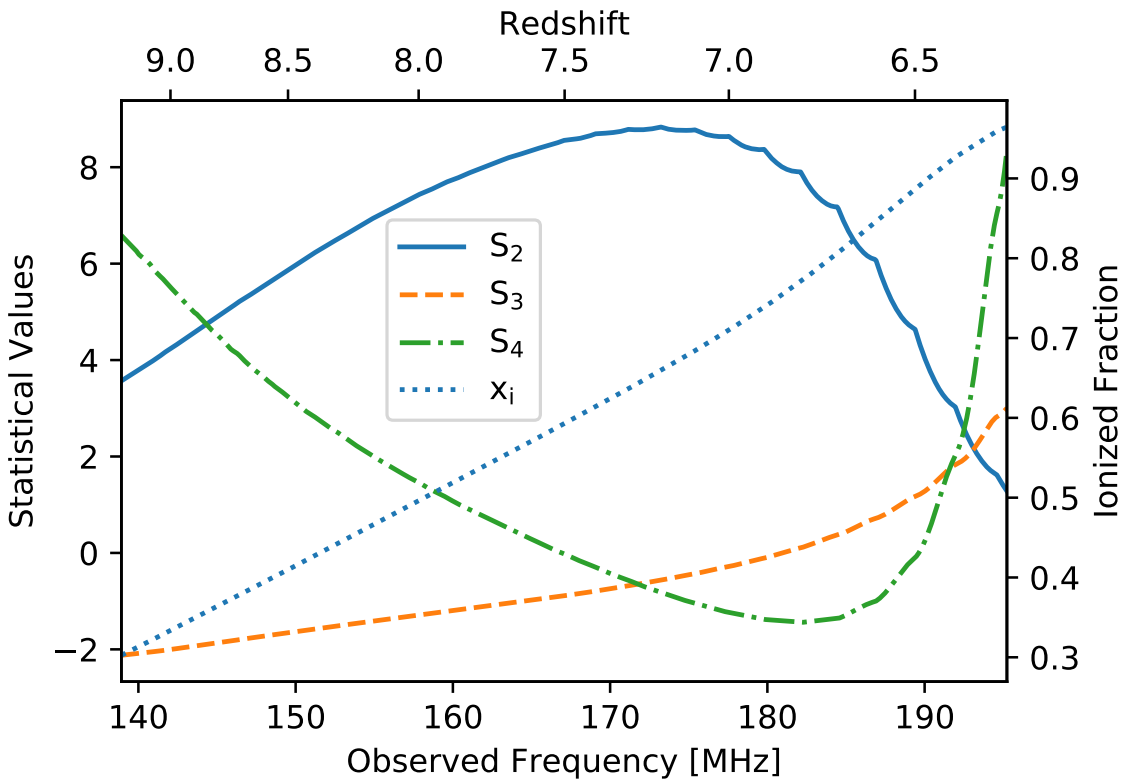

Figure 4. Variance (solid line), skewness (dashed line) and kurtosis (dot-dash line) of the input lightcone model calculated using all of its pixels as a function of frequency and redshift. The ionised fraction of the model at each redshift is shown as the dotted line. The left y-axis shows corresponding statistical values, whereas the right y-axis shows the ionised fraction. These measurements illustrate the unique redshift evolution of one-point statistics and act as references for our analysis.

is complicated and unintuitive, but this transitional period can be roughly identified by the crossing of the skewness and kurtosis, the peak of the variance, or the declining kurtosis followed by an abrupt up-turn.

The details of the evolution of the 21 cm PDF, along with its variance, skewness and kurtosis, will change depending on the details of underlying astrophysical process that governed reionization. Recent papers have shown that variance and skewness react to changes in reionization scenarios rather distinctively to allow discerning of

different reionization models (see, e.g., Harker et al. 2009; Watkinson and Pritchard 2014, 2015; Watkinson et al. 2015; Shimabukuro et al. 2015). These studies, however, primarily focus on the theoretical aspects of the statistics, whereas measurements from actual observations will be biased due to contamination from astrophysical foreground sources and other systematics. In addition, the kurtosis has been neglected in literature, but we have shown here that it could provide significant additional information about the state of the 21 cm brightness temperature PDF.

1.5 This Dissertation

Over the course of the next three chapters, we will investigate the detectability of 21 cm one-point statistics from the observational perspective, focusing on the effects of foreground and instrument systematics on the statistics. We will develop tools to perform realistic simulations of mock 21 cm observations, focusing HERA as the instrument. Using these mock observations, we will show in Chapter 2 that HERA will be able to measure 21 cm one-point statistics with high sensitivity if foreground contamination can be mitigated. In Chapter 3, we will develop a foreground avoidance method for one-point statistics and apply it to the HERA simulations to further gauge the detectability of the statistics. In Chapter 4, we will demonstrate some of the techniques that we will be developing on the first season data from the MWA observations. Finally, we conclude in Chapter 5 by discussing the implications of our results.

Chapter 2

SENSITIVITY OF THE HYDROGEN EPOCH OF REIONIZATION ARRAY TO 21 CM ONE-POINT STATISICS

The first question that emerges when it comes to the measurements of 21 cm one-point statistics in real observations is whether a telescope will have sufficient sensitivity to make such measurements. This translates into knowing the expectation values and the uncertainties of the statistics as measured by a particular telescope. Both of which depend on how the observed 21 cm brightness temperature intensity fluctuations are influenced by the beam response of the telescope, thermal noise, and other observational parameters.

Using HERA as a telescope model, we will develop simulation and analytical tools to perform mock observations of 21 cm brightness temperature observations and derive estimates for the sensitivity of the telescope to 21 cm one-point statistics. This chapter is based on Kittiwisit et al. (2018) with minor changes for coherency within this dissertation.

2.1 HERA

HERA is a second-generation radio interferometer optimized for redshifted 21 cm power spectrum detection. Presently under construction, HERA uses large, 14-metre parabolic dishes as antenna elements with most dishes densely packed into hexagon shape to increase the sensitivity at the short baselines and aid with calibration. A number of outriggers are spread around the hexagon core to improve imaging perfor-

mance. The construction of the telescope will be divided into 5 stages. As of 2017, the first stage with 19 dishes has been completed and commissioned. The second stage with 37 dishes is being constructed at the time of writing of this manuscript, and the third, fourth and the final fifth stages with 128, 240 and 350 dishes are scheduled to be constructed in 2017, 2018 and 2019. Observations with each build-out stage will be conducted subsequently following each construction period. For redshifted 21 cm observations, only the hexagon core will be used, yielding a maximum angular resolution of $\sim$ 0.5 deg from the full array. The telescope will have a $\sim 9^\circ$ primary field of view and will operate between 100 and 200 MHz with a channel bandwidth of 100 kHz.

Pointed at the zenith at all time, HERA will observe in a drift-scan mode and records $\approx$ 0.7 hours of integration for each observed field on the sky per day. Only nighttime observations will be used for redshifted 21 cm science, resulting in 125 hours of integration per field per year. Assuming $\approx$ 20% of observations are discarded due to poor weather conditions or radio-frequency interference, we expect an effective integration of 100 hours per year for any given region observed by HERA. As the array is located at -30° latitude, the Galactic Centre and anti-Centre pass almost overhead through the telescope beam. HERA will only compile 21 cm drift scans when the hight-Galactic latitudes are overhead, yielding a strip of a sky that spans approximately 180 degrees of Right Ascension nested between the Galactic plane.

However, simulating a full drift scans and making a single mosaic image from the observations are both very challenging. We approximate the drift scan by combining the analysis of multiple independent $\sim$9 degree fields that span the drift scan length. Less sky coverage of individual fields will yield measurements with higher sample variance, but we will show that statistics of the sky model can be recovered by averaging

over multiple measurements from different fields, as well as deriving sample variance and thermal noise uncertainties of these measurements. For the rest of this paper, we will simply refer to these multiple-field measurements as drift scan measurements.

Details of the specifications of the HERA instruments and planned observations are in Dillon and Parsons (2016) and DeBoer et al. (2017).

2.2 Sky Model

A good model of 21 cm brightness temperature fluctuations is needed as an input for our simulation. Many current state-of-the-art 21 cm simulators use semi-analytic methods to produce three-dimensional cubes of 21 cm brightness temperature fluctuation at different redshifts. These cubes are represented in rectangular comoving coordinates and can be up to a couple of $(\mathrm{Gpc/h})^3$ in size (e.g., Mesinger et al., 2011)), roughly equivalent to ~ 100 deg^2 regions of sky and corresponding depth at the relevant redshifts. In contrast, EoR observations produce three-dimensional data where two of the dimensions map the spatial dimensions of the sky and one dimension measures redshift (frequency), conflating line-of-sight distances with time, also known as the lightcone effect.

In order to match existing 21 cm models to an instrumental observation, we transform the four-dimensional (three spatial and one time) outputs of theoretical 21 cm simulations by Lidz and Malloy (2014) into a three-dimensional (two angular and one frequency) 21 cm observation cube. Existing techniques for generating lightcone cubes concatenate slices from simulated cubes at multiple redshifts into a single observational cube (e.g., Datta et al., 2012, 2014; Zawada et al., 2014). This method captures the time evolution, but not the curvature of the sky. To extend on these methods, we

developed a tile-and-grid process that maps a set of simulation cubes from different redshifts to a set of full-sky maps in HEALPix[6] coordinates. We elaborate and discuss the procedure in Appendix B.

The output from this process is a set of full-sky maps spanning redshifts observed by HERA in steps of 80 kHz spectral channels between $\sim 139 - 195$ MHz, which forms a sky model for this work. We use 80-kHz spectral channel here, instead of the 100-kHz channel of HERA, as we adopted the sky model from our previous effort to simulate other instruments. We decided to keep this bandwidth because extensive computing time would be required to rerun the lightcone tiling to match 100-kHz spectral channel, and a 20-kHz increase in channel bandwidth will only improve the thermal noise by $\approx 10\%$. Besides, final measurements are usually taken after averaging multiple spectral channels into a larger observed bandwidth to gain additional sensitivity, which we cover in Section 2.6.

We plot the PDF and one-point statistics of the output model in Figure 3 and Figure 4, which we thoroughly discussed in Section 1.4 to motivate this work.

2.3 Mock Observation Pipeline

To simulate mock observations of HERA as described in Section 2.1, we first smooth our sky model with a Gaussian kernel with a full width at half maximum (FWHM) corresponding to the angular resolution of each of the HERA build-out stages. Then, we pre-allocate 200 non-overlapping fields across the sky, project each field to the instrument observed sine coordinates and measure variance, skewness and

[6] http://healpix.jpl.nasa.gov

kurtosis as defined in Section 1.4, using only pixels within a radius equal to half of a FWHM of the HERA primary beam from the field center.

Before calculating statistics, each field is subtracted by its mean value to emulate the absence of the mean value of the sky in interferometric observations. Then, we randomly select 20 measurements and use their mean as an estimate for statistics recoverable by a HERA drift scan. To estimate the sample variance of the drift scan, we repeat the random draw of the 20 measurements, calculate the drift scan estimate from each draw, and use the standard deviation of all estimates as the drift scan sample variance uncertainty. In addition, we use the standard deviation of all 200 single-field measurements as an estimate for the sample variance uncertainty in single field observations. We add the sample variance uncertainty to the thermal noise uncertainty in quadrature to estimate the total uncertainty in any single-field measurement and propagate to drift scan measurements accordingly. We use statistics calculated from all pixels of the sky model smoothed to HERA angular resolution as the estimate of the ideal signal.

We adopt thermal noise calculations from Watkinson and Pritchard (2014), expanding their derivation to kurtosis. In summary, the uncertainty from thermal noise in interferometric observations (ΔT_n) can be described by the system temperature (T_{sys}) of the array, array filling factor (η_f), spectral channel bandwidth ($\Delta\nu$) and integration time of the observations (t_{int}) (Furlanetto et al., 2006),

$$\Delta T_n = \frac{T_{sys}}{\eta_f \sqrt{\Delta\nu \, t_{int}}}. \tag{2.1}$$

By assuming that the system temperature is dominated by the Galactic synchrotron radiation at the EoR observing frequency, $T_{sys} \approx T_{sky} = 180\ (\nu/180\ \mathrm{MHz})^{-2.6}\mathrm{K}$ (Mozdzen et al., 2016), Equation 2.1 can be expanded to obtain the thermal noise

uncertainty in redshifted 21 cm observations (σ_n),

$$\sigma_n = 2.9\,\mathrm{mK}\left(\frac{10^5\,\mathrm{m}^2}{A_{tot}}\right)\left(\frac{10\,\mathrm{arcmin}}{\Delta\theta}\right)^2 \times \left(\frac{1+z}{10.0}\right)^{4.6}\sqrt{\left(\frac{1\,\mathrm{MHz}}{\Delta\nu}\frac{100\mathrm{h}}{t_{int}}\right)}, \tag{2.2}$$

which depends on the total effective collecting area of the array (A_{tot}), the angular resolution of the array ($\Delta\theta$), redshift (z) and integration time of the observations (t_{int}) in addition to the spectral channel bandwidth.

Given an expression for the p-th order central statistical moments (m_p) in Equation 1.3 and the thermal noise uncertainty description in Equation 2.2, thermal noise induced estimator variance of the 2nd ($V_{\hat{m}_2}$), 3rd ($V_{\hat{m}_3}$) and 4th ($V_{\hat{m}_4}$) order statistical moments can be derived based on a statistical framework to obtain,

$$V_{\hat{m}_2} = \frac{2}{N}(2m_2\sigma_n^2 + \sigma_n^4), \tag{2.3}$$

$$V_{\hat{m}_3} = \frac{3}{N}(3m_4\sigma_n^2 + 12m_2\sigma_n^4 + 5\sigma_n^6), \tag{2.4}$$

$$V_{\hat{m}_4} = \frac{8}{N}(2m_6\sigma_n^2 + 21m_4\sigma_n^4 + 48m_2\sigma_n^6 + 12\sigma_n^8), \tag{2.5}$$

and later propagated to variance (S_2), skewness (S_3) and kurtosis (S_4) via Taylor expansion to obtain the estimator variance of the variance ($V_{\hat{S}_2}$), skewness ($V_{\hat{S}_3}$) and kurtosis ($V_{\hat{S}_4}$), yielding,

$$V_{\hat{S}_2} = V_{\hat{m}_2} \tag{2.6}$$

$$V_{\hat{S}_3} \approx \frac{1}{(m_2)^3}V_{\hat{m}_3} + \frac{9}{4}\frac{(m_3)^2}{(m_2)^5}V_{\hat{m}_2} - 3\frac{m_3}{(m_2)^4}C_{\hat{m}_2\hat{m}_3}, \tag{2.7}$$

$$V_{\hat{S}_4} \approx \frac{1}{(m_2)^4}V_{\hat{m}_4} + 4\frac{(m_4)^2}{(m_2)^6}V_{\hat{m}_2} - 4\frac{m_4}{(m_2)^5}C_{\hat{m}_2\hat{m}_4}, \tag{2.8}$$

where N is the number of samples in a measurement. $C_{\hat{m}_2\hat{m}_3}$ and $C_{\hat{m}_2\hat{m}_4}$ are the estimator covariance of the relevant moments, which can be derived in the similar manner

to obtain,

$$C_{\hat{m}_2\hat{m}_3} = \frac{6}{N} m_3 \sigma_n^2, \tag{2.9}$$

$$C_{\hat{m}_2\hat{m}_4} = \frac{4}{N}(2m_4\sigma_n^2 + 9m_2\sigma_n^4 + 3\sigma_n^6). \tag{2.10}$$

The thermal noise uncertainty of one-point statistics of each single field is then just a square root of its estimator variance. Appendix A provides a more detailed summary of Watkinson and Pritchard (2014) procedure as well as our full derivation of the estimator variance of the 4th statistical moments and the kurtosis.

We assume $t_{int} = 100$ hours for every $\Delta\nu = 80$ kHz spectral channel when calculating uncertainties from the thermal noise. The number of samples per measurement in an observation will be limited by the field of view and the angular resolution of the telescope. Because our maps oversample the angular resolution with multiple pixels, we calculate the number of independent resolution elements per pixel from the ratio of the pixel and the resolution element areas and multiply this factor to the number of pixels in a measurement to obtain N. The oversampling of the angular resolution does not affect the statistics because the over sampling factor is cancelled out in the moment equations (see Equation 1.3).

Table 1 summaries the parameters of our mock observations, where we refer to HERA240 and HERA350 arrays without their outriggers as HERA240 Core and HERA350 Core respectively.

2.4 Simulated Observed Intensity Maps

Figure 5 shows simulated observed brightness temperature intensity maps from our pipeline at $x_i = 0.5$, 0.7 and 0.95 for all of the HERA build-out stages with all panels taken from the same field in our sky model. The angular resolution increases as

Built-out Stage	Collecting Area (m^2)	Maximum Baseline (m)	Angular Resolution (deg)
HERA19	2,925	70	$\sim 1.53 - 2.16$
HERA37	5,696	98	$\sim 1.10 - 1.54$
HERA128	19,550	182	$\sim 0.59 - 0.83$
HERA240 Core	33405	238	$\sim 0.45 - 0.63$
HERA350 Core	50,953	294	$\sim 0.37 - 0.51$

Table 1. Instrument specifications for the HERA build-out stages used in our mock observations. We perform the simulation over ∼56 MHz bandwidth, from ∼139-195 MHz, with 80 kHz spectral channel bandwidth. Further information on the array configurations can be found in DeBoer et al. (2017).

the telescope grows and the fluctuations become more pronounced. Figure 6 shows a cut along the frequency direction from the same field at HERA350 Core angular resolution to illustrate the lightcone evolution. The size scale along the frequency direction grows as reionization progresses and reaches a typical size of ~ 4 MHz near the end of reionization. The brightness temperature scale of the observed maps is centered around zero with both negative and positive values due to the lack of mean measurements.

2.5 HERA350 Core Measurements

We will first present and discuss measurements for the HERA350 Core instrument with 80 kHz bandwidth. Figure 7 compare drift scan and single field measurements derived from the mock observations with measurements from the full-sky model smoothed to HERA350 Core angular resolution. Comparing the drift scan measurements with the input model statistics in Figure 4, we see the effect of HERA's relatively poor angular resolution, which acts to smooth the input maps, reducing

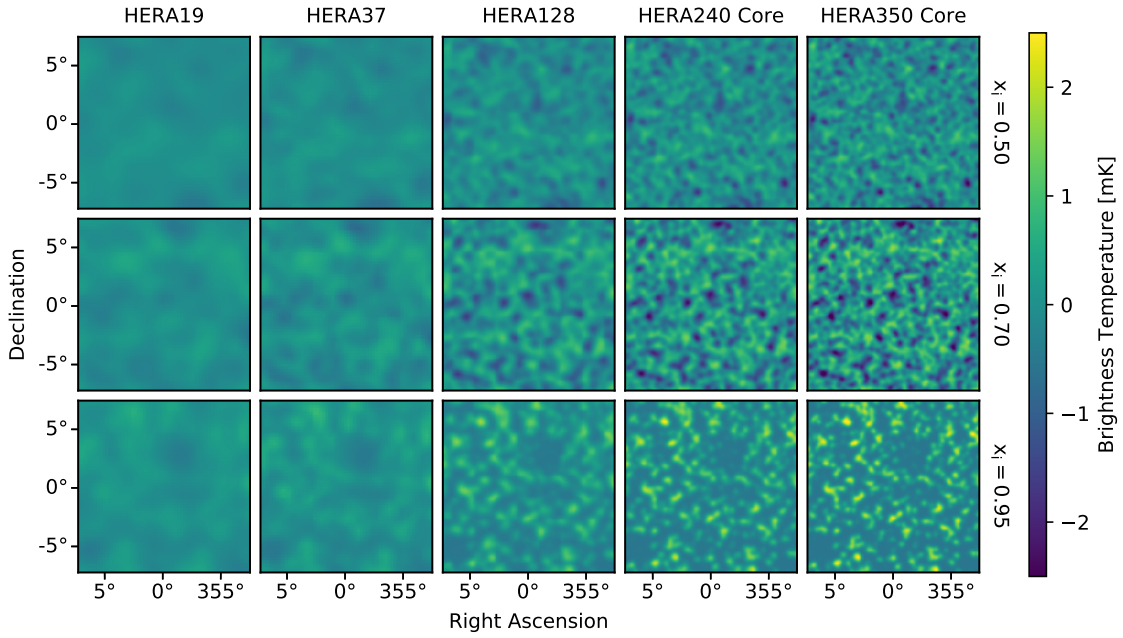

Figure 5. Simulated observations at ionized fraction of 0.5, 0.7 and 0.95 (top to bottom rows) with different HERA build-out stages (left to right columns). The 21 cm lightcone model is smoothed to the resolution of each array, showing more pronounced fluctuations as the angular resolution increases. No thermal noise is included in the simulation.

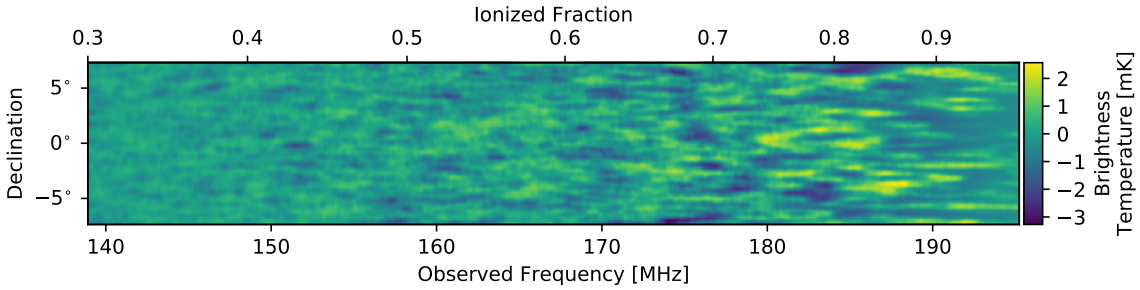

Figure 6. Lightcone slice from the HERA350 Core mock observations. The size scale along the frequency direction grows as reionization progresses and reaches a typical size of ~ 4 MHz near the end of reionization.

the observed variance, skewness and kurtosis. We will see below that this effect is especially pronounced for the HERA build-out phases, where the coarser angular resolution is predicted to yield one-point statistics that are only weakly non-Gaussian (Mondal et al., 2015).

Nevertheless, it is evident that HERA350 Core will be sensitive to one-point statistics, particularly in the second half of reionization where the rise of skewness and the pronounced negative dip and rise of kurtosis indicate non-Gaussian fluctuations. Uncertainty from thermal noise in the drift scan measurement of the variance is small throughout the redshift ranges, becoming negligible in comparison to the contribution from sample variance at the end of reionization, and should allow high sensitivity measurements. For skewness and kurtosis, the thermal noise is significant, resulting in large uncertainty in the drift scan measurements at the beginning of reionization, but the thermal uncertainty decreases as frequency increases, becoming minimal at the end of reionization, beyond $\sim$170 MHz for our sky model. The result is that the variance measurement is limited by thermal noise early in reionization and later by sample variance near the end of reionization while skewness and kurtosis measurements will be dominated by thermal noise throughout reionization, but significant detections will be possible near the end of reionization where the signal is strong.

As expected, statistics from single field measurements exhibit fluctuations due to sample variance as opposed to the smoothly evolving ensemble statistics derived from the full-sky model. Occasionally, the fluctuations sharply rise despite the overall small sample variance uncertainty. These strong fluctuations are interesting in their own right, and we explore their behavior in Section 2.7. The 20-field averaged, drift scan observations provide a much more faithful recovery of the model statistics with negligible fluctuations from sample variance.

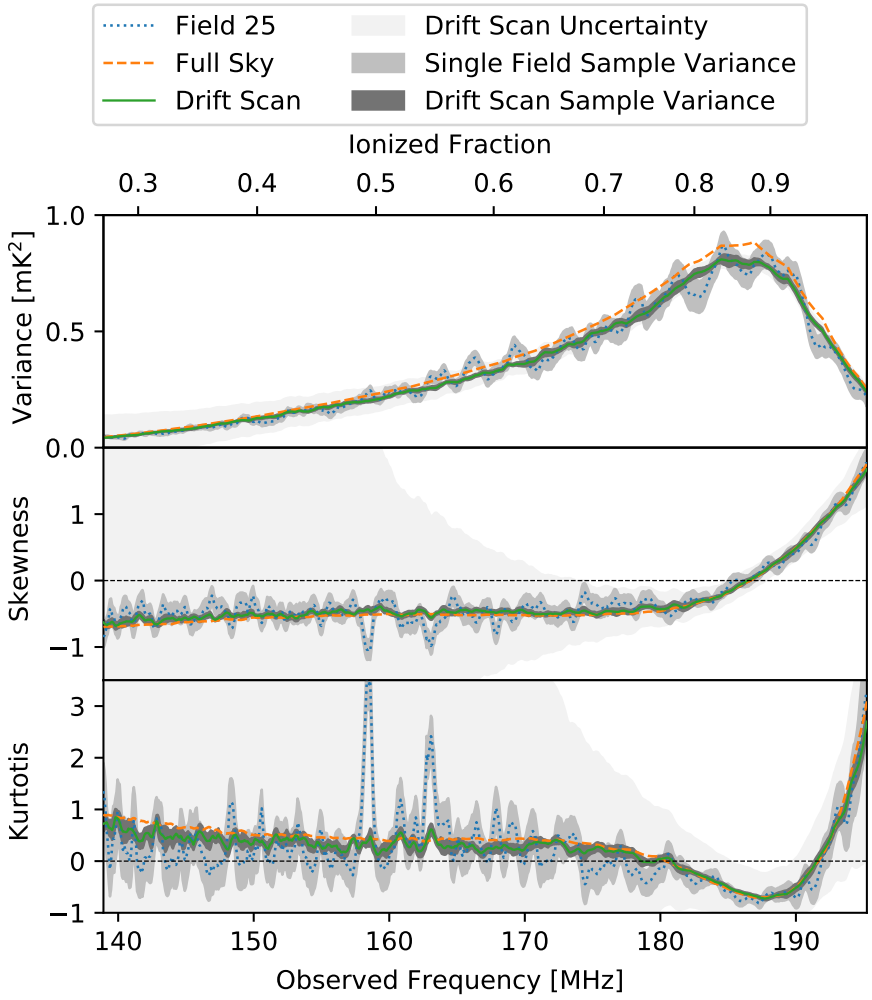

Figure 7. Variance, skewness and kurtosis (top to bottom panels) measured from simulated HERA 350 Core observations with 80 kHz channel bandwidth as a function of observing frequency and ionized fraction. The dotted line shows an example of statistics measured from a single field. The solid line shows the drift scan measurements, defined as the mean of 20 single-field measurements. The dashed line shows statistics derived from the full sky after smoothing to HERA350 Core angular resolution as a reference. The three shaded regions shows sample variance uncertainty of the drift scan measurements (dark), which is only visible in the kurtosis, sample variance uncertainty of a single field measurement (medium), and the uncertain of the drift scan measurements propagated from the single field sample variance and thermal noise uncertainty (light). HERA350 Core will be sensitive to one-point statistics, particularly in the second half of reionization. Skewness and kurtosis measurements are limited by thermal noise, but detections are possible near the end of reionization, while both thermal noise and sample variance are insignificant in variance measurements.

2.6 Improving Sensitivity with Bandwidth Averaging

We have only considered measurements from mock observations with 80 kHz channel bandwidth in Section 2.5. The narrow channel bandwidth limits thermal noise performance in the measurements. In this section, we introduce two methods of bandwidth averaging, a commonly used *frequency binning* and a less-common method, mainly used in the 21 cm power spectrum measurements that we term *frequency windowing*.

Frequency binning improves thermal noise uncertainty and can be done by averaging maps of neighboring spectral channels to produce a single output map with larger effective channel bandwidth and lower thermal noise. This is an effective strategy to improve thermal noise until the bin size becomes larger than the typical size of the features in the signal, at which point further increasing the bin size will diminish the strength of the signal by averaging over uncorrelated regions.

We find in Section 2.5 that skewness and kurtosis measurements are limited by thermal noise. We will show below that frequency binning can be used to significantly improve the sensitivity of HERA to these two statistics. We also find in Section 2.5 that measurements of the variance by HERA will be constrained by sample variance at high frequencies toward the end of reionization, rather than by thermal noise. Frequency binning will not improve sample variance sensitivity because the number of of samples that can be used in a measurement is the same for both the binned and un-binned maps when observing over the same field with the same instrument. Thus, it is of interest to explore an additional approach aimed at reducing sample variance. Since sample variance depends on the number of samples per map, which is fixed by the angular resolution and the field of view, the only way to increase the number of samples used in an estimate is to use maps from multiple spectral channels as a single data set. In this

method, we form a three-dimensional data cube from multiple maps of neighboring spectral channels and measure the statistics of the cube, using all samples within the field of view. We term this process frequency windowing. Thermal noise per pixel is unchanged with frequency windowing because the native spectral channel is preserved, but thermal noise uncertainty on the one-point statistic estimates will still decrease due to the $1/N$ factor in the estimator variance equations (see Equation 2.3–2.5).

To explore the relative trade-offs between the two methods, we perform frequency binning and frequency windowing on the brightness temperature maps from our HERA350 Core simulation, varying bin and window sizes from 1-8 MHz with 1 MHz increment. We start from the highest spectral channel in our $\sim$60-MHz bandwidth, at 195 MHz, and bin or window, progressing down to lower frequencies. The process is repeated on all 200 sample fields. Then, we make drift scan measurements and estimate the uncertainties for each case using the same method as described in Section 2.3.

The observed variance decreases across the observed frequency range when frequency binning is used, with particularly rapid decline near the variance maxima. This is expected as the signal strength along the frequency dimension in our HERA350 Core mock observations, shown in Figure 6, is smaller and more uniform early in reionization but grows and reaches the maximum strength and maximum variance at around 185 MHz. Binning the signal when both the signal strength and signal variance are high will greatly reduce the signal amplitude, resulting in much smaller observed variance. As a side note, the observed variance only slightly declines between the native 80-kHz channel bandwidth and 1-MHz binning case. This is expected as the coherence length of the 21 cm signal is predicted to be approximately 1 MHz (Santos et al., 2005). Thus, the bin size that is finer than 1 MHz would not dramatically alter

the signal variance. Although not shown, we find that the overall evolution of skewness and kurtosis recovered by the instrument do not change when frequency binning is used apart from slight variations between bins.

Compared to frequency binning, frequency windowing simply adds more samples along the frequency dimension. With no averaging of maps from neighboring spectral channels, variance of the signal within each spectral channel is preserved, and the observed variance would be the mean value of variance of all spectral channels within that window. Skewness and kurtosis are also preserved as the added samples from neighboring spectral channels do not alter the shape of the PDF but contribute to form a more well-sampled PDF, unless strong redshift evolution occurs between spectral channels. All statistics measured from frequency windowing data also show less variation between window to window and follow the sky model more closely.

We find that frequency binning is more effective for the skewness and kurtosis measurements at nearly all redshifts in our simulations since sample variance dominates the uncertainty over much of the modeled band, whereas frequency windowing is better for the variance measurements. To illustrate, we compare in Figure 8 the signal-to-noise ratio (SNR) of the statistics for different binning and windowing cases measured from the HERA350 Core simulation. We define the SNR as the absolute values of statistics divided by their uncertainties, and we use the mean values of the measurements from 10 independent sets of the drift scan simulations in the calculation to more clearly illustrate the results. The SNR improvement from frequency binning in the variance measurements saturates after the bin size reaches a few MHz because thermal noise has been reduced below sample variance at that point, putting the measurements in sample variance limited regime. The binned signal amplitude also declines at approximately the same rate as the thermal noise uncertainty when the

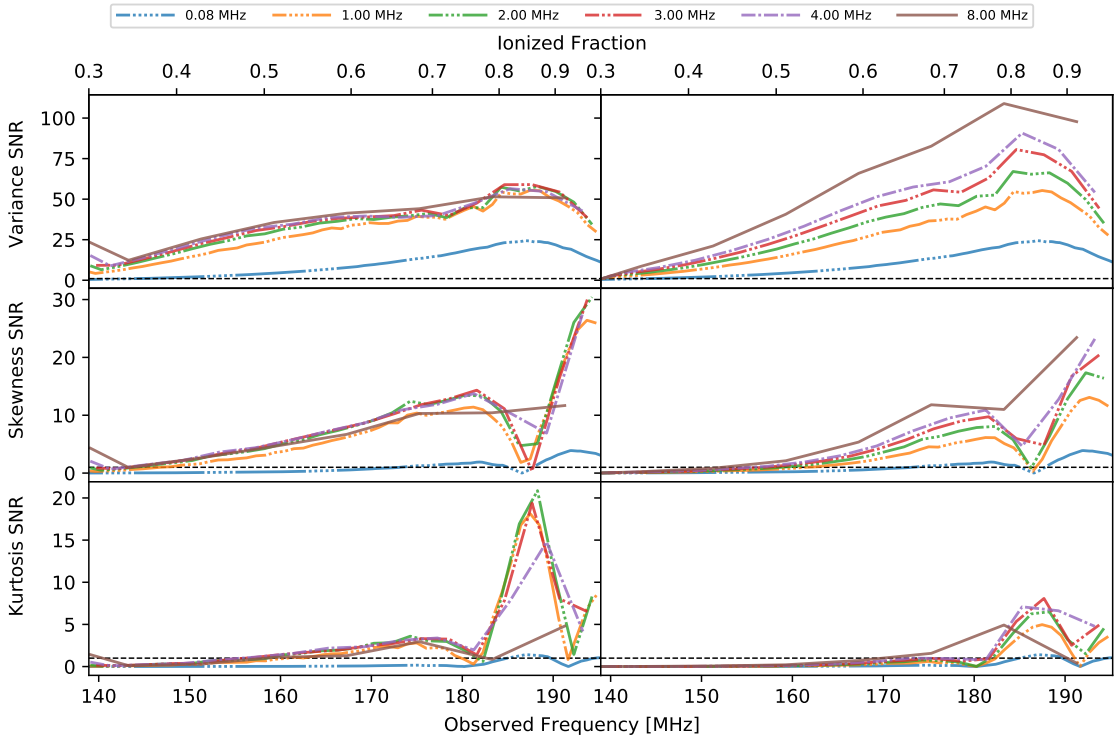

Figure 8. Comparing SNR measured from HERA350 Core simulation with different frequency binning (left column) and frequency windowing (right column) cases. SNR is defined as the ratio of the absolute values of the mean statistics and uncertainty from drift scan observations. Frequency windowing improves the sensitivity more than frequency binning at nearly all redshifts in the variance measurements due to the reduced sample variance, whereas frequency binning is more effective for skewness and kurtosis measurements as HERA observations on these two statistics are limited by thermal noise. The horizontal dashed lines indicate SNR=1.

bin size is larger than the typical signal feature size. With frequency windowing, SNR of the variance measurements continues to improve with larger windows. Although we only investigate up to an 8-MHz window case, we expect the SNR of the variance to continue improving beyond the 8 MHz window size. However, redshift evolution will have detrimental effect on the signal with that large bandwidth; thus, the logical choice would be to perform frequency windowing on the variance measurements only with a large enough window size to obtain sufficient SNR.

A general conclusion is that frequency windowing should be used in observations that are sample variance dominated, whereas frequency binning maybe more beneficial when observations are thermal noise dominated (depending on the spectral coherence of the underlying signal). This statement is easiest to explain quantitatively. For an observation at a particular frequency, integration time and angular resolution, the thermal noise description from Equation 2.2 can be plugged into the estimator variance formulas in Equation 2.3 to 2.5 to obtain a simplified thermal noise uncertainty equation for p-th order one-point statistics,

$$\sigma_{\hat{m}_p} = \sqrt{V_{\hat{m}_p}} \propto \frac{\sigma_n^p}{\sqrt{N}} \propto \frac{1}{\sqrt{N(\Delta\nu)^p}}. \tag{2.11}$$

When performing frequency binning with n_{ch} channels, the number of samples in a measurement N is unchanged, but the frequency binned map will have an effective channel bandwidth of $\Delta \propto n_{ch}$, resulting in $\sqrt{n_{ch}^p}$ reduction of thermal noise uncertainty. In contrast, performing frequency windowing with n_{ch} channels will not alter the channel bandwidth, but the number of samples in a measurement is multiplied by n_{ch}, reducing thermal noise uncertainty by just $\sqrt{n_{ch}}$. However, the increased number of samples from frequency windowing will also reduce sample variance, allowing detection with higher sensitivity in the case where thermal noise is no longer the limiting constraint of the observations.

For HERA, frequency binning will yield sufficient sensitivity on all observations of one-point statistics. Frequency windowing could also be used in the variance measurement if higher sensitivity is desired. A combination of both method should also be possible to further improve the sensitivity but is beyond of scope of the study in this work.

2.6.1 Performance of HERA Build-Out Stages

Although it is clear from Section 2.5 and 2.6 that the complete HERA 350 Core array will be able to mitigate sample variance by averaging statistics measured over multiple fields across the sky and utilizing bandwidth averaging, it is important to see how the smaller, planned built-out, arrays will perform as data from HERA 350 Core will not be available until after 2020.

In general, smaller arrays have two key disadvantages of less collecting area and worse angular resolution. Typically, smaller collecting area increases the thermal uncertainty, while poorer angular resolution smooths over the intrinsic 21 cm features, yielding a more-Gaussian like signal with lower amplitude than for higher angular resolutions. However, HERA is very close to being a filled aperture array, resulting in the angular resolution and array collecting area that roughly scale as the maximum baseline and the maximum baseline squared, respectively. As a consequence, it can be shown from Equation 2.2 that the thermal uncertainty per resolution element of HERA does not change with the size of the array. Thus, the only disadvantage of smaller HERA array is the reduced angular resolution that damps the signal and lowers the number of independent resolution elements per map.

For a detailed investigation, we perform frequency binning and frequency windowing on the mock observations of all HERA build-out stages, and calculate the drift scan statistics, sample variance uncertainty and thermal noise uncertainty for each case following the methods described in Section 2.3. The HERA build-out arrays cover angular resolution from $\sim$1.5° to 0.5° as the array grows. Thus, this study also gives an insight into the effects of angular resolution on the one-point statistics.

Figure 9 shows the one-point statistics measured from the mock observations of

each of the build-out stages, along with the corresponding SNR calculated in the same manners as in Section 2.6, with 1-MHz frequency binning applied before the calculations. It is clear that the derived statistics are affected by the increasing angular resolution as the array grows. Variance decreases with smaller arrays, similar to the effect of frequency binning. Skewness and kurtosis measured from smaller, HERA19 and HERA37, arrays also vanish, only fluctuating near zero throughout much of reionization. In contrast, the larger HERA128, HERA240 Core and HERA350 Core arrays exhibit non-zero skewness and kurtosis even early in reionization, diverging more from zero as the angular resolution improves. The negative region of kurtosis near the end of reionization only reaches significance in observations with these large build-out phases.

This resolution effect is an expected consequence from the angular resolution smoothing. With finer angular resolution, larger HERA arrays can resolve more of the intrinsic underlying fluctuation and preserve the amplitude of the signals. The shape of the PDF distribution of the signal is also preserved, and thus the values of skewness and kurtosis remain closer to the intrinsic level of the signals. When the angular resolution becomes larger than the typical sizes of the underlying signals, angular resolution smoothing blurs out the fluctuations, reduces the overall signal amplitude and shift the PDF from non-Gaussian to Gaussian. As a result, variance is greatly reduced, and skewness and kurtosis vanish. These results are in agreement with Mondal et al. (2015), who suggests, based on the study of 21 cm power spectrum SNR, that 21 cm signal would only be weakly non-Gaussian at a degree scale near the end of reionization, comparable to angular resolution of HERA19 and HERA37 arrays, and be mostly Gaussian otherwise.

Apart from better resolving the intrinsic fluctuations, increasing the angular reso-

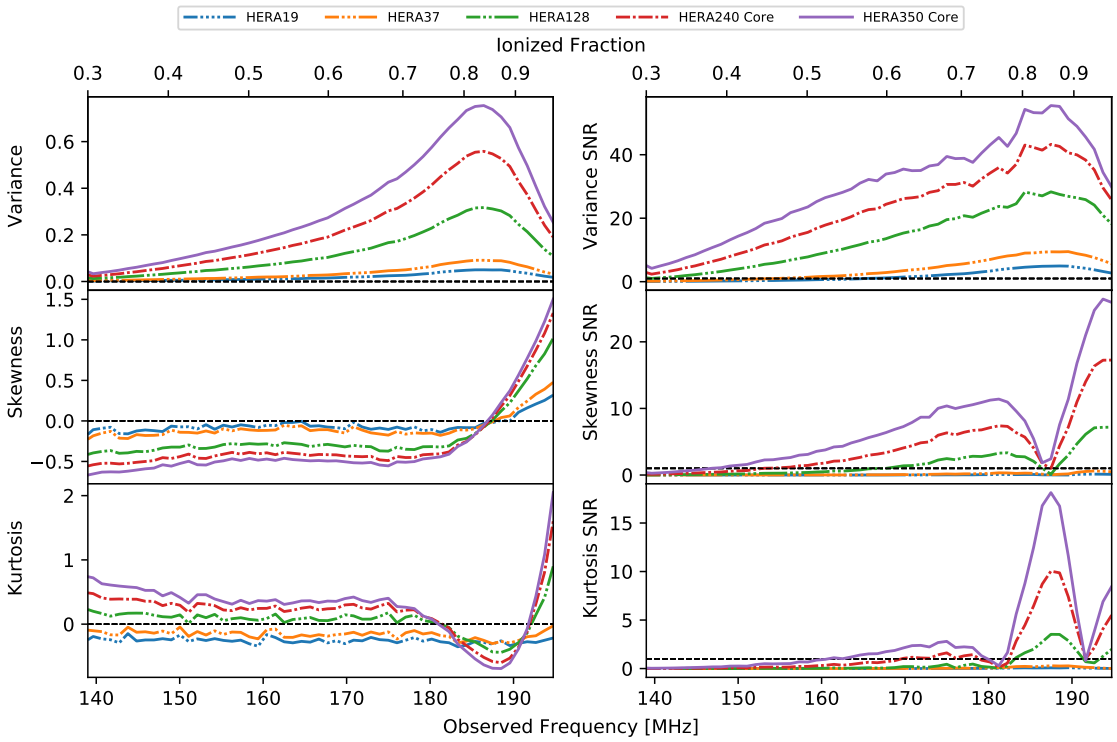

Figure 9. Mean drift scan statistics (left) and SNR (right) measured from the mock observations of all planned built-out HERA stages with 1-MHz frequency binning applied before the calculations. All HERA configurations should be able to measure the variance with high SNR. In addition, HERA128 and above will be able to measure the characteristic rise of skewness and the dip, then rise, of kurtosis near the end of reionization with sufficient SNR. The horizontal dashed lines on the statistics and SNR columns indicate zero statistical values and SNR=1 respectively.

lution will also reduce sample variance. All statistics measured from the mock observations of the arrays with finer angular resolutions also show less variation between bin to bin and follow the sky model more closely.

Our simulations suggest that all HERA configurations should be able to measure the variance with high SNR. In addition, HERA128, HERA240 Core and HERA350 Core will be able to measure the characteristic rise of skewness and the dip, then rise, of kurtosis near the end of reionization with sufficient SNR, especially when frequency binning is used, as demonstrated in Figure 9.

2.7 Strong Bias in Individual Field Measurements

In this chapter, we focus on recovering the one-point statistics over multiple fields corresponding the full drift scan area that will surveyed by HERA. Here we briefly turn our attention to the individual 9x9 deg^2 HERA beam fields in our simulations. As expected, statistics measured within individual fields are more susceptible to sample variance. For example, there is a strong kurtosis spike near 170 MHz in the measurement from field number 140 from our HERA350 Core simulation when 1-MHz frequency binning applied. This kurtosis spike is a factor of ~ 5 above the sample variance expected for the field. Significant outlier deviations such as these are seen in fields with one or two large cold or hot spots dominating the underlying fluctuation. Figure 10 illustrates the case. When cold or hot spots appear in the observed fields, they perturb the PDF, adding more density to the tails of the distribution, and causing kurtosis to rise. In some occasions, these outliers also shift the symmetry of the PDF and cause strong troughs in the skewness as appeared in Figure 7. This behavior can also be thought of as a strong sample variance bias – i.e., the outliers become dominating due to the small field of view.

Although the behavior discussed here is considered a bias in the measurements due small field of view, it could potentially be used as a simple and robust bubble detector. Statistical study of the frequency of occurrence of the outlier skewness and kurtosis peaks could be conducted for a given instrument and related to predictions from reionization models. The outliers should be less susceptible to noise in the underlying fluctuations than typical estimates of the statistics. However, investigation of this possible metric would require further study that is beyond the scope of this work.

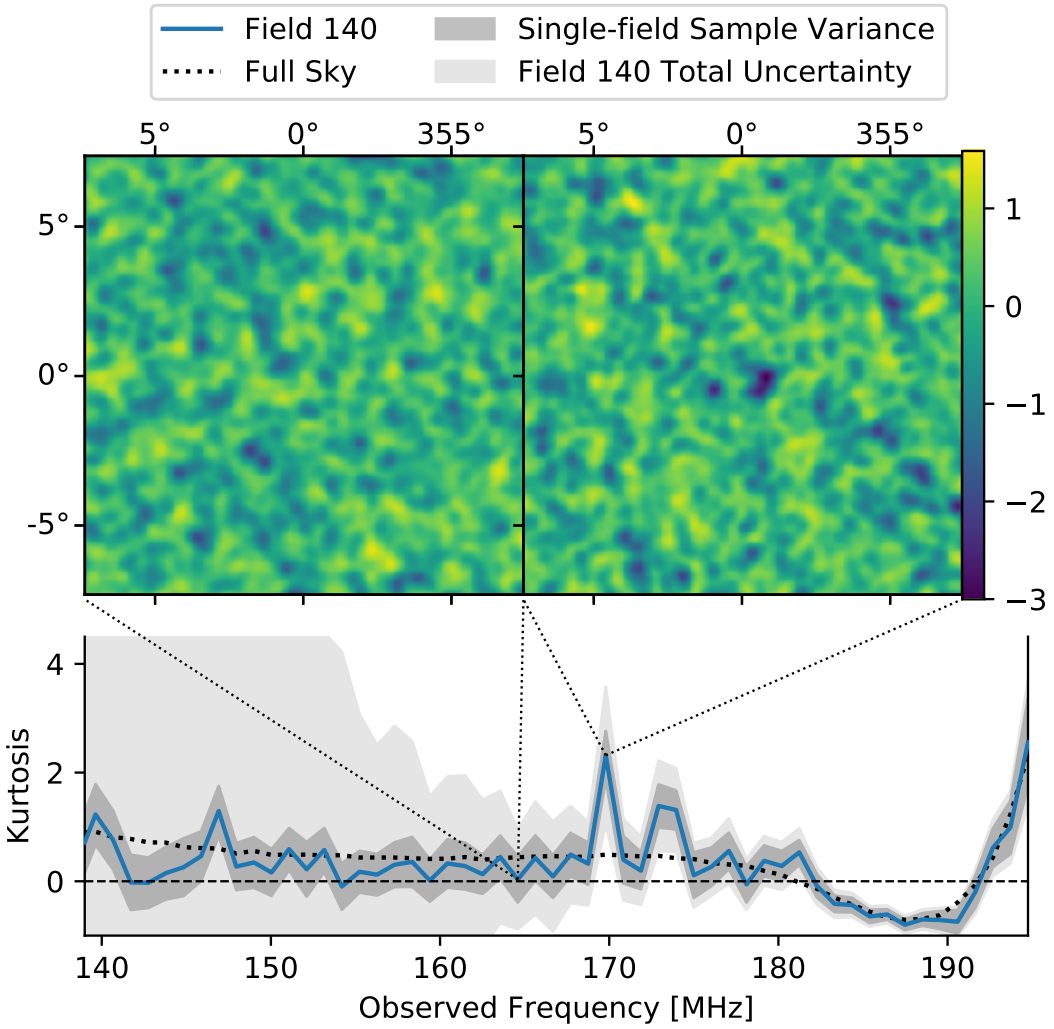

Figure 10. Illustrating the correlation between strong sample variance fluctuation in the single-field measurement of kurtosis and the outlying cold or hot spots in the observed field. The bottom panel shows the kurtosis measured from field 140 from HERA350 Core simulation with 1-MHz frequency binning applied (solid line), overlaid on top of a 1-σ single-field sample variance uncertainty (dark shade) and total uncertainty (light shade), and the expected full sky kurtosis (dotted line). The top two panels show maps of the underlying brightness temperature signal at ~170 MHz, where the kurtosis rises above the sample variance uncertainty (right), and at ~165 MHz, where the kurtosis is near zero (left). The outlying cold spots perturbs the tail of the PDF, causing kurtosis to rise. This statistical feature could potentially be used as a bubble indicator.

2.8 Summary

In this chapter, we have performed sensitivity analysis of HERA to 21 cm one-point statistical probes to the EoR using realistic mock observations of redshifted 21 cm brightness temperature fluctuations.

We develop a tile-and-grid method that transforms a suite of small 21 cm simulation cubes into a full-sky lightcone input model that matches the dimensionality of the observational data. We incorporate the angular resolution effects of all of the planned build-out stages of HERA to gauge the sensitivity of the array as it grows in size. We use simple Gaussian smoothing to incorporate the array angular resolution, using multiple kernel sizes that match angular resolutions of the different build-out stages. The span of resolutions also allows us to study their effects on the statistics. Apart from the variance and skewness that have extensively been covered in previous studies, we also measure kurtosis from our mock observations as well as deriving sample variance uncertainty associated with the measurements. Uncertainty from thermal noise is mathematically derived from the framework developed in Watkinson and Pritchard (2014), where we have extended their derivation to kurtosis. We calculate SNR to gauge the sensitivity of the measurement and perform frequency binning and frequency windowing to investigate if the sensitivity can be further improved. We ignore foreground contamination and other systematics in this work, postponing them to future works.

Our results show that measurements of 21 cm one-point statistics by HERA will be sample variance limited throughout reionization for the variance measurements while skewness and kurtosis sensitivities will be limited by thermal noise. Frequency binning can be used in all measurements to improve the sensitivity. In addition, frequency

windowing can be used in the measurements, particularly in the variance, to further improve the sensitivity once thermal noise has been reduced below the uncertainty from sample variance. However, care must be taken to not use a bin or a window size that is too large to avoid redshift evolution. In addition, all build-out stages of HERA will be able to measure variance with high sensitivity, and HERA128 and above will also be able to measure skewness and kurtosis.

An introduction of kurtosis into our analysis has led us to identify kurtosis peaks as potential indicators of outlying cold or hot spots in individual fields of observations. Kurtosis will sharply rise when a few hot or cold outlying regions appear on top of the underlying Gaussian-like signal in the observed field. Further investigation of this feature is beyond the scope of this work.

Although we only focus on HERA in our analysis, our results should be applicable to future arrays such as the SKA. In particular, the thermal uncertainty will be lower and the signal strength and sample variance uncertainty will be further improved due to its higher angular resolution.

Chapter 3

21 CM ONE-POINT STATISTICS IN A FOREGROUND AVOIDANCE REGIME

Although we showed in the previous chapter that the completed HERA array should have sufficient sensitivity to measure 21 cm one-point statistics, we based our conclusion on an assumption that contaminations from astrophysical foreground sources can be perfectly removed. In practice, removal of foreground contamination is, perhaps, the most challenging aspect of 21 cm observations.

The primary sources of foreground contamination in 21 cm observations are: synchrotron radiation from our own Galaxy, extragalactic radio galaxies, Galactic free-free emission, and Galactic radio recombination lines. Although these sources can be 4 to 5 order of magnitude brighter than the 21 cm signal, a general consensus from initial studies (e.g., Di Matteo et al., 2002, 2004; Oh and Mack, 2003; Gnedin and Shaver, 2004; Zaldarriaga et al., 2004; Morales and Hewitt, 2004; Santos et al., 2005; Wang et al., 2006; McQuinn et al., 2007) is that they are either spectrally smooth along the line of sight dimension or at known frequencies that can be easily modified, and none of their spectra mimics the spherical symmetry of the EoR spectra. The spectrally smooth astrophysical foreground is expected to be contained within the lower line-of-sight wavenumber in the Fourier transform k space. Thus, the foreground could be modeled and subtracted from the data.

Leveraging this spectral smoothness of the foreground is the heart of the foreground subtraction strategy for EoR analysis. Under this basis, the Galactic foreground spectra can be modeled as a directional-dependent power law with a different

spectral index for each line of sight, while the extragalactic foreground from radio galaxies can be modeled as a summation of power law spectra of different spectral indexes to account for overlapping sources in a single line of sight. Over the past decade, a large body of literature has developed several different methods to model and subtract the foreground (e.g., Morales et al., 2006; Bowman et al., 2009; Liu et al., 2009; Liu and Tegmark, 2011; Chapman et al., 2012, 2013; Dillon et al., 2013; Wang et al., 2013), but the lack of good foreground observations in 21 cm observing frequencies make it currently difficult to build models with sufficient accuracy. The situation may change within the next few years when a few new meter-wavelength foreground surveys, such as the GaLactic and Extragalactic All-sky Murchison Widefield Array (GLEAM; Hurley-Walker et al., 2017) and the LOFAR Multifrequency Snapshot Sky Survey (MSSS; Heald et al., 2015), are complete.

Nevertheless, the true challenge in modeling the foregrounds and performing foreground subtractions is complication from the interaction between the foregrounds and the frequency-dependent instrument responses known as mode-mixing. The chromatic instrument responses can add structure to astrophysical foreground sources, throwing foreground power into higher line-of-sight k to obscure the EoR spectra. It was first identified by Bowman et al. (2009), who showed that chromatic sidelobe responses interacting with residual foreground sources can produce ripples of foreground power across the line-of-sight k dimension. Later, a more precise simulation from Datta et al. (2010) showed that mode-mixing in a multi-baseline interferometer results in the foreground power occupying a distinct wedge-shape region in the cylindrically averaged 2D Fourier space. Several more works (e.g., Trott et al., 2012; Vedantham et al., 2012; Morales et al., 2012; Parsons et al., 2012; Hazelton et al., 2013; Thyagarajan et al., 2015a, 2016) confirm, as well as developing mathematical frame-

work to explain the foreground wedge. All reported observations have also confirmed the existent of the wedge (Pober et al., 2013; Dillon et al., 2014; Beardsley et al., 2016). The mode-mixing effect adds an additional requirement for a very accurate instrument model on top of the already demanding requirement to build the foreground model, making foreground subtraction extremely challenging.

As a result, several analysis have explored the alternative foreground avoidance strategy. The predictable (although hard to correct) behavior of the foreground wedge defines the EoR window, a region in the Fourier k space that is expected to be free from mode-mixing effects. As such, the data outside of the EoR window, i.e., within the wedge, can be completely removed from the analysis to obtain results that are freed from foreground contamination. Recent 21 cm power spectrum results have utilized foreground avoidance strategy, usually coupled with the delay power spectrum technique (Parsons et al., 2012), to yield good results and upper limits (Jacobs et al. 2015; Ali et al. 2015; Paul et al. 2016; Kohn et al. 2018; Cheng et al. 2018; Kolopanis et al. in prep.; Kern et al. in prep.).

In this chapter, we develop a foreground avoidance technique for 21 cm one-point statistics and investigate its effects on the HERA measurements that we developed in Chapter 2.

3.1 Mock Data Sets

We will begin by describing the mock data sets that we will be using in the analysis in this chapter.

We use the simulated observed 21 cm brightness temperature intensity cubes of HERA 350 Core discussed in Chapter 2 as the models of the signal (see Section 2.2 to

2.4). To recap, all signal cubes are 256x256x705 pixels the sky position and frequency coordinates $(\theta_x, \theta_y, \nu)$. The frequency resolution $(\Delta\nu)$ is 80 kHz, yielding 56.4 MHz frequency bandwidth (B) that spans $\sim 138-195$ MHz. The angular pixel size $(\Delta\theta_{xy})$ is $\sim 3.4''$ throughout the bandwidth, oversampling the angular resolution of HERA350 Core by $\sim 6-8$ times.

In Chapter 2, we obtained thermal noise uncertainty on the measurement through analytical method, which assumes that the noise is Gaussian. This assumption may no longer be true after the data (signal and noise) in the foreground wedge has been removed. Therefore, we will perform Monte Carlo simulation to obtain thermal noise uncertainty in the measurement for the analysis here. We generate 500 Gaussian noise cubes for each of the signal cube. The noise cubes have the same dimension as the signal cubes. Each frequency channel in the noise cube is convolved with the same Gaussian-approximation of the instrument response as that we used to add instrument effects to the signal cubes. After the convolution, the noise power is adjusted to yield noise RMS per channel that match the analytical prediction.

Since we will be experimenting with foreground avoidance techniques, no actual foreground models will be used in the analysis. Modeling the foregrounds is also very difficult as discussed above.

3.2 Foreground Avoidance Filter

To remove foreground contaminated k modes from the data, we will form a foreground avoidance filter as a cube in the k space with zero and one for pixels inside and outside of the foreground wedge, respectively, multiply this filter to the Fourier representations of the sum of the signal and noise cubes and revert back to real space

for measurements. The actual operation will require knowledge on the shape of the foreground wedge, as well as effects from from the Fourier transform window. We will first describe the relationship between coordinates in the image and k spaces and mathematically define the boundaries of the foreground wedge, and, then, show that a rolling implementation of the filters is best at retaining the dynamic range and structural coherency of the original signal.

3.2.1 The k Space

Adapting from Morales and Hewitt (2004), a three-dimensional Fourier transform can be applied to an image cube of brightness temperature intensity fluctuations in the sky position and frequency coordinates $(\theta_x, \theta_y, \nu)$ to obtain its Fourier representation in the interferometric baseline coordinates (u, v, η),

$$I(\theta_x, \theta_y, \nu) \overset{\mathcal{F}}{\longleftrightarrow} \tilde{I}(u, v, \eta), \tag{3.1}$$

where we have denoted the Fourier quantity with $\sim$ accent. The baseline coordinates are reciprocals of the sky position and frequency coordinates in the Fourier transform convention that we use. The Fourier representation in comoving wavenumber space $\tilde{I}(k_x, k_y, k_z)$ can be obtained by mapping the baseline coordinates to the comoving wavenumber coordinates (k_x, k_y, k_z) using the following relationships that account for cosmology,

$$k_x = \frac{2\pi}{D_M(z)} u \qquad = \frac{2\pi}{D_M(z)} \frac{1}{\theta_x}, \tag{3.2}$$

$$k_y = \frac{2\pi}{D_M(z)} v \qquad = \frac{2\pi}{D_M(z)} \frac{1}{\theta_y}, \tag{3.3}$$

$$k_z = \frac{2\pi H_0 \nu_{21} E(z)}{c(1+z)^2} \eta \quad = \frac{2\pi H_0 \nu_{21} E(z)}{c(1+z)^2} \frac{1}{\nu}. \tag{3.4}$$

Here, ν_{21} is the rest frequency of the 21 cm line (1420.405 MHz). H_0 is the Hubble constant. $D_M(z)$ is the transverse comoving distance. $E(z) = [\Omega_M(1+z)^3+\Omega_k(1+z)^2+\Omega_\Lambda]^{1/2}$ is a standard term in cosmology, and z is the reference redshift of the data cube, which we derive from the mean frequency. We also define $k_\parallel = k_z$ and $k_\perp = \sqrt{k_x^2 + k_y^2}$ as the line-of-sight and radial k coordinates. In analysis, the EoR power spectrum is formed in $(k_\parallel, k_\perp)$ space by cylindrically averaging the Fourier representations of the 21 data along $k_\parallel = 0$ to leverage the symmetry of the EoR spectra for sensitivity improvement. We will discuss the geometry of the foreground wedge in this $(k_\parallel, k_\perp)$ space as it is simpler and follows the standard convention used in literature but will later revert back to (k_x, k_y, k_z) space when building the foreground avoidance filter.

Due to the Fourier coordinate mapping in Equation 3.2 to 3.4, the measurable $k_\perp$ and $k_\parallel$ values are limited by frequency and spatial coordinates (and their Fourier duels) and probe the signals at different size scales. Specifically, lower $k_\perp$ and $k_\parallel$ probe larger size scales along the angular and line-of-sight dimensions. The minimum and maximum $k_\parallel$ are determined by the frequency bandwidth and frequency resolution, whereas the minimum and maximum $k_\perp$ are determined by the angular resolution and field of view of the intensity map. These limits are shown as the four bounding boxes in Figure 11. Instrumentally, the limits on $k_\perp$ are determine by the baseline lengths.

3.2.2 The Shape of the Foreground Wedge

With the above coordinate framework, contamination from a foreground source with a smooth spectrum at an angle θ from the field center will appear in the $(k_\parallel, k_\perp)$ space as a line (or a shell of two concentric cones with their tips touching at $(k_x, k_y, k_z) = 0$ in the 3D k space) that follows a remarkably simple linear relationship

(Morales et al., 2012),

$$k_{\parallel} = \sin(\theta)\frac{H_0 E(z) D_M(z)}{c(1+z)} k_{\perp}. \tag{3.5}$$

Figure 11 illustrates the consequences of this relationship. A foreground source near the field center will produce a line of contamination with a shallow slope angle (dotted lines). Another foreground source far from the field center will produce another line of contamination with a steeper slope (dash-dotted line). A foreground source at the horizon, $\theta = \pi/2$ radian, will produce a line of contamination that defines the maximum boundary of the foreground wedge (solid line),

$$k_{\parallel\ \mathrm{Max}} = \frac{H_0 E(z) D_M(z)}{c(1+z)} k_{\perp}. \tag{3.6}$$

As a results, multiple sources at different angles across the field of view will produce multiple lines of contamination with different slope angles that fill up the $(k_{\parallel}, k_{\perp})$ space to form the foreground wedge (dark gray shade). Data inside the foreground wedge will be contaminated. The EoR window outside of the foreground wedge has been shown to be free from contamination due to mode mixing although calibration errors and other systematics could bleed the foreground power to the outside of the wedge (Vedantham et al., 2012). If we could control the extent of the foreground sources (or their residuals) to be within a certain angle θ from the field center, a smaller foreground wedge, thus less contamination, would also be possible. Note that we plot Figure 11 in linear $(k_{\parallel}, k_{\perp})$. The 2D power spectrum space is usually plotted in $(\log k_{\parallel}, \log k_{\perp})$, so lines of contamination would appear to move to higher $\log k_{\parallel}$ as the source angle increases (see Figure 4 in Morales et al. (2012)).

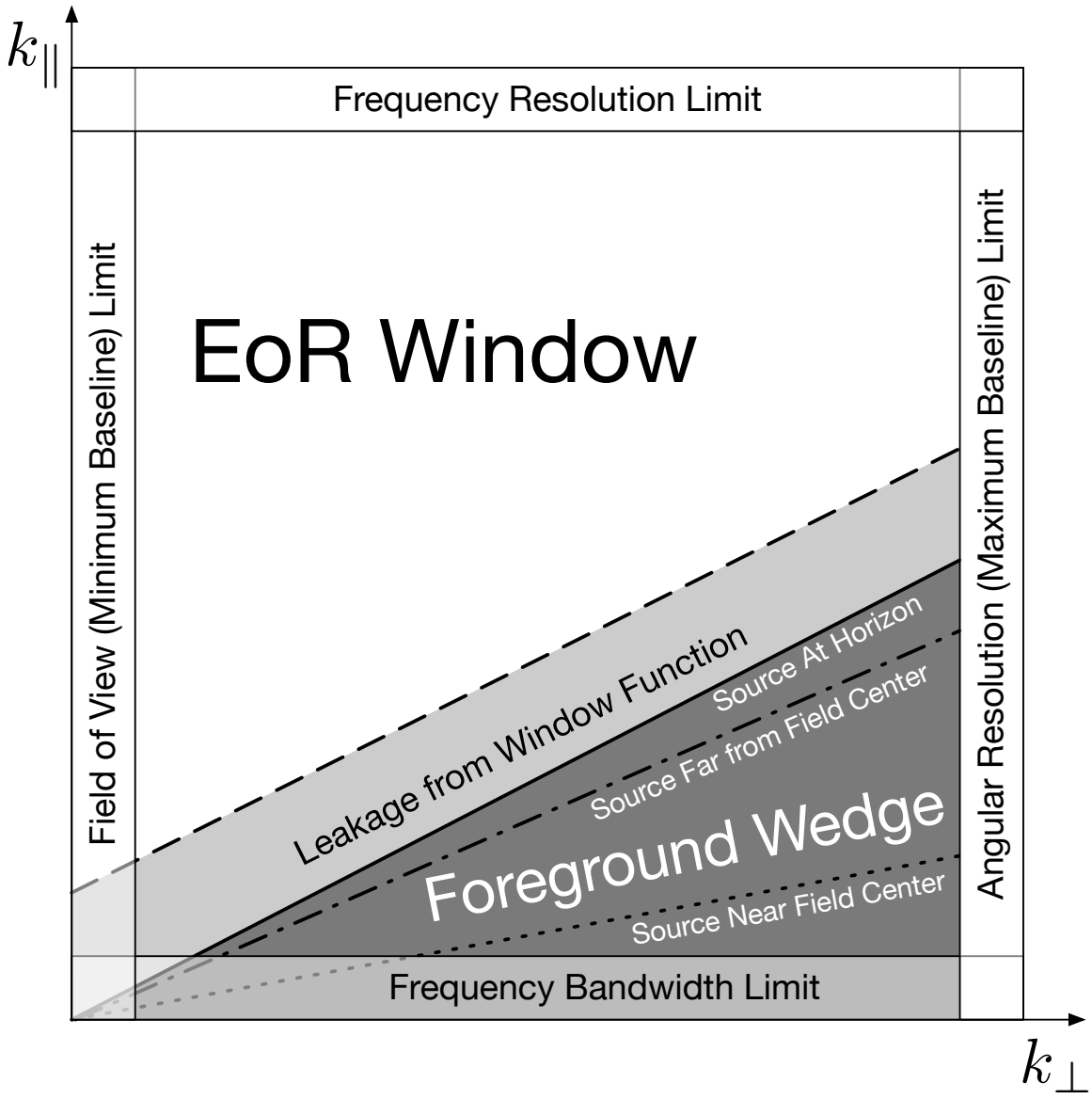

Figure 11. Schematic diagram of the foreground wedge in $(k_{\parallel}, k_{\perp})$ space. Mode-mixing causes power of foreground sources at different angle distances from the field center to appear as lines in $(k_{\parallel}, k_{\perp})$ space, with shallower and steeper slope angles fro sources near the field center and far from the field center, respectively. Leakage from multiple sources across the field will form the wedge-shape contaminated region. The Fourier transform window function will cause additional leakage of the foreground wedge to higher $k_{\parallel}$.

3.2.3 Window Function Leakage and Bandpass Shaping

In addition to leakage due to mode-mixing that gives rise to the foreground wedge, a Fourier transform operation on the data with finite boundaries will smear the spectral responses and cause additional spectral leakage that appear as sidelobe ripples, reducing the dynamic range of the Fourier transform spectrum. For example, a Fourier transform of a constant signal with infinite boundaries yields a delta-function spectral response at $k = 0$ with an amplitude equal to the constant. On the other hand, a Fourier transform of the same constant signal within a finite rectangular window will produce a sinc response. The lower peak amplitude and sidelobes of the sinc response will result in lower dynamic range. This effect, known as window function leakage, is an important problem in the EoR analysis because it means that foreground contaminations will be thrown to higher $k_{\parallel}$ outside of the foreground wedge once the data has been Fourier transformed.

To reduce spectral leakage, the observing bandpass can be shaped into a non-rectangular window by multiplying the data cube with a non-rectangular function along the frequency dimension before Fourier transforming, but this operation, sometimes refer to as bandpass shaping, comes at a cost of lower spectral resolution. This is because any non-rectangular windows have broader main lobe responses than a rectangular window that will smear spectral structures into the neighboring k values albeit the reduced sidelobe ripples.

Several studied have experimented with different window functions to shape the bandpass of the EoR data. Vedantham et al. (2012) showed that a Blackman-Nuttal window can reduce spectral leakage in the EoR window to improve dynamic range by 3 to 4 order of magnitude. The spectral resolution of a Blackman-Nuttal window

function is, however, fairly poor. Thyagarajan et al. (2013) showed that a modification can be made to the Blackman-Nuttal function to improve its spectral resolution while retaining good dynamic range. Regardless, the simpler Blackman-Nuttal (or its close cousins Blackman-Harris) is still a popular choice in the most recent power spectrum analysis.

For simplicity, we will use a Blackman-Nuttal function to shape the bandpass of our data cube but account for smearing from the reduced resolution by shifting the wedge boundary to higher $k_\parallel$. This shifting is equivalent to adjusting the $k_\parallel$ intercept in Equation 3.5, which we indicate in a modified expression for the wedge boundary below with a variable β,

$$k_\parallel = \sin(\theta)\frac{H_0 E(z) D_M(z)}{c(1+z)} k_\perp + \beta. \tag{3.7}$$

The leakage due to the window function and the adjusted wedge boundary to account for it are shown in Figure 11 as the light gray region and the dashed line above the foreground wedge.

Substituting back $k_z = k_\parallel$ and $k_\perp = \sqrt{k_x^2 + k_y^2}$ will yield the same relationship in (k_x, k_y, k_z) space,

$$k_z = \sin(\theta)\frac{H_0 E(z) D_M(z)}{c(1+z)} \sqrt{k_x^2 + k_y^2} + \beta. \tag{3.8}$$

3.3 Noiseless Foreground Avoided Measurements

We can use Equation 3.8 to build a foreground avoidance filter as a cube in (k_x, k_y, k_z) space with zero and one for pixel weights inside and outside of the foreground wedge, respectively. We can multiply our data cube with a Blackman-Nuttal function along the frequency dimension to shape the data bandpass, Fourier transform

to k space and multiply by the filter to remove foreground contaminated data. Then, to obtain the foreground avoided data in the sky position and frequency space, we inverse Fourier transform and divide the resulting data cube with the same Blackman-Nuttal function used during the forward transform to undo the window function. Finally, we can make variance, skewness and kurtosis measurements.

However, the measurements will be biased due to the transform-multiply-transform-divide operation described above. We also have to make a few decisions when building the foreground avoidance filter. What should we assume for the maximum source angle θ? How much should we account for spectral leakage from window function, and how does that translate into the β parameters? Which are good ranges of frequency bandwidths to apply the filters? In other words, is it better to apply the filters on the full 54-MHz data bandwidth or on a smaller subband of the data? The choices on these parameters will affect not only the physical appearance of the filter but also the bias on one-point statistics measurements. In this section, we will investigate these questions and present measurement from noiseless simulation for references.

3.3.1 Filter Bias

We select subbands of one of our signal cubes (no noise) centered at $\sim$ 187 MHz with the bandwidths of the subbands (W_{BW}) spanning 2 to 16 MHz in 2 MHz increments. Then, we construct two sets of foreground wedge filters, one set with $\theta = 5$ degree, corresponding to the field of view of the HERA instrument, and $\beta = 0$, 1, 2 and 4 times Δk_z, and another set with $\beta = 0$ times Δk_z and $\theta = 5$, 15, 60 and 90 degrees, apply them to the selected signal cubes, and measure variance skewness and

kurtosis from the filtered outputs. Note that the bandwidths of the subbands also define the bandwidths of the filters, which are equal.

The frequency slices of the filtered intensity maps with $\theta = 5$ deg and $\beta = 0$ Δk_z are shown in Figure 12. Figure 13 show foreground avoidance measurements with the $\theta = 5$ deg and $\beta = 0$ Δk_z filter at different filter bandwidths along with measurements from the unfiltered signal cube to illustrates these points.

To make it easier to quantify the bias induced in the one-point statistics from the foreground avoidance filters compared to a perfectly foreground removed map, we define,

$$\text{Fractional Bias} = \frac{\text{Statistics from Filtered Map} - \text{Statistics from Ideal Map}}{|\text{Statistics from Ideal Map}|}. \quad (3.9)$$

Thus, the fractional bias is zero if the measurements are not biased, and is positive or negative if the measurements are positively or negatively biased. The fractional biases of the measurements in Figure 13 are shown in Figure 14, focusing on the central 8 MHz of the band. Figure 15 compares fractional bias on variance, skewness and kurtosis at the center of the subband.

The first clear effect from foreground avoidance filtering is that signals at the edges of the bandpass are saturated due to the window function un-weighting, resulting in saturated one-point statistics measurements. In the middle of the band, the foreground avoidance measurements are more closely resemble the ideal maps but become more biased as the measured frequencies deviate from center of the subbands and as the bandwidths of the subbands increase. The measured variance decreases and becomes more biased as the filter bandwidth increases. The skewness, however, appear to be maximally biased at 8-MHz bandwidth, contradicting the general trend statement. This may be due to more of the highly skewed signals at higher frequencies getting mixed into the unfiltered k modes. The measured kurtosis follow the general

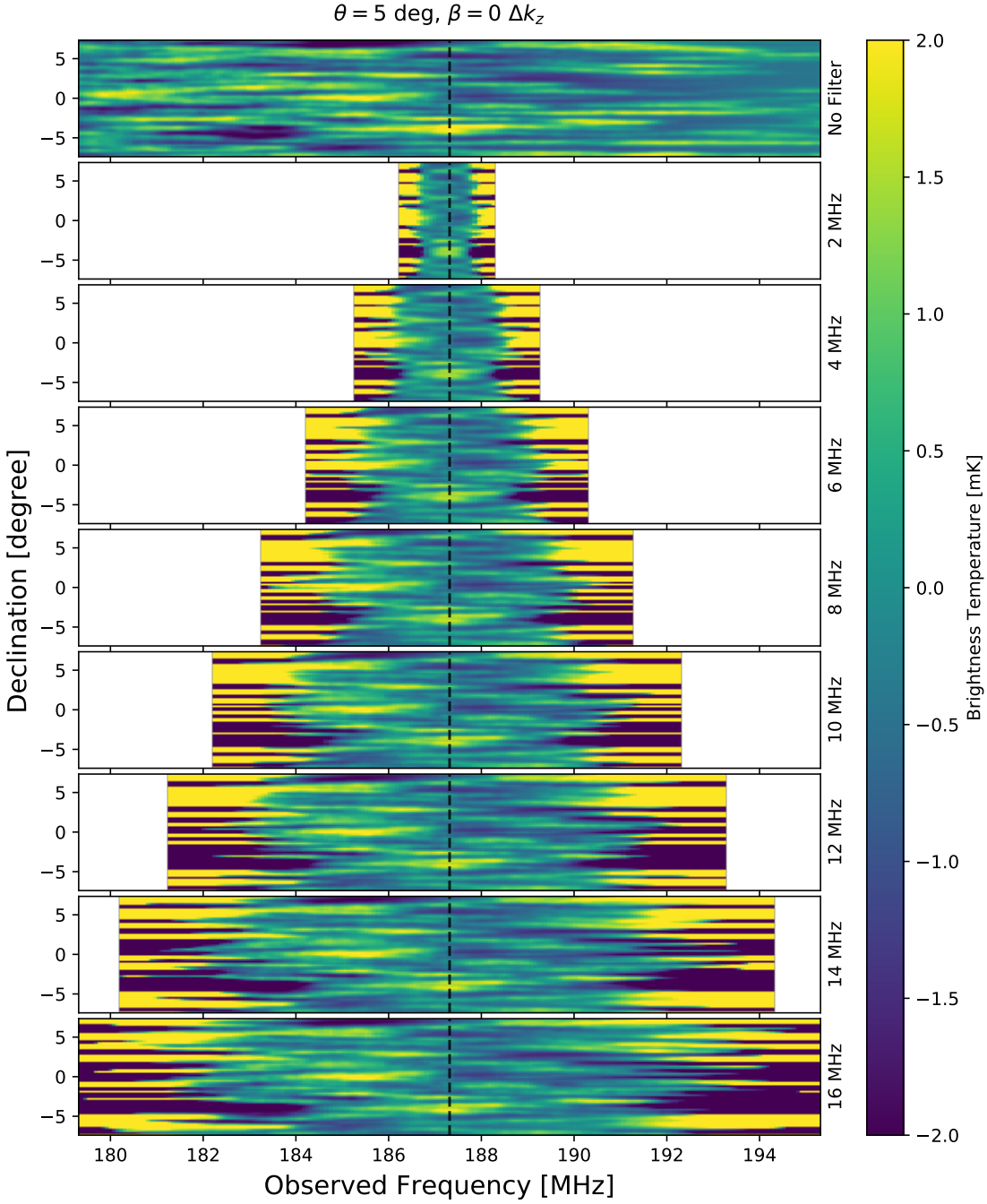

Figure 12. Recovered maps after foreground filtering of different bandwidths. The filters used in this demonstration assume that foreground sources are contained within the HERA field of view ($\theta = 5$ degree) and there is no leakage from window function ($\beta = 0$). Notice the saturation at the edges of the subband due to window function unweighting. In the middle of the bands, the foreground filtered maps appear to have slightly reduced dynamic range but are indistinguishable from the unfiltered map.

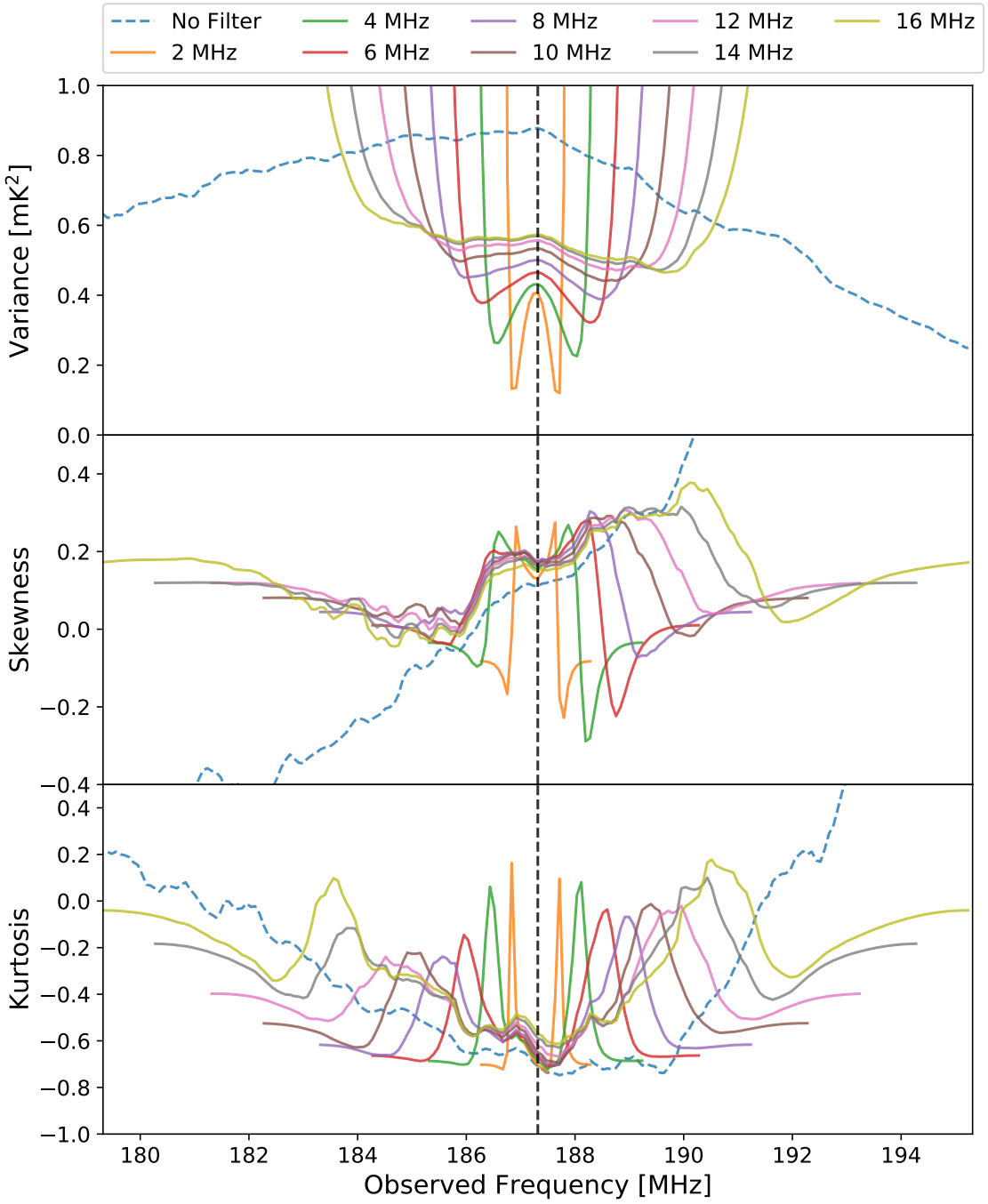

Figure 13. Recover statistics after foreground filtering of different bandwidths, measured from maps in Figure 12. The overshoot and saturation at the edges of the subbands are caused by window function unweighting and should be discarded from actual measurements. Statistics measured from the center channel of the subbands are the least biased.

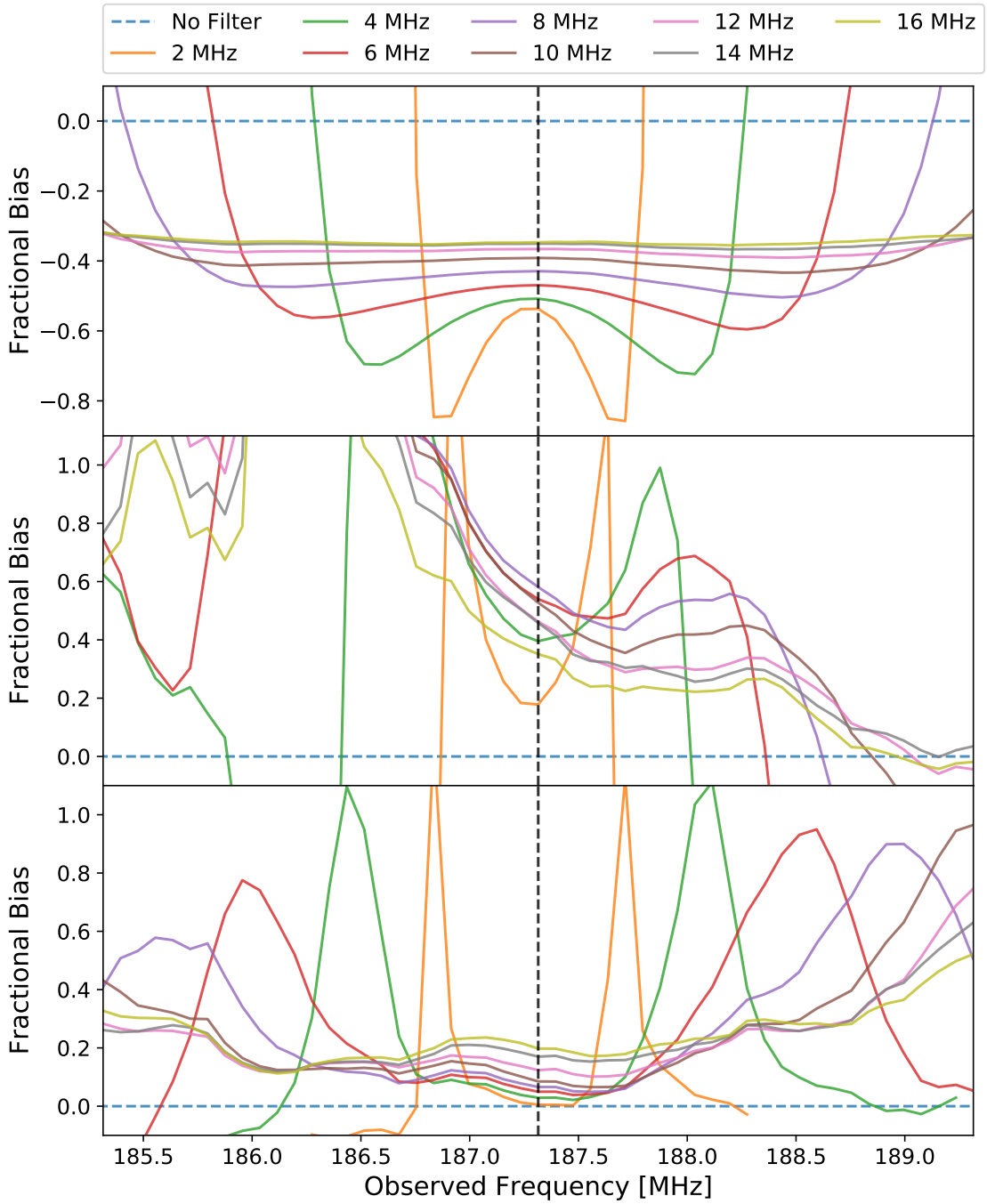

Figure 14. Fractional bias of measurements in Figure 13. The range of observed frequencies in the x-axis is cropped to the central 8 MHz of the bandpass. Statistics measured at the center of the subband are the least biased.

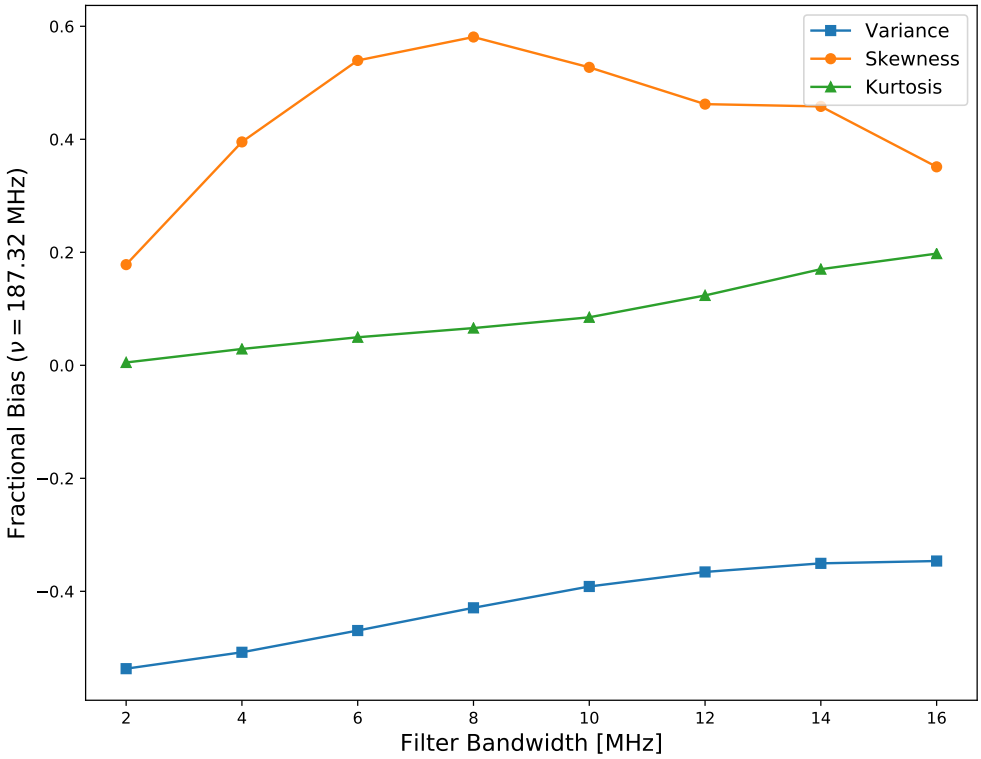

Figure 15. Fraction bias in Figure 14 at center of the subbands as a function of filter bandwidths. The bias in variance and kurtosis increases as the filter bandwidth in creases. The bias in skewness is peak at 8 MHz.

trend seen in the variance with stronger bias as the filter bandwidth increases. We repeat our experiment with subbands center at $\sim$ 160 MHz, where the signal across the subbands exhibit similar skewness, and see stronger bias in all one-point statistics as the bandwidths increase. We also notice through the repeated experiment that the bias is dependent of the signal.

The results here imply that smaller subbands are better when performing foreground avoidance filtering. This implication, however, must be taken with caution. Since the frequency resolution, spatial resolution and field of view of our image cubes

are fixed, the maximum $k_\parallel$, maximum $k_\perp$ and $k_\perp$ pixel size are also fixed, and the foreground wedge will span the same region in k space regardless of the frequency bandwidths. Smaller bandwidths will yield poorer $k_\parallel$ resolution and cause more leakage at higher $k_\parallel$ due to window function smearing. Since our demonstration here only contains signal, this effect causes signal power in low $k_\parallel$, which correspond to non-Gaussian structure, to leak to higher $k_\parallel$ that were not filtered, resulting in less bias in the measured skewness and kurtosis. If foreground were present, the foreground power would also leaked to higher $k_\parallel$.

The question would, then, become whether residual foreground power would be stronger or less than residual signal power after filtering. A complete answer to this question will require modeling the foreground and signal with full radio interferometric simulations, which are extremely challenging due to reasons discuss in the beginning of this chapter. To provide an order of magnitude answer, we apply the two filter sets used in the demonstration here to an analytic foreground model by Zheng et al. (2017), that has been Gaussian smoothed to the instrument resolution but contains no wedge, and compare the residual foreground power to the residual signal power at high $k_\parallel$ after filtering. We found that an 8-MHz filter bandwidth yield residual signal power that is 10^4 greater than residual foreground power in the high $k_\parallel$, which should be plentiful to detect the EoR signal even in the presence of noise. Therefore, we will use an 8-MHz filter bandwidth for the rest of our investigation. Using narrower bandwidths, such as 4 MHz, may also be sufficient, but very narrow bandwidths, such as 1 or 2 MHz, will leave very small EoR window to work with and may not provide sufficient sensitivity to detect the residual signal in the presence of noise.

The effects from the other two filter parameters – the maximum angle of foreground source from the field center (θ), the extra shift in line-of-sight dimension to

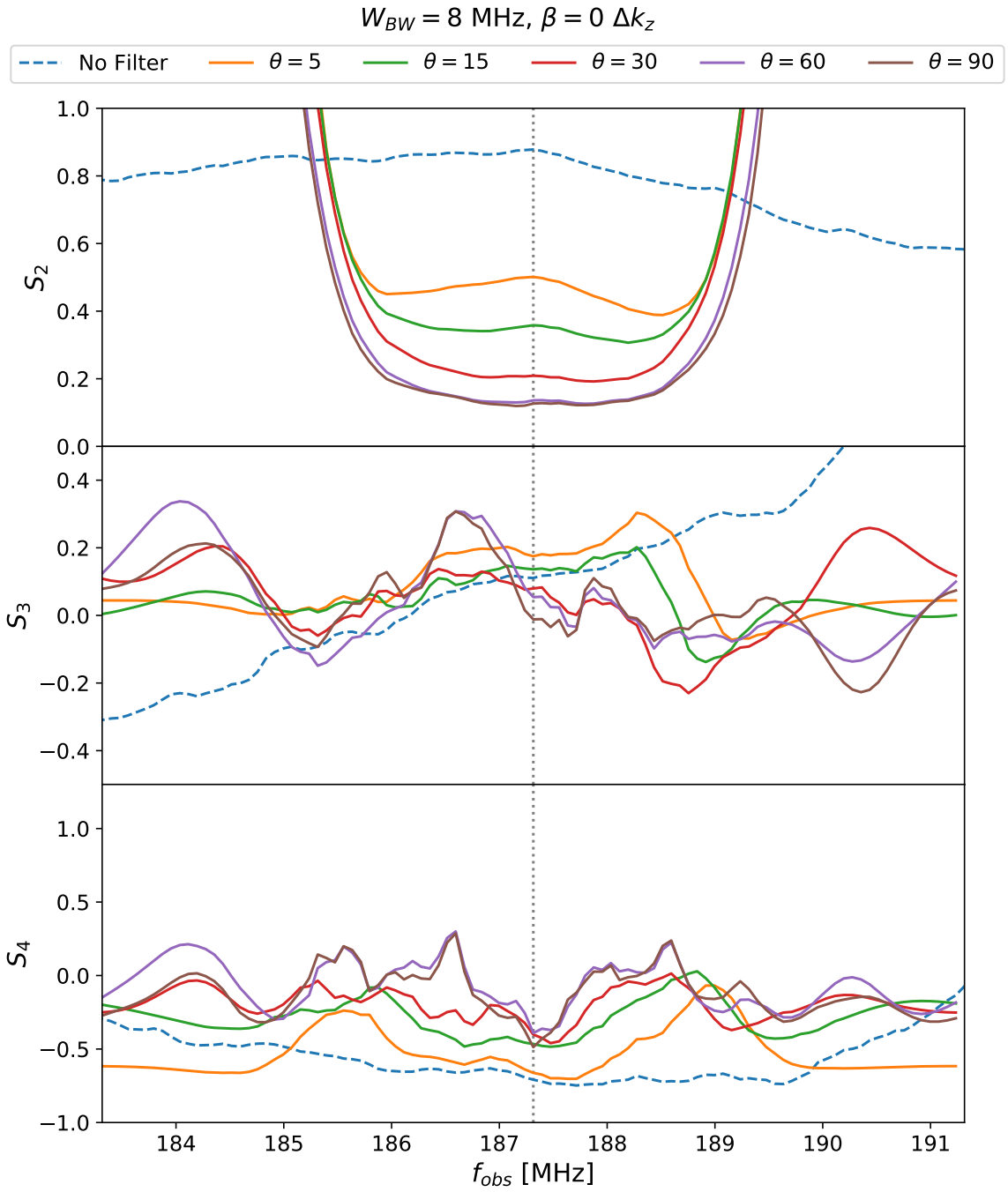

Figure 16. Recovered statistics after foreground filtering of different values for the assumed maximum angles of foreground sources from the field center θ. All filters used have 8 MHz bandwidths and assume no leakage from window function. The top, middle and bottom panels show variance, skewness and kurtosis. An increase in θ quickly increases the bias on the statistics.

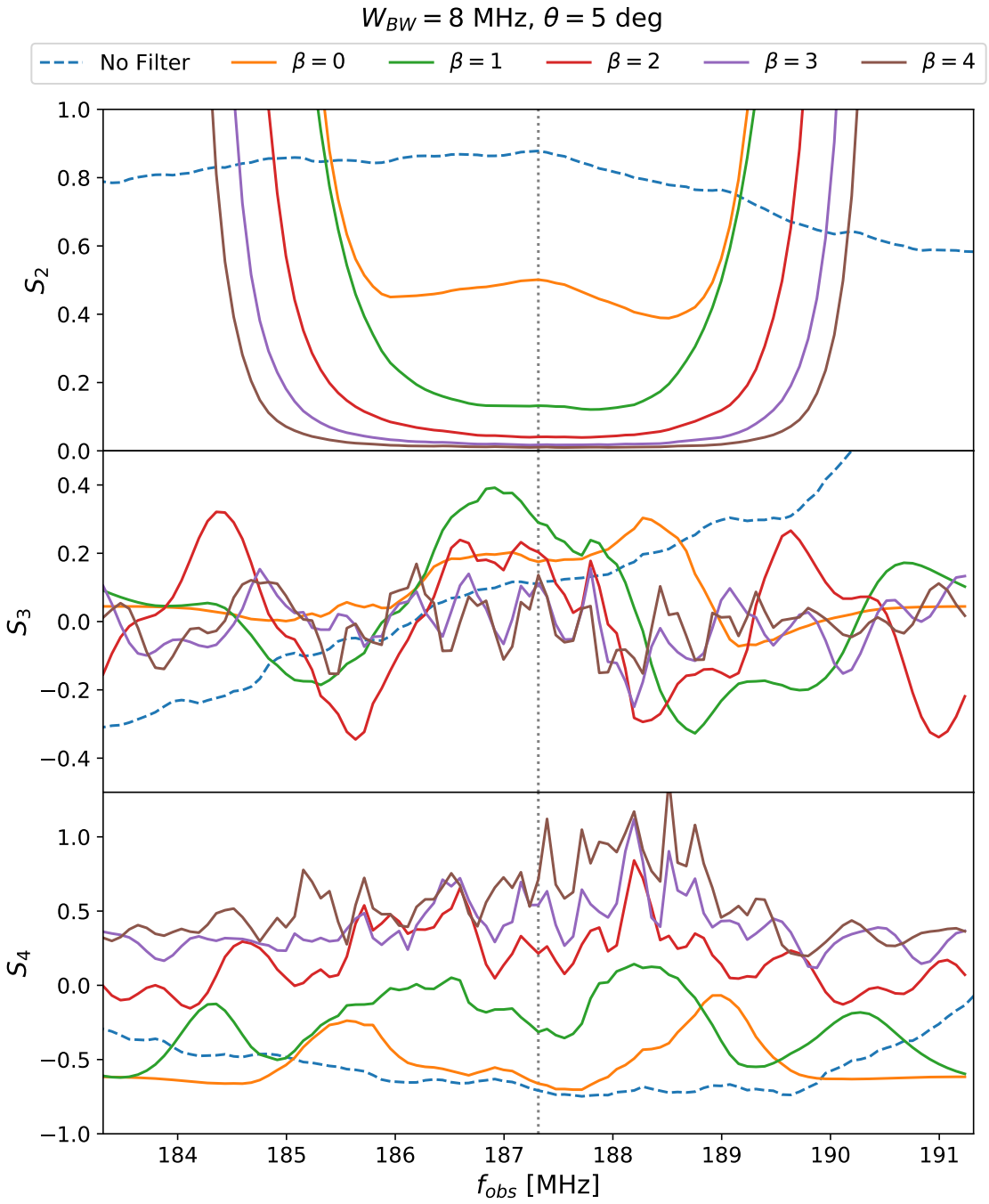

Figure 17. Recovered statistics after foreground filtering of different assumed window function leakage β. All filters used 8 MHz bandwidths and assume 5-degree maximum extent of foreground sources from the field center ($\theta = 5$ degrees). The top, middle and bottom panels show variance, skewness and kurtosis. Similar to an increase in θ, an increase in β quickly increases the bias on the statistics, but a slight increase in β appear to induce more bias than an increase in θ.

account for spectral leakage (β) – are more clear. To illustrate, Figure 16 show measurements from an 8-MHz filtered signal cube with $\beta = 0$ times Δk_z and varying θ, and Figure 17 show measurement from the same input signal cube and filter bandwidth but with $\theta = 5$ degree and varying β for comparison. As the filter parameters become more aggressive from the use of higher β and θ values, more data in the lower $k_{\parallel}$ modes are removed, and all measured one-point statistics are washed out. Particularly, the variance flattens across the band, while skewness and kurtosis appear as random fluctuations near zero. We will revisit this behavior when discussing further results in the following sections. Regardless, these measurements suggest that foreground avoidance filter will results in strong bias that washes out EoR signatures in one-point statistics unless the minimum wedge filters can be used, which require reducing the foreground wedge to k modes that are lower than the horizon limit, as well as minimizing spectral leakage through optimization of the window function.

3.3.2 Rolling Filter Implementation

Although the strong bias in foreground avoidance filtered measurements discussed in the previous section may sound discouraging, one characteristic of the bias hint a simple way that may improve the measurements. We notice that the center frequency of the band always yield the minimum bias because the weight of the window function at the center frequency is closest to 1. Therefore, we can optimize the bias across the frequency bandpass of the data by using a rolling filter technique, which can be done as follow.

- First, the filter is constructed and applied over a chosen subband as in our

demonstration in the previous section, but only an output image at the center frequency of the subband, which is the least biased, is kept.

- Next, the filter subband is shifted up or down in frequencies. A new filter is reconstructed to match the redshift of the new subband and applied. An output image at the center channels is kept as above
- The above two steps are repeated as we roll the filter subband across the band-pass.
- Finally, all of the saved outputs are stitched together as a function of frequency to form a foreground filtered image cube that with minimal bias across the band.

This technique is similar to the overlap-save method (Hanumantharaju et al.) commonly used in signal processing. Note that the rolling filter simply optimizes bias to the minimally possible level across the band but does not, and cannot, reduce the bias beyond the possible outcome of filter.

Following the discussion in the previous section, we will apply rolling filters to 20 noiseless signal cubes to develop the baseline expectation on the foreground avoided measurements that could be measured from drift scan observations in the absence of thermal noise. We will use an 8-MHz filter bandwidth, which is within optimal ranges of bandwidths as discussed, and combinations of filter parameters from the cartesian product of $\theta = (5, 30, 90)$ and $\beta = (0, 2, 8)$. We choose these specific sets of parameters to represent some possible observational cases. $\theta = 5$ and 30 are approximately equivalent to assuming that foreground sources can be controlled to be within the FWHM and the first null of the primary beam of HERA respectively, while $\theta = 90$ makes no assumption on the extent of the foreground sources, i.e. assuming that foreground sources occupy the whole sky . $\beta = 0$, 2 and 8 represent optimistic, practical and conservative assumptions on spectral leakage from the window function.

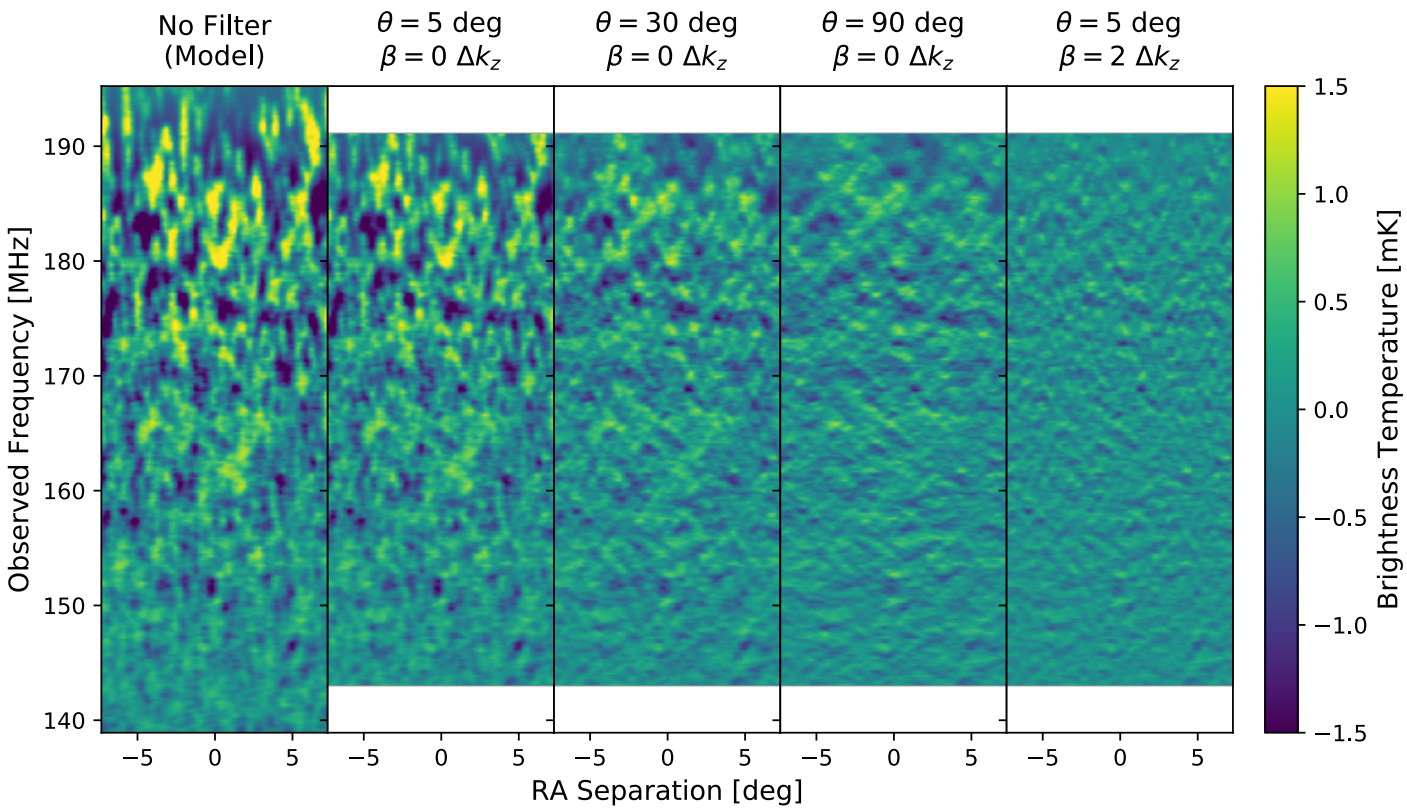

Figure 18. Comparing 21 cm fluctuations after rolling foreground filtering of different parameters. With minimal filtering ($\theta = 5$ degree and $\beta = 0$, 2nd panel from the left), a rolling filter method effectively retains structural coherency and dynamic range of the unfiltered brightness temperature maps. Extended structures corresponding the ionized and overdense regions are washed out as the slope of the foreground wedge increases. Shifting the boundary of the foreground wedge to higher k_z to account for window function leakage washes out most of the signal even with small wedge slope. This implies that we must control leakage from window function through other means to be able to use foreground avoidance filtering.

Figure 18 show frequency slices of the output after rolling filters of various parameters have been applied to the same input signal cube. Note on how the filters with more aggressive parameters washed out more non-Gaussian structure in the brightness intensity fluctuations.

We follow the procedure in Chapter 2 to derive drift scan measurements. In short, variance, skewness and kurtosis measured from all 20 filtered signal cubes are averaged and used as drift scan measurements. The results are shown in Figure 19 to 21.

In general the trends that were apparent when we discussed the filter bias in Section 3.3.1 are still applied. As the filter parameters become more aggressive, the measured variance reduces to near zero values, and the measured skewness is washed out into random fluctuation near zero. Interestingly, the measured kurtosis abruptly increases as a function of frequency near the end of reionization with more aggressive filters that account for spectral leakage ($\beta = 2$ and 8). However, it is very clear from Figure 18 that filtering with $\beta > 0$ washes out most of the ionized and overdense regions that are responsible for rise of skewness and kurtosis at the end of reionization. Therefore, the increases in kurtosis here is simply due to and implies that the structure concentrated in large k has a heavy-tailed distribution. Whether this feature can be related to reionization is beyond the scope of this work.

In term of the effects from the two primary filter parameters θ and β, increases in β wash out features in one-point statistic significantly more than increases in θ. Even with $\beta = 2$, most features are removed unless foreground sources are assumed to occupy only regions within the beam FWHM. This implies that we must try to resolve window function spectral leakage through other means that are not extending the foreground wedge boundary to higher k. One of the solutions may be to just keep $\beta = 0$ and let foreground spectrum leaked into the measurements window. The leaked

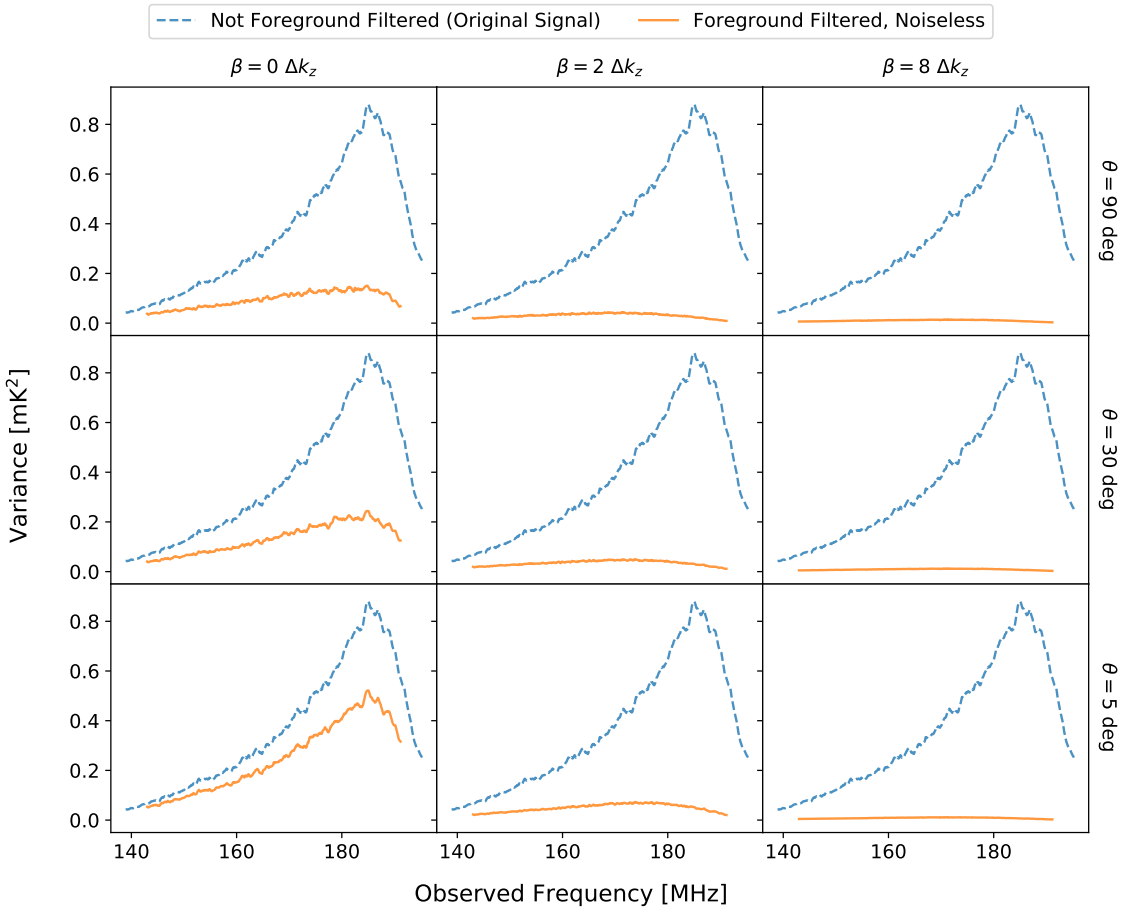

Figure 19. Drift scan variance measured from noiseless, foreground filtered, HERA350 Core simulations (solid lines) in comparison to measurements from the mock observations with no foreground filtering (dashed lines). Different rows from the top to the bottom show measurements after foreground filtering with $\theta = 90$, 30, and 5, which correspond to assuming that the foreground sources are present from horizon to horizon, within the null of the HERA primary beam, and within the FWHM of the HERA field of view, respectively. The measurements in the left column are from simulations with the foreground filters that do not account for window function leakage $\beta = 0$, whereas the measurements in the middle column are from simulations with filters that account for leakage from the Blackman-Nuttal window $\beta = 2$. In addition, measurements from simulations with filters that account for a lot of leakage $\beta = 8$ are shown in the right column to demonstrate an extreme case. As expected, the variance is reduced to near zero as the filters become more aggressive.

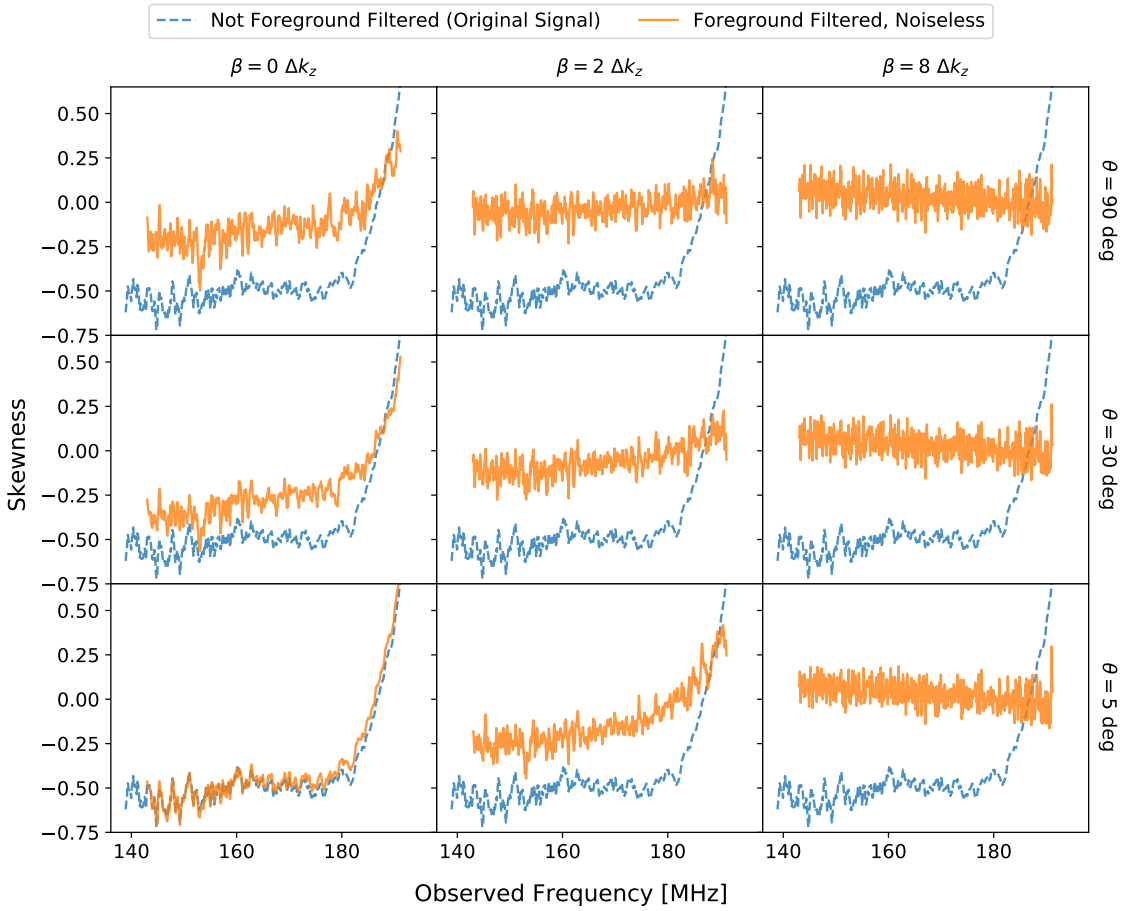

Figure 20. Drift scan skewness measured from noiseless, foreground filtered, HERA350 Core simulations (solid lines) in comparison to measurements from the mock observations with no foreground filtering (dashed lines). Different panels correspond to measurements from the simulations with different foreground filtering parameters, which are described in the main text and in the caption of Figure 19. As expected, the skewness is reduced to near-zero fluctuations as the filters become more aggressive.

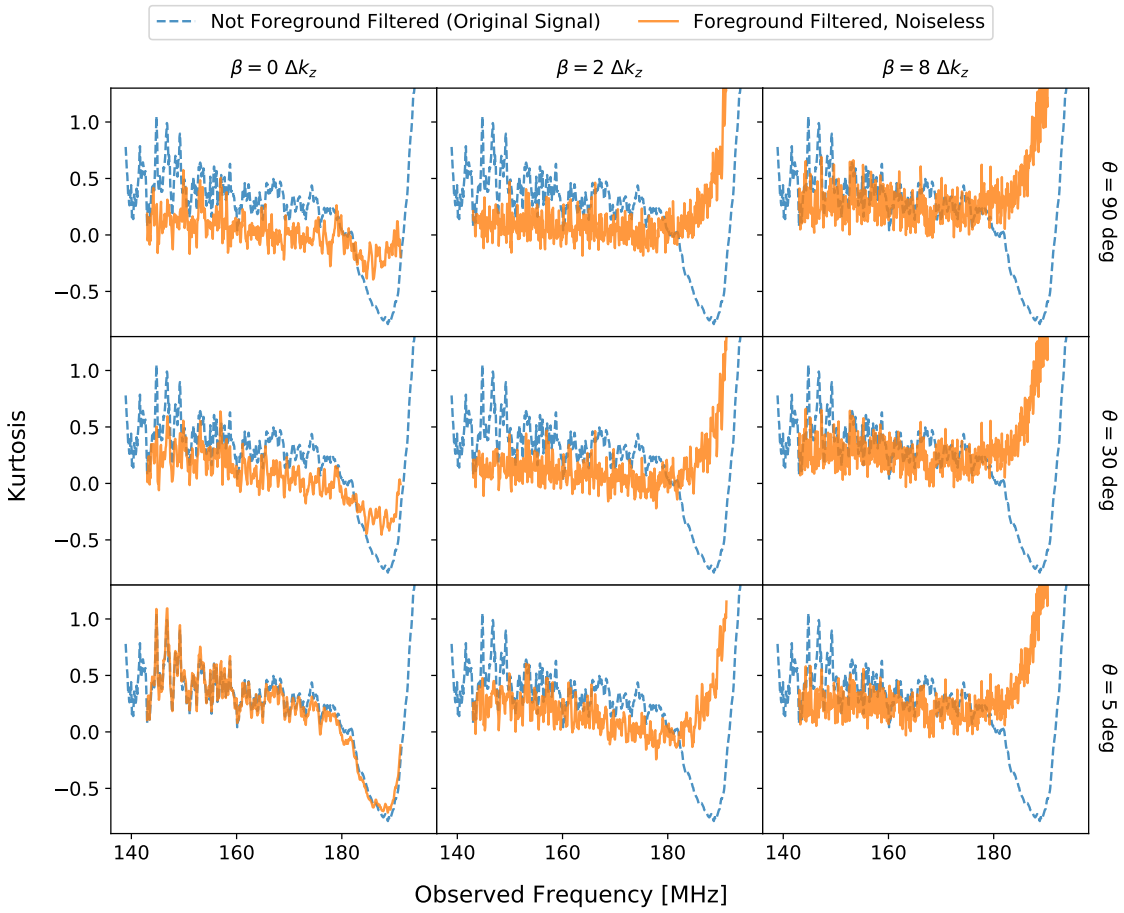

Figure 21. Drift scan kurtosis measured from noiseless, foreground filtered, HERA350 Core simulations (solid lines) in comparison to measurements from the mock observations with no foreground filtering (dashed lines). Different panels correspond to measurements from the simulations with different foreground filtering parameters, which are described in the main text and in the caption of Figure 19. The kurtosis features of the 21 cm signal, such as the dip and rise during the middle of reionization, are washed out as the foreground filters become more aggressive. Interestingly, the kurtosis values near the end of reionization rises more as the filter become more aggressive. This suggests that the structure in the large k that remains after foreground filtering has a heavy-tailed distribution.

foreground power may not affect the measured one-point statistics as much as we have been fearing, depending on the dynamic range between the leakage foreground and the signal and their spectral structure, which could be improved by optimizing the window function. Investigating this, however, will require a good foreground model and is beyond the scope of this work.

3.4 Thermal Noise Bias

Even though the foreground avoidance filters may introduce significant bias on the measured one-point statistics, certain combinations of the filter parameters still yield measurements that are viable. In this section, we will complete the analysis of these measurements by deriving uncertainty from thermal noise.

As we briefly mentioned in Section 3.1, we obtain uncertainties from thermal noise on the foreground avoided measurements through Monte Carlo simulation instead of the analytical approach that we used in Chapter 2. For each of the 20 signal cubes, we generate 500 noise cube that we have smoothed with a Gaussian kernel matching the angular resolution of HERA350 Core to approximate the instrument beam effects, and normalized adjusted the noise RMS per frequency channel to match the expected thermal uncertainty of the array. We assume the noise RMS equivalent to 200 hours of integration time per field, roughly equivalent to two years of operation (see Section 2.1 for discussion). Then, we add a noise cube to a signal cube to form a thermal noise contaminated data cube, apply a rolling filter with the same filter sets used in Section 3.3.2, and measure one-point statistics of the resulting foreground avoided outputs.

As the data now contains simulated thermal noise, simply measuring moments

and deriving variance, skewness and kurtosis with Equation 1.3 to 1.6 will result in noise biases. To recover the "true" values of the statistics, unbiased estimators of the moments must be used. We derived the unbiased estimators for 2nd to 4th orders of the moments in Appendix A as part of the derivation of the analytical thermal uncertainty that we used in Chapter 2 analysis. They are,

$$\widehat{m}_2 = m_2^B - \sigma_n^2 \qquad \approx m_2^T, \tag{3.10}$$

$$\widehat{m}_3 = m_3^B \qquad \approx m_3^T, \tag{3.11}$$

$$\widehat{m}_4 = m_4^B - 6m_2^T\sigma_n^2 - 3\sigma_n^4 \qquad \approx m_4^T, \tag{3.12}$$

where we have denote the true, thermal noise biased and unbiased quantities with a superscript T, a superscript B and a wedge $\wedge$ symbol respectively for clarity. Notice that the 3rd moment is not biased by thermal noise, and the noise variance must be known to obtain the unbiased 2nd moment (i.e., the unbiased variance), which is needed to approximate the the true 2nd moment in the second term of the unbiased 3rd moment formula. To obtain the noise variance, we apply the same set of filters to the noise cubes and measure the variance of the output. Then, we use the measured noise variance to calculate unbiased moments with Equation 3.10 to 3.12 above and derive variance, skewness and kurtosis using Equation 1.4 to 1.6 as before. In actual observation, the noise variance can be computed by subtracting two subsequent integrations since the foreground and the 21 cm signal can be assumed to not change.

The process above is repeated for all combination of signal and noise cubes. Then, the average and the standard deviation of the measurements from the same signal cube and filter parameters are calculated over the 500 realization of noise to use as the expectation of values and uncertainties of the measured statistics. We also experiment with frequency binning over a broad range of frequency bandwidths from 1 to 8 MHz to improve thermal uncertainty (see Section 2.6 for discussion on the method).

First, we will omit the variance results from the figures because we find that thermal noise has little effects on the variance, yielding measured statistics that has little changes from the results Figure 19 and error bars that are smaller than the width of the lines for all filters. This is a good news as it suggest that HERA should have no problem detecting the variance.

The results for skewness and kurtosis with 2-MHz frequency binning are shown in Figure 22 and 23, where we have plotted the derived expectation values as dark gray lines and the uncertainties as light gray shades. We also re-plot measurements from the un-filtered and filtered signals as in Figure 20 and 21 for comparison.

As appearance in the figures, only the three cases with $\beta = 0$ and the $\beta = 1$ and $\theta = 5$ case are viable. For all other cases, thermal uncertainties dominate the signal to the point that the 500 noise realization that we use are not enough to estimate the expectation values. This may also be in part due to the actual skewness and kurtosis values being fluctuated around zero, resulting large variations in the estimate of the expectation values.

To check the effect of the wedge filter on the noise itself, we re-apply the filters on just the noise cubes (no signal) and measure variance, skewness and kurtosis of the noise cubes. Before filtering, variance of the noise cubes should be the square of the noise RMS, while skewness and kurtosis should fluctuate near zero as the noise are Gaussian. With the foreground avoidance filters applied, all three statistics of the noise appear to have little changes – there are only small differences in the low-level random fluctuations in noise statistics but no changes in the amplitude of the noise variance, skewness and kurtosis. This suggest that the foreground avoidance filter have no effect on Gaussian noise. Therefore, when more aggressive filter parameters

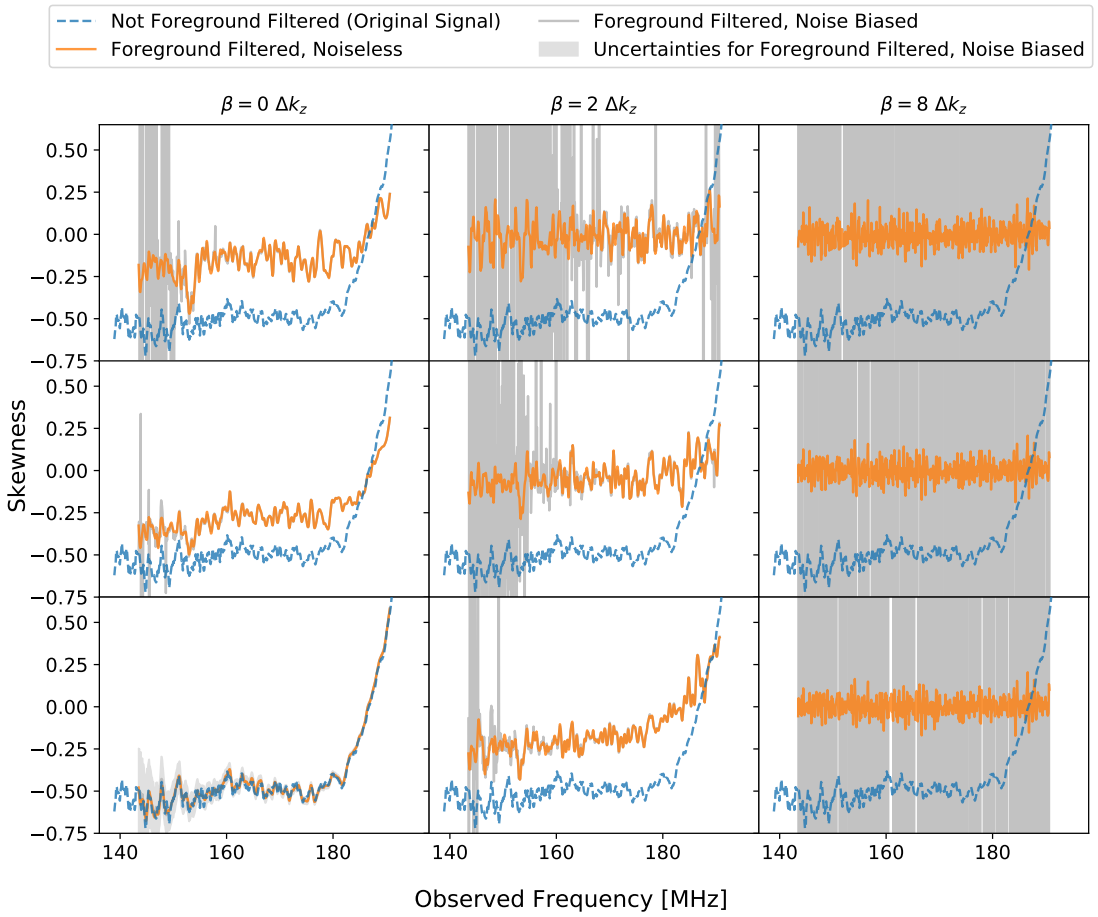

Figure 22. Drift scan skewness expectation values (solid dark gray lines) and uncertainties (light gray shade) derived from noise biased, foreground filtered, Monte Carlo simulations of the HERA350 Core instrument. Measurements from the noiseless simulations in Figure 20 and from the mock observation with no foreground filter are plotted for comparison as solid orange lines and dashed blue lines, respectively. Different panels correspond to measurements from the simulations with different foreground filtering parameters, which are described in the main text and in the caption of Figure 19. The simulations do not converged when aggressive filtering parameters are used, suggesting that foreground avoidance filtering removes signal but has little effect on the noise. Overall, these results suggest that minimal filtering must be used to be able to recover the statistics.

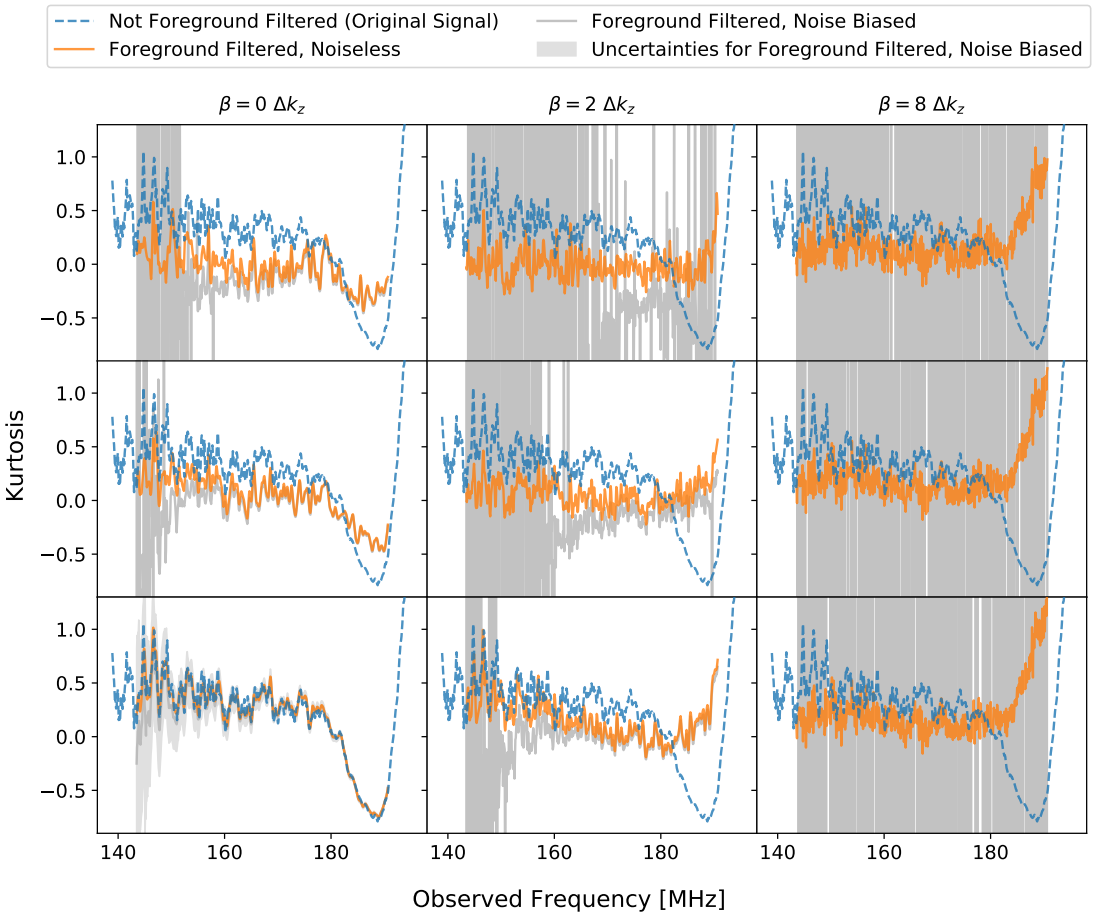

Figure 23. Drift scan kurtosis expectation values (solid dark gray lines) and uncertainties (light gray shade) derived from noise biased, foreground filtered, Monte Carlo simulations of the HERA350 Core instrument. Measurements from the noiseless simulations in Figure 20 and from the mock observation with no foreground filter are plotted for comparison as solid orange lines and dashed blue lines, respectively. Different panels correspond to measurements from the simulations with different foreground filtering parameters, which are described in the main text and in the caption of Figure 19. The simulations do not converged when aggressive filtering parameters are used, suggesting that foreground avoidance filtering removes signal but has little effect on the noise. Overall, these results suggest that minimal filtering must be used to be able to recover the statistics.

are used, only signals are removed but not noise, decreasing signal-to-noise ration and resulting measured statistics that are noise dominated.

3.4.1 Alternative Skewness and Kurtosis Measurements

We notice that when the thermal noise is dominating, averaging over 500 noise realizations does not converge skewness or kurtosis measurements to the expectation values that follow the trends of the statistics but results in overflows at the measured frequencies. The measurements would also not improve when we add several more noise realizations. This suggests that something in the skewness and kurtosis calculation causes the measurements to overflow.

Upon inspecting the the unbiased moment measurements from several pairs of signal and noise cubes, we found that left over fluctuations from the non-perfectly subtracted thermal noise, coupled with near-zero values of the moments in the frequency ranges where thermal noise is strong, result in the overflows in measured statistics that cannot be averaged out when deriving drift scan equivalent of the measurements. Since it is the division operation when deriving skewness and kurtosis from the moments that are causing the overflows, improving the uncertainty in the denominator before we perform the division should yield better expectation values.

We experiment with an alternative way to derive drift scan measurements by first averaging the moment measurements over multiple noise realization to obtain the drift scan measurements of the moments, and then calculate the drift scan skewness or kurtosis from the drift scan moments. These alternative measurements are demonstrated in Figure 24 and Figure 25 for skewness and kurtosis, respectively. To produce these two figures, we apply rolling foreground avoidance filters with $\theta = 90$ and $\beta = 2\ \Delta k_z$

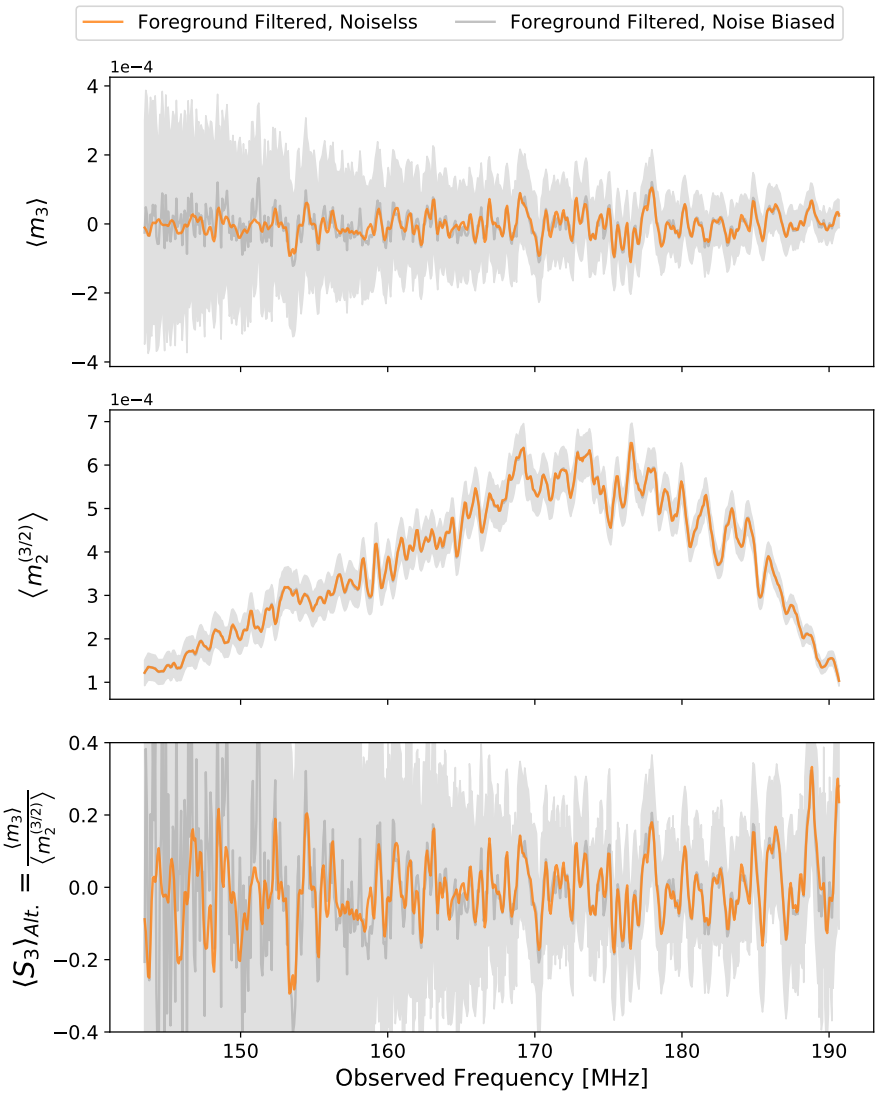

Figure 24. Illustrating an alternative way to measure drift scan skewness. The dark solid gray lines and the light gray shades in the top and middle panels are expectation values and uncertainties of the nominator and denominator terms in the skewness equation (Equation 1.5), derived from noise biased, foreground filtered ($\theta = 90$ and $\beta = 2$), simulations. The dark solid gray line in the bottom panel is skewness expectation value that is obtained by dividing the top panel with the middle panel. Similarly, the light gray shade in the bottom panel is skewness uncertainty propagated from the top and middle panels. The solid orange lines in all panels show measurements taken from noiseless, foreground filtered, simulations in Figure 20 for comparison. Notice how drift scan skewness calculated this way suffer significantly less overflows in high thermal noise regions in comparison to the drift scan skewness derived using our regular method (see Figure 22).

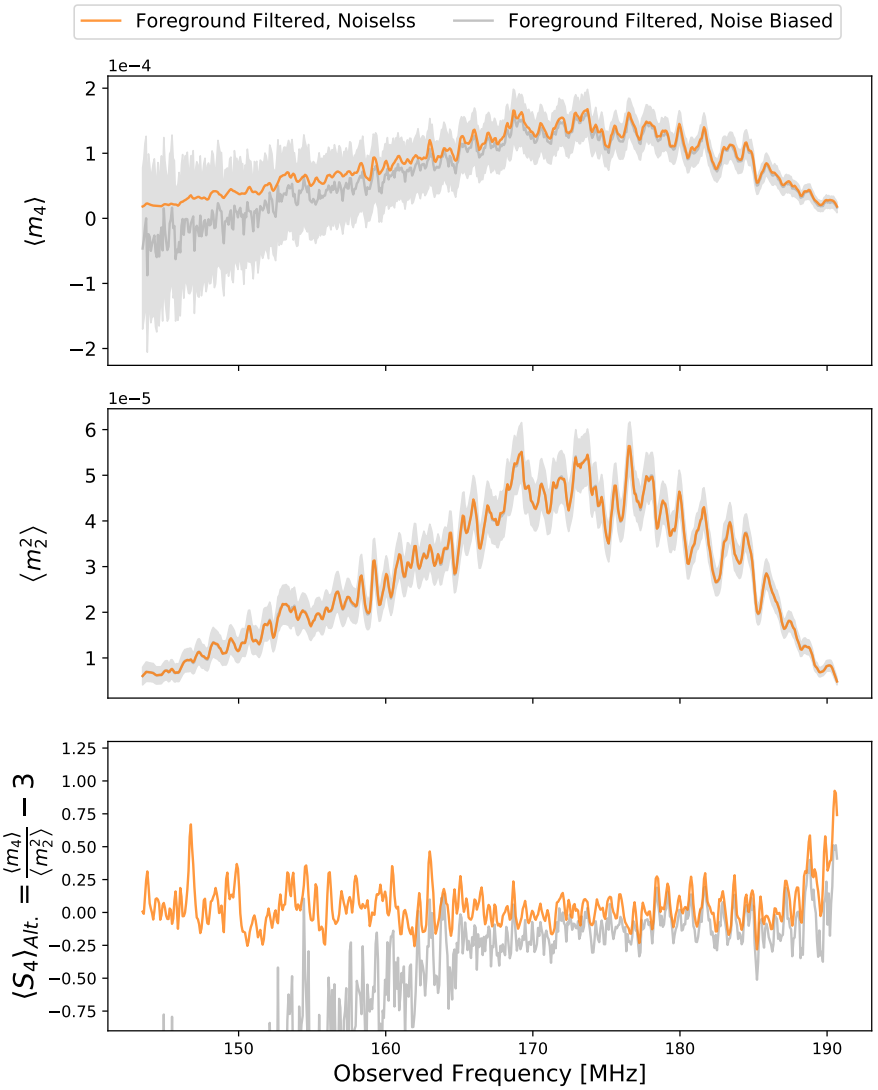

Figure 25. Illustrating an alternative way to measure drift scan kurtosis from foreground filtered data with $\theta = 90$ and $\beta = 2$ filter applied. All styling and colorization are the same as in Figure 24. Similar to the previous figure, kurtosis derived using this alternative method suffer significantly less overflows in high thermal noise regions (see Figure 23 for comparison).

to the same data set used to derive measurements in Figure 22 and 23. The top and middle panels show the derived drift scan moments as appear in the nominator and denominator terms for the corresponding statistics. The bottom panels show the drift scan skewness (or kurtosis) calculated by dividing the top panel with the middle panel. Error bars are propagated according to the standard uncertainty propagation. The solid orange lines in all panels show drift scan measurements derived using our regular method for a comparison. Notice how drift scan skewness and kurtosis calculated this way suffer significantly less overflows in high thermal noise regions. In the absence of noise, this alternative method will produce the same results as the method that we have been using. In the presence of noise, however, the latter will introduce additional bias. While derivation of this bias is beyond the scope of this work, but we include this discussion to demonstrate the possibility of improving the measurements.

3.5 Summary

In this Chapter, we study the effects of the foreground avoidance filters on 21 cm one-point statistics. We construct foreground avoidance filters that remove foreground contaminated modes from the spectrum of the data based on our knowledge of the instrument mode-mixing foreground wedge and the spectral leakage from the Fourier transform window function. We develop a rolling implementation of the filters that removes frequency-dependency filter bias from outputs. We experiment with different filter parameters and find that the filter bandwidths between 4 to 8 MHz are optimal. Applying an 8-MHz rolling filter to the 21 cm signal cube with multiple noise realization and performing Monte Carlo simulation, we found that the filter seem to have little effect on the noise but results in washed out statistics when more signals

are removed through the more aggressive filter. This suggests that we must find ways to reduce spectral leakage from the window function or remove contamination from foreground sources near horizon, or both, so that the less aggressive filter can be used.

Chapter 4

MEASUREMENTS FROM THE MURCHISON WIDEFIELD ARRAY PHASE I

In this chapter, we will apply some of the techniques that we have developed in the last two chapters to a real data set from the first season observations of the MWA. This data set is the same data set used in the analysis by Beardsley et al. (2016) that resulted in upper limits on the EoR power spectrum. The data is thermal noise dominated. Therefore, we do not expected detect the EoR using one-point statistics, but, through the analysis of the data, we hope to reaffirm our understanding of the statistics and demonstrate the techniques on real data.

Before we begin looking at real data, we will perform additional mock observation to derive the expected sensitivity of the MWA to one-point statistics using the same method that we have used in Chapter 2 to study the sensitivity of HERA to the statistics. In addition, we will use a high-precision radio interferometric simulator and the actual imaging pipeline of the MWA to simulate an even more realistic mock observation that includes chromaticity and sidelobe responses of the telescope point-spread-function (PSF). Output from this simulation will allow us to study if the sidelobe responses would affect the measured one-point statistics.

4.1 The Murchison Widefield Array

Since we will be focusing on the MWA in this chapter, we provide additional details on the telescope.

The MWA is a radio interferometer built in the Western Australian outback with

the primary science goal of detecting the EoR power spectrum. While primarily an EoR instrument, the array also serves as a general observatory for several science programs, including Galactic and extragalactic surveys, time domain astrophysics, solar astrophysics, and ionospheric science. The technical design of the array is detailed in Tingay et al. (2013), and the science capabilities are described in Bowman et al. (2013).

The collecting elements of the MWA – referred to as "antenna tiles" – comprise 16 dual polarization bow-tie shaped dipole antennas placed on a rectangular grid on top of a 5 m x 5 m ground screen with 1.1 m spacing between each antenna. Each dipole is sensitive to the entire sky and is optimized to operate in the frequency range of 80 - 300 MHz. The radio signals from the dipoles in each antenna tile are combined in an analog beamformer that generates physical delays to shift the phase of the signals and "point" the tile to different regions of the sky. The pointing of the tile generate a primary beam response that extends across the whole sky but with a usable main lobe of about 25 degrees diameter at 150 MHz, which define usable field of view of array. The MWA contains 128 such tiles placed in a pseudorandom arrangement with a tightly packed 50 m radius core and the remainder tiles extended to the radius of 1.5 km to provide capabilities for all science programs. EoR observations only use the compact core to optimize power spectrum sensitivity, foreground subtraction and calibration (Bowman et al., 2009; Beardsley et al., 2013).

The MWA had recently been upgraded to the Phase II configuration (hearafter MWA-II; Wayth et al., 2018). The MWA-II combines the original 128 antenna tiles of the MWA with 72 new tiles on two compact hexagons near the original core for optimal power spectrum analysis and 56 new tiles on extended baselines up to 5 km for improved survey and imaging capabilities. In this chapter, we will only focus on the original Phase I configuration.

4.2 Detectability

Now we explore the detectability of the MWA to one-point statistics. We perform a simulation of the MWA observations following the same procedure that we have used to simulate HERA observations in Chapter 2. As before, we smooth the input 21 cm intensity cube representing the sky with a Gaussian kernel with a FWHM matching the angular resolution of the telescope to approximate the instrument beam response. We measure one-point statistics from the instrumentally corrupted signal cubes and calculate uncertainty from thermal noise using an analytical method discussed in Appendix A. The statistics and uncertainties are calculated using the native 80-kHz frequency resolution. We ignore foreground contamination and perform the simulation on a single field of view, neglecting drift scan effect. We also include HERA37 and HERA350 Core simulations for comparison. The former happens to match the angular resolution of the MWA Phase I Core, allowing for a relatively direct comparison of the two, although the MWA has a much wider field of view. Table 2 summarizes our simulation parameters for the MWA Phase I Core and both HERA configurations. Results from this simulation are shown in Figure 26.

First, it is evidence that the MWA Phase I will not have sufficient thermal sensitivity to detect any of the statistics with the native frequency channel resolution. Although frequency binning can improve thermal noise, the actual MWA frequency bandpass are separated into several coarse bands of 1.28 MHz bandwidth (Prabu et al., 2015) with small gaps of reduced sensitivity in between neighboring channels, making it difficult to bin the data over multiple coarse bands. Beside, our simulation here assume 1000 hours of integration, whereas data from Beardsley et al. (2016) are from 32 hours of integration and will thus have approximately 5 times more thermal noise. An N-MHz

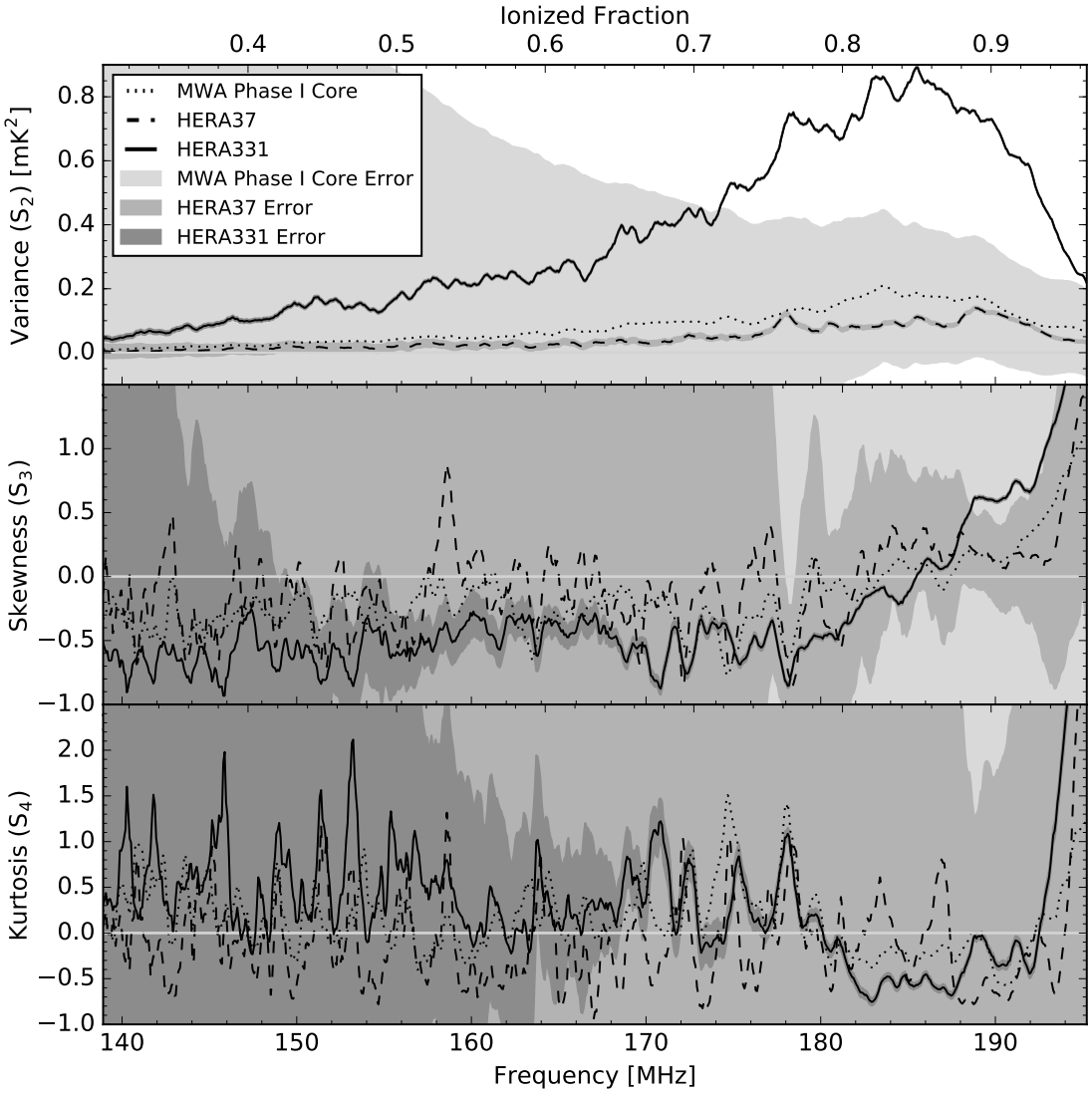

Figure 26. Sensitivity of the MWA to one-point statistics. The variance skewness and kurtosis with estimated uncertainty from thermal noise are shown in the top, middle, and bottom panels. The dotted, dashed and solid lines show statistics derived from MWA Phase I Core, HERA37 and HERA331 simulations using Gaussian kernels to approximate the telescope PSFs. The shaded regions are estimated thermal noise uncertainty, starting from lighter to darker from MWA Phase I Core to HERA. Note that the uncertainty for HERA331 is not visible in the variance plot and only becomes prominent in skewness and kurtosis below 170 MHz. All simulations here are performed with 80kHz frequency channels.

Simulation Parameters	MWA Phase I Core	HERA37	HERA 350 Core
Number of Collecting Element	50	37	331
Antenna Area (m^2)	21.5	153.86	153.86
Collecting Area (m^2)	1075	5,696	50,953
Maximum Baseline (m)	100	98	140
Integration Time (h)	1000	100	100
Angular Resolution (deg)	∼1-1.6	∼1-1.6	∼0.3-0.5
Field of View (deg)	∼20-35	∼7-11	∼7-11

Table 2. Instrument specifications used in our simulations. In addition to the parameters above, antenna layouts were taken from Beardsley et al. (2012) and (DeBoer et al., 2017). For all of our simulations, we use a simulation bandwidth of ∼139-195 MHz with 80 kHz raw spectral channel width.

binning will also only reduce the thermal noise by approximately $\sqrt{N}$. Thus, we do not expect frequency binning of reasonable bin sizes to improve the data.

As for the measured statistics, the higher angular resolution of HERA350 Core, compared to HERA37 and the MWA Phase I Core, smooths out less signal, especially early in reionization when feature sizes are smaller. This results in an overall higher observed variance. Similarly, skewness and kurtosis derived from the HERA350 Core simulation show more fluctuation, especially earlier in reionization, as the telescope's smaller PSF resolution is more sensitivity to small ionized and overdense structure that contribute to the skewness and kurtosis. Regardless, the overall trend of skewness and kurtosis are the same for all telescopes as these two statistics are sensitive to the relative amplitude of the fluctuations, which is not affected by PSF smoothing.

Nevertheless, given less sensitivity of the array and less number of integration, we do not expect to see any EoR features in the one-point statistics that we will measure from Beardsley et al. (2016) data.

4.3 Sidelobe Effects

The main instrumental response of a radio interferometer is the array PSF response, which is both directional and spectral dependent and consists of the dominant main lobe and spatially varying sidelobes. The functional shape of the PSF depends on the primary beam response of the individual collecting element, the layout arrangement of all collecting elements, the observing frequency, and the pointing direction. The FWHM of the main lobe of the PSF is approximately equivalent to the angular resolution of the array. Up to now, we have been using this fact to approximate the telescope's PSF with a Gaussian function. Specifically, we have been using a Gaussian kernel with a FWHM matching the angular resolution of the array to smooth a sky model to produce observed intensity maps.

Figure 27 compare the true PSF of the MWA with the Gaussian approximation. The solid line shows a cross section of the PSF of the full MWA Phase I array that includes all 128 antenna tiles. The dotted line shows the PSF of the array's compact core that includes tiles within the 100 meter diameter, which is the PSF used in EoR analysis. The solid-line with square markers shows a Gaussian fit to the main lobe of the compact core PSF that we used to simulate mock observation in the previous section.

The Gaussian beam approximation is common in analytical studies in literature. Since most of the power of a PSF resides in its main lobe response, a Gaussian fit to the main lobe offer a solid approximation to the PSF. However, the Gaussian fit neglects spatial variation in the sidelobe response directional dependency in the PSF that could add low-level structures known as sidelobe confusions to the observed

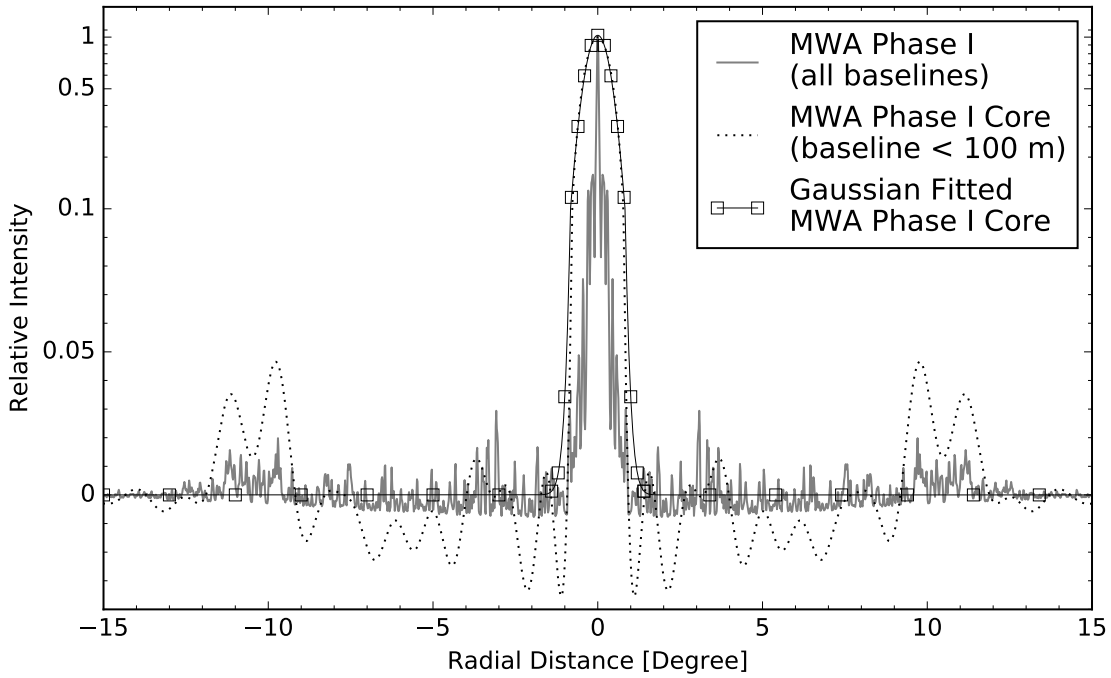

Figure 27. Cross sections of the beam responses of the full MWA Phase I with all baselines (solid line), and the MWA Phase I Core with only baselines less than 100 meters (dotted line). A Gaussian fit to the latter case is shown as solid line with squares. Note that scaling on the y-axis is linear from -0.05 to 0.1 and logarithmic otherwise.

maps. Since, skewness and kurtosis are very sensitive to spatial structures, we will want to know if the MWA sidelobe responses would have any effects on our analysis.

To investigate, we carry out an end-to-end high-precision simulation of the MWA Phase I Core observation using the MIT Array Performance Simulator (MAPS[7]) and the Fast Holographic Deconvolution (Sullivan et al., 2012, FHD;), one of the two primary calibration and imaging pipelines of the MWA (Jacobs et al., 2016). MAPS generates directional and frequency-dependent PSF response from user-configurable antenna configurations, array configurations and observing parameters, and performs

[7]https://www.haystack.mit.edu/ast/arrays/maps/

a convolution of the PSF with a sky model. MAPS also applies w-projection to correct for widefield effects. We configure MAPS to use the MWA Phase I 128-tile array layout, using a short cross-dipole on an infinite ground plane as an antenna model. We run MAPS on our full-sky 21 cm lightcone models, performing the simulations independently for each observing frequency with the corresponding input map to ensure spectral dependency in the simulation. In real EoR observation, the MWA operate in a drift-and-shift mode. The telescope is pointed at a specific coordinate in a radio quiet region of the sky (for example, $\alpha = 0$h, $\delta = -30°$) and observes as the sky drifts throughs the primary beam. Then the telescope is repointed, and the process repeats. Although MAPS is capable of simulating such a complicated observation, we adopt a simpler single-point observation where the telescope is always pointed at the zenith for our simulation, and model the limiting case of a single snapshot image with 2 second integration to avoid complication from sky rotation. Our results, therefore, correspond to the worst-case PSF with no rotation synthesis to improve UV coverage and sensitivity of the measurements.

The outputs from MAPS are amplitude and phase values of the visibility for each baseline pair that can be observed by the array. To form an image, the visibility must be re-gridded into a rectangular coordinate in the instrument baseline space and Fourier transform. We use FHD to perform these two steps, dropping the visibility from baseline greater than 100 m to only form an image with the MWA Phase I Core. The re-gridding step is equivalent to reconstructing the Fourier transform of the sky brightness that have been sampled by the PSF at each baseline pair coordinate to produce the visibility during the observation. The PSF response must be precisely known to ensure accurate reconstruct the original sky. FHD contains an empirical beam model of the MWA that it uses during the re-gridding. The gridded visibility can be immediately

Fourier transform to produce a "dirty" map of the sky brightness or deconvolved to remove the structures of the PSF. In principle, a deconvolution through a matrix inversion or an iterative algorithm such as the CLEAN algorithm can be utilized to remove the PSF structure and recover the "true" sky brightness. However, the sky structures in maps from reionization arrays are too complicated and not sufficiently sparse to utilize such an approach. For current EoR experiments, foreground-subtracted dirty images are generally where derived statistics are calculated. As such, the dirty maps will be the final data products of our simulation.

The bottom row of Figure 28 compare the dirty map derived from the MAPS–FHD MWA simulation to an output map from the Gaussian beam simulation and the difference between the two, as well as the input sky model used in both simulations for reference. The PDFs for the four maps are also plotted in the top panel. All data shown correspond to $x_i = 0.5$ ($z = 7.9$, $\nu = 158.195$ MHz). Two effects are readily apparent. First, The MAPS-FHD simulated map has higher dynamic range than the Gaussian simulated map. This is likely cause by the more accurate PSF used in the MAPS-FHD simulation. Second, the differences between the outputs of the two simulation methods lies mostly outside of the primary beam FWH, indicated as a black circle in the figure. This effect is caused by how FHD directionally weights the primary beam to produce a flat field from a curve sky and is thus more faithful to real observation.

One take away point from the second effect is that, if only data within the primary beam FWHM is used, Gaussian simulated maps should give similar one-point statistics measurements to the more accurate MAPS-FHD simulated maps. Figure 29 illustrate this point. The variance, skewness and kurtosis derived from the MAPS-FHD (solid line) and Gaussian (dashed line) simulations, as well as statistics derived from the dif-

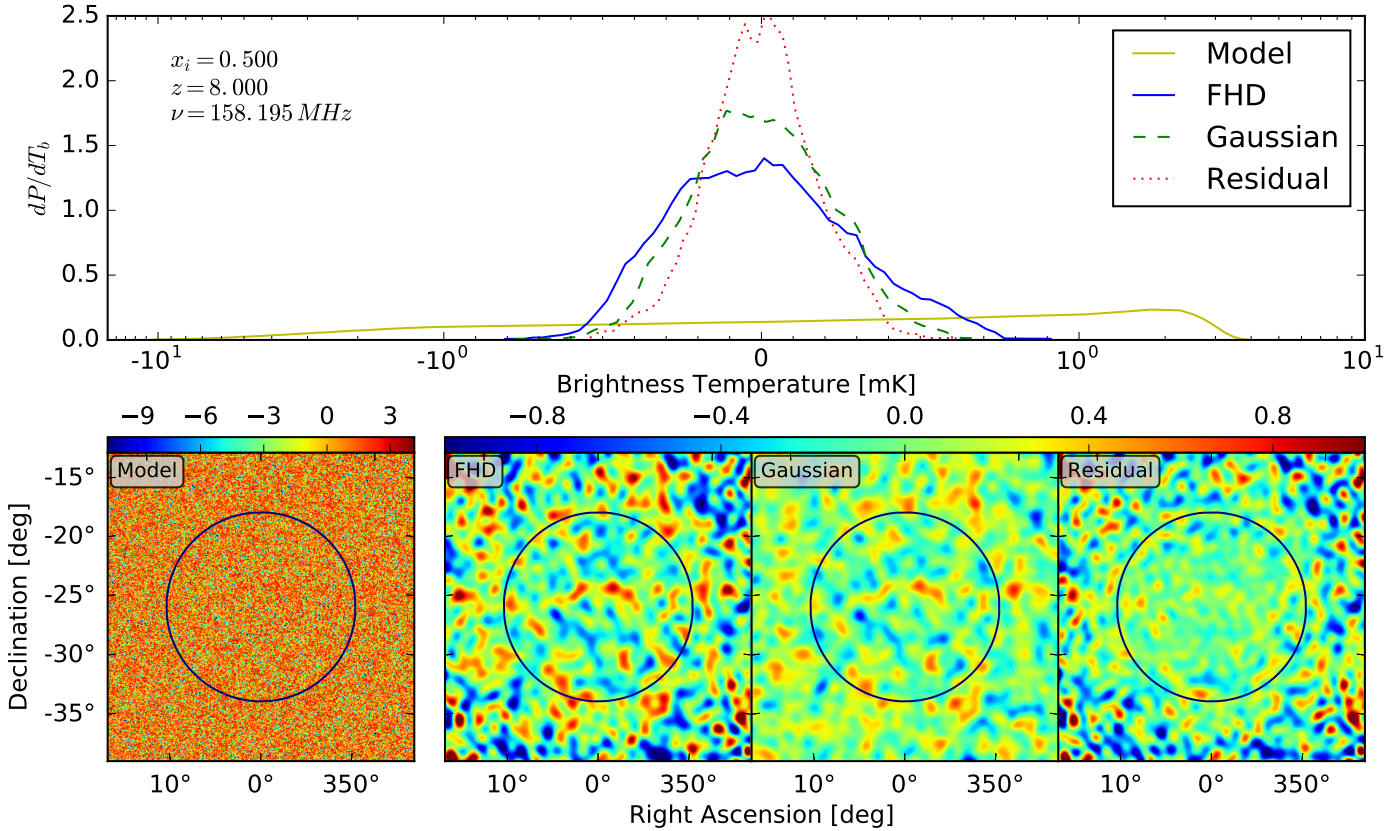

Figure 28. Example PDFs (upper panel) derived from the FHD (solid line) and Gaussian (dashed line) simulations at $x_i = 0.5$ ($z = 7.9$) along with the corresponding simulated maps (lower panels). The PDF of the residual map between the two simulations (FHD - Gaussian) is also shown as the dotted line along with the map. Black circles in the maps indicate the field of view of the telescope, equivalent to the FWHM of the primary antenna beam. Notice that the different between the two simulations are mostly contained outside of the field of view FWHM. Therefore, we only use the pixels inside the field of view are used to calculate statistics.

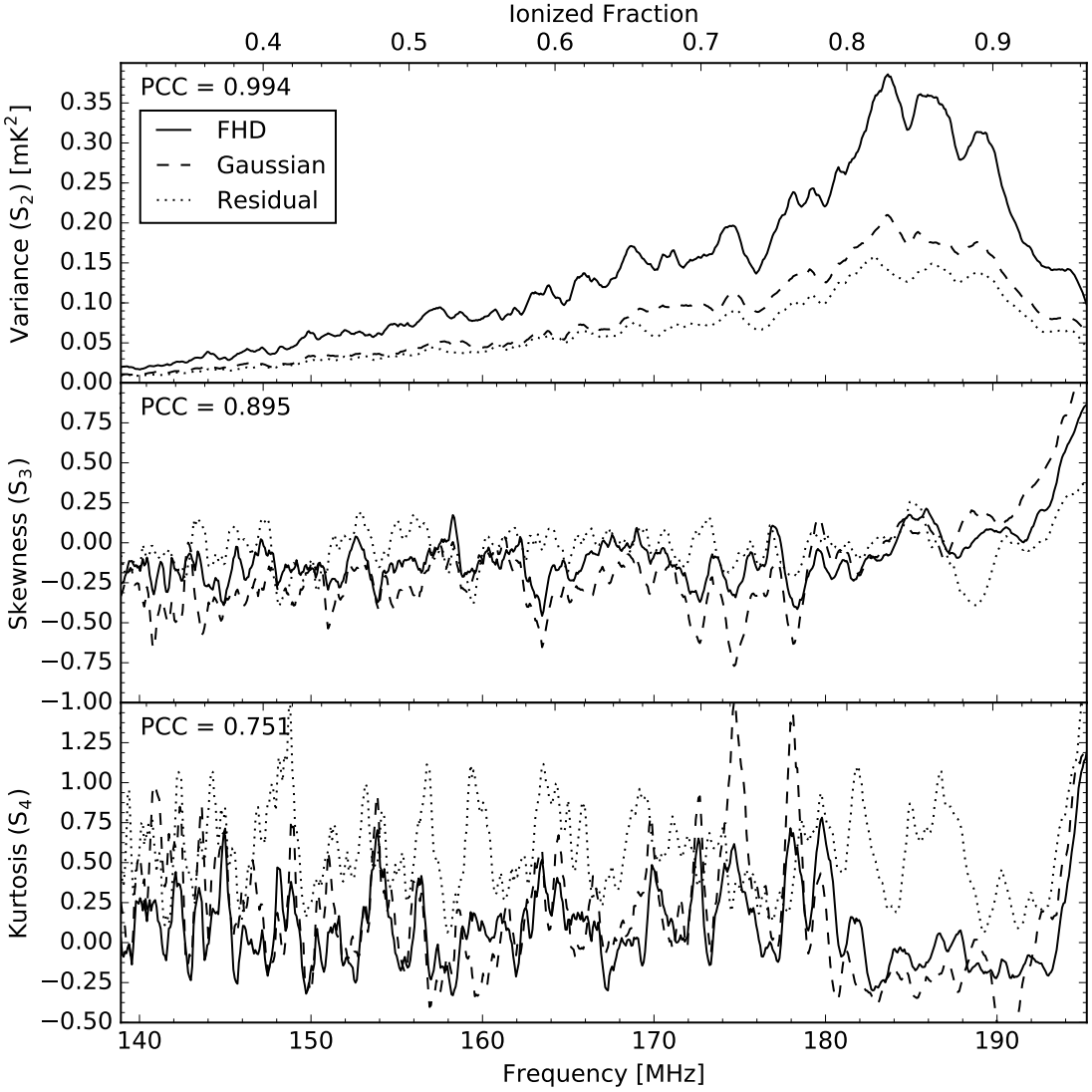

Figure 29. Variance (top), skewness (middle) and kurtosis (bottom) derived from the FHD (solid lines) and Gaussian (dash lines) simulations as a function of frequency and ionized fraction. Statistics for the residuals of the two simulations are also shown as dotted lines. PCC is the Pearson correlation coefficient between statistics derived from FHD and Gaussian simulations.

ferences between the two simulations, are plotted as a function of ionization fraction and frequency. The statistics presented here exhibit stronger fluctuations throughout the measured frequency, as opposed to smoothly varying measurements shown in Chapter 2 and 3, due to the sample variance inherent in simulating an observation of a single field, rather than averaging over measurements from multiple field.

Despite, it is evident that the one-point statistics resulting from the FHD-simulated maps and Gaussian-smoothed maps are qualitatively similar. Skewness and kurtosis derived from both methods of simulation are almost exactly matched, neglecting slight detailed variation. However, the FHD-derived variance is consistently higher than the Gaussian-derived variance by approximately 56%, which is a result from a broader PDF (see Figure 28). We interpret the increased variance in the FHD case to be due to the complicated sidelobe structure inherent in the full instrumental PSF. This structure results in sidelobe confusions that scatters power throughout the map, raising the overall variance. Sidelobe confusions are also the likely cause of the differences in the small detailed fluctuations in the skewness and kurtosis measured from the two simulations. Despite the discrepancy in variance between the two cases, the dependence on ionization fraction of each of the statistics is highly correlated between the two cases. We quantify the similarity by calculating the Pearson Correlation Coefficients (PCC) between the two cases for each one-point statistic. We find coefficients of 0.994 for variance, 0.895 for skewness, and 0.751 for kurtosis.

We attempt to further quantify the effect of sidelobe confusion by measuring statistics from the residual maps derived by subtracting FHD maps from Gaussian maps. The residual maps contain features from sidelobe confusions and other effects inherent in the full instrumental PSFs. Statistics derived from the residual maps are plotted in Figure 29 as dotted lines along with those from the FHD and Gaussian

simulated maps. Variance of the residual maps closely follow variance from the Gaussian convolved maps as expected from the fact that the FHD-derive variance is 56% higher than the Gaussian-derive variance. The residual skewness and kurtosis remains noise-like through the redshifts, oscillating around -0.029 mean and 0.136 standard deviation for skewness and 0.576 mean and 0.282 standard deviation for kurtosis.

Based on these findings, we conclude that Gaussian-smoothing kernels are reasonable approximations to full instrument simulations for densely-packed antenna arrays such as the MWA Phase I Core. The skewness and kurtosis estimates derived from Gaussian smoothed maps are likely sufficient for many statistical investigations. For variance estimates, a simple transfer function of the form $m_2^{obs} = f(m_2^{Gaus})$ can be used to compensate for the factional difference between the estimates derived from realistic simulations and more-commonly modeled idealized cases. Inspection of Figure 29 suggests that this function may reduce to a multiplicative correction factor such that $m_2^{obs} = f_0 m_2^{Gaus}$, with $f_0 = 1.56$ in our case. We have not explored different 21 cm input models, but given that most theoretical models yield similar features, we expect the correction factor to be generally independent of the detailed properties of the 21 cm signal for a given instrument.

4.4 Measurement from The MWA First Season Data

Now that we have developed a good expectation on the sensitivity and the PSF response of the MWA, it is time to look at data from the MWA observations.

The data set that we will be looking at is the same data set used in Beardsley et al. (2016). It is fully calibrated and foreground subtracted through an iterative foreground modeling approach based on the FHD software package and a hierarchical source

catalog. The data set contains several data cubes representing different components of the sky, including the dirty sky brightness (which, roughly speaking, includes 21 cm signal, foreground signal, and noise), the FHD foreground models, and their differences (residual), as well as other quantities for power spectrum formation. Each frequency and polarization (XX or YY) of a data cube is stored as a HEALPix map with NSIDE=1024, providing $\sim 3.4''$ pixel resolution that sufficiently oversample the ~ 1 degree PSF resolution of the array. The data was collected using the MWA Phase I Core array with 32 hours of integration on the "EoR0" observing field (Right Ascension (RA) = 0h00, Declination (Dec) = -27°). The frequency bandwidth is 30.72 MHz, consisting of 24 of the 1.28-MHz coarse band that span the frequency range from ~ 167 MHz to ~ 197 MHz. The frequency resolution is 160 kHz.

Figure 30 show slices of the dirty, model and residual cubes at 180 MHz. The color scales of all panels are the same arbitrary unit. This unit is used internally by FHD, so that it can pass the data directly to the CHIPS power spectrum estimator (Trott et al., 2016), which is part of the pipeline in (Beardsley et al., 2016). Thus, we keep the unit as it is. Skewness and kurtosis are unitless and can thus be measured regardless of the unit. Variance will be affected by the unit, but we will still be able to see below that it is dominated by noise. As expected, the FHD foreground model is far from perfect. We can see that some regions in the image are over-subtracted and under-subtracted. This subtraction errors will have significantly impact on the skewness and kurtosis as we will see below.

In principle, foreground avoidance filters, which we explored in details in the previous chapter, can be applied to the dirty data cube to remove foreground contaminated data before measurements. However, additional simulation will be needed to study how the coarse band of the MWA bandpass will interact with the foreground

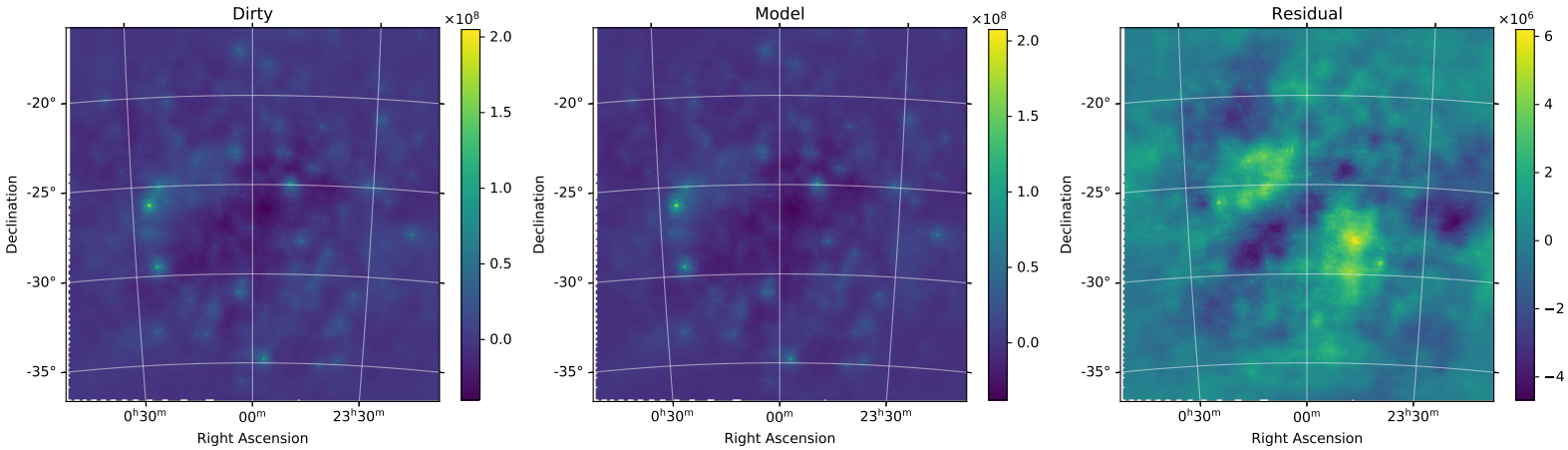

Figure 30. Maps of the dirty (left), foreground model (middle) and the residual between the two (right) from the first season data of the MWA at 180 MHz (Beardsley et al., 2016). The color scales are arbitrary units. Bright source-like structure and void in the residual are remnants of un-subtracted and over-subtracted foregrounds.

avoidance filter. Therefore, we do not apply the foreground avoidance technique in the this data set, postponing the investigation to future works.

We are mostly interested in measuring one-point statistics from the residual is an estimate of a sum of the 21 cm signal and noise. We estimate one-point statistics of the 21 cm from the data using the unbiased estimators that we derived in Appendix A, but we need to know the noise variance to use the unbiased estimators.

The noise variance can be estimated from the difference between the even and odd data sets with some assumptions on the noise. We will derive how this can be done in the next few paragraphs.

First, let's assume that the each of the even (I_{even}) and odd (I_{odd}) maps for each polarization and frequency contains signal (I_{sky}), which can either be 21 cm signal or foreground or both, and noise (n). Let's also assume that the signal in the odd map is the same as the signal in the even map. This is the same assumption use when deriving an unbiased estimator of the power spectrum. With this assumption we have,

$$I_{even} = I_{sky} + n_i, \tag{4.1}$$

$$I_{odd} = I_{sky} + n_j, \tag{4.2}$$

where we have use the subscript i, j to differentiate the two set of noise in the even and the odd maps.

We can subtract the odd map from the even map to obtain their difference (I_{dif}) that only contain the two noise,

$$I_{dif} = I_{even} - I_{odd} \tag{4.3}$$

$$= (I_{sky} + n_i) - (I_{sky} + n_j) \tag{4.4}$$

$$= n_i - n_j. \tag{4.5}$$

We can then square the difference and average to get its variance,

$$\langle I_{dif}^2 \rangle = \langle (n_i - n_j)^2 \rangle \tag{4.6}$$

$$= \langle n_i^2 - 2n_i n_j + n_j^2 \rangle \tag{4.7}$$

$$= \langle n_i^2 \rangle - 2\langle n_i n_j \rangle + \langle n_j^2 \rangle. \tag{4.8}$$

If we assume that the noise in the even and the odd maps are not correlated, the middle term can be dropped to get,

$$\langle I_{dif}^2 \rangle = \langle n_i^2 \rangle + \langle n_j^2 \rangle. \tag{4.9}$$

Then, if we also assume that the two noise are drawn from the same distribution, which is a valid assumption as we observing the same sky with the same instrument, n_i and n_j can be added to obtain,

$$\langle I_{dif}^2 \rangle = 2\langle n^2 \rangle \tag{4.10}$$

The average of a square of a random variable quantity is its variance. This means that we can obtain the noise variance by calculating the variance of the difference between the even and the odd maps and divide the output by 2,

$$\sigma_n^2 = \frac{Variance(I_{even} - I_{odd})}{2}. \tag{4.11}$$

Now that we know how to obtain the noise variance, we can calculate the 2nd, 3rd and 4th moments from the unbiased estimators of the corresponding moments (Equation 3.10 – 3.12) and estimate variance, skewness and kurtosis from the unbiased moments using Equation 1.4 – 1.6 as before. Since the data cubes has already been cropped to a 21 degrees rectangular field of view, we perform the calculations directly on the HEALPix maps, using all pixels within the field. We also average the odd and

even cubes together first to improve the noise variance by a factor of 4 before calculating statistics. Therefore, we calculate the noise variance according to Equation 4.11 and the procedure that we have laid out above, but we divide the resulting values by 4 to adjust for improvement from averaging before using them in the unbiased moment calculations. We also form the Stoke I product by averaging over the two polarization, $I = (XX + YY)/2$ before any of the above calculation. Figure 31 shows the unbiased variance, skewness and kurtosis measured from the data sets along with the derived noise variance.

The most noticeable feature in these measurements is clearly the "picket fence" coarse bands of the MWA that show up in all statistics. Reduced sensitivity in the gaps between the course bands cause the noise variance and the data variance to sharply drop from the over all trends.

The derived noise variance follow a negative power law as expected as they should be dominated by the Galactic synchrotron radiation. The noise variance of the dirty and residual cubes are at similar levels, which is a good sign as both should contain similar level of noise.

The variance of the dirty sky and the foreground model are also at similar level as expected since the dirty sky should be dominated by foreground. However, the unbiased variance of the residual are still several order of magnitude higher than the noise variance despite having already taken into account the noise. This suggests that foreground subtraction and calibration errors dominate the measurements. It is also possible that the noise are highly correlated between pixels and between the even and odd time intervals and thus cannot be estimated using the method that we have developed.

Skewness and kurtosis of both the dirty cube and the foreground model are pos-

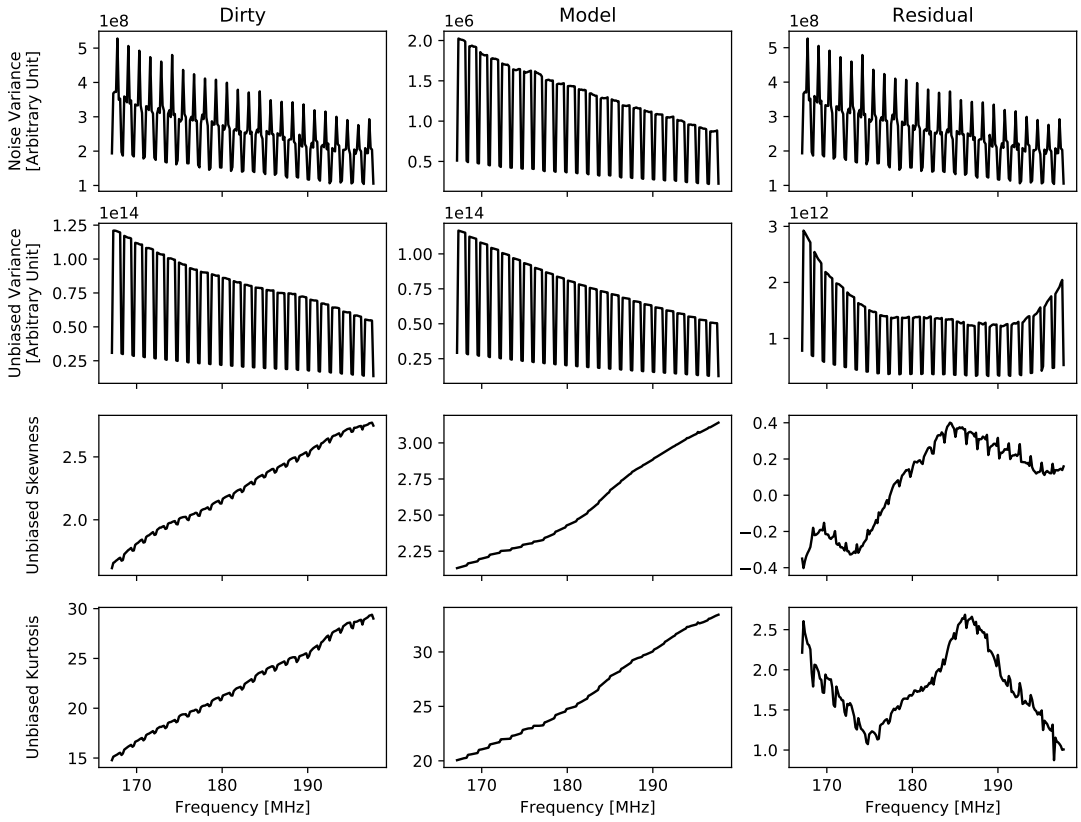

Figure 31. One-point statistics measured from Beardsley et al. (2016) data sets. The first row from the top show the estimates of the noise variance from Equation 4.11, which is needed to derived the unbiased variance, skewness and kurtosis in the 2nd, 3rd and 4th rows, respectively. Different columns, from the left to the right, show corresponding measurements from the dirty (observed), foreground model and residual (dirty - foreground model) data. The course bands of the MWA are visible as the "picket fence" variation in the variance. Foreground subtraction and calibration errors dominate these measurements, appearing as noise-like variance and variation in skewness and kurtosis. In addition, skewness and kurtosis of the dirty and model data sets, which are dominated by the foregrounds, suggest that foregrounds PDF is heavy-tailed. Understanding which foreground components are responsible for the tailness of the foreground PDF is an important question for future study of 21 cm one-point statistics.

itive and increase as frequency increases. Since both are dominated by foregrounds, this suggests that the foreground components that correspond to the tails of the foreground PDF are dominating and become relatively brighter than the other components as frequency increases. This is opposite to the sky-averaged foreground power, which decreases as frequency increases. One explanation may be that the foreground components that are responsible for the tails of its PDF have flatter spectral indexes than the other components. Understanding which astrophysical processes are responsible for these components is important for the measurements of higher-order 21 cm one-point statistics but will require significant efforts in modeling and analyzing foreground data. We therefore postpone the investigation to future works.

After the foreground has been subtracted from the dirty cube, the remaining residual exhibits non-zero skewness and kurtosis that gradually rise and then fall as frequency increases. This variation is cause by foreground subtraction errors. When the foreground is over-subtracted or under-subtracted, the residual will have high positive or negative intensity relative to the mean of the fluctuations. For example, The right panel in Figure 30 clearly show the bright foreground-like object that is caused by under-subtraction. These regions correspond to the tails of the PDF of the fluctuations and will thus have strong impact on skewness and kurtosis. In principle, the EoR is also contributing to these measurements, but the results here are highly dominated by foreground subtraction effects.

4.5 Summary

Over the course of the investigation in this chapter, we have transitioned from simple mock observations to end-to-end simulation of the radio interferometric ob-

servation and imaging, and to real data. With the simple mock observation that use a Gaussian function to approximate the instrument, we are able to obtain an estimate of sensitivity of the MWA to one-point statistics, which suggested that one-point statistics measurements with the MWA data will be dominated by thermal noise.

With the high-precision simulation, we were able to show that the Gaussian PSF kernels can reasonably approximate the full instrument simulations for arrays with densely-pack antenna configuration such as the MWA Core. Our results also show that high correlation is maintained between statistics derived from simulations with Gaussian and full PSFs although sidelobe confusion in the full PSF can scale the measured statistics by as much as 40-60%.

Looking at the real data, we come to a realization again that foreground contamination is the most challenging aspects of the EoR observations. Despite using a data set that has been carefully calibrated and foreground subtracted, we are unable to obtain sensible measurements due to errors in foreground subtraction. Nevertheless, we show through our discussion that we have relatively good understandings of the signal, our instruments, and the nature of one-point statistics.

Chapter 5

CONCLUSION

In the first chapter of this dissertation, we identified one important question regarding the measurement of one-point statistics of 21 cm brightness temperature intensity fluctuations. Following-up on theoretical leads in literature, we asked if one-point statistics can be measured in real observation under the influence of contamination from foreground sources and systematics.

To answer this question, we developed tools that simulate realistic mock 21 cm observations and used them to establish the baseline sensitivity of HERA to the statistics. We showed that HERA will have enough sensitivity to measure one-point statistics if foreground contamination can be sufficiently mitigated. We developed a foreground avoidance technique and showed that it can be used to obtain noise-limited measurements with HERA in the presence of foreground. Our results have demonstrated that one-point statistics can be used as a complementary probe to the EoR in upcoming observations, especially with HERA.

In addition to these findings, we have significantly contributed new development to the broader reionization and related fields. We are the first to look at how foreground avoidance measurements would affect the brightness temperature intensity fluctuations in real space, which led to an optimization of the foreground avoidance filter through the rolling implementation. We have also included kurtosis in the analysis of 21 cm fluctuations for the first time, deriving and contributing analytical expressions of its the unbiased estimator and thermal noise uncertainty to literature. We have also developed a tiling method that transform three-dimensional cosmological simulation

in the observed sky maps. All of these technique can potentially be used in future studies.

Nevertheless, there are several limitation in our work. First, we have only consider one reionization model partly due to the overhead of running large simulations. Over the course of this work, 21 cm simulation tools, such as (Mesinger et al., 2011), has become significantly mature and much easier to use, and we will be employing them in our future works. Second, we did not investigate the effects of the foreground subtractions on one-point statistics. Lastly, all simulation in our works, except the MAP-FHD simulation in Chapter 4, used Gaussian approximation to the synthesized beam response and did not take into account actual antenna layouts and the effects of rotation synthesis. The results that we presented in Chapter 2 and 3 are, therefore, the best case statistics. High-precision, end-to-end, radio interferometric simulations are required for more realistic studies but are computationally expensive. The landscape may change as better tools are currently being developed by a team of scientists that include members from both HERA and the MWA collaborations.

5.1 Future Directions

There are three primary challenges in pursuing future detection and characterization of the EoR with alternative statistics: (1) the sensitivity of the telescope to the statistics, (2) mitigation of astrophysical foreground contamination, and (3) inferring of reionization and astrophysical parameters from the measurements. Addressing these challenges for one-point statistics has always been the broader goal of this work. We extensively investigated the first challenge through the analysis of mock 21 cm observations. We partially addressed the second challenge through foreground avoid-

ance analysis. We believe that our accomplishment here is significant, but there are still many works left to be done as we have yet to address all challenges.

One possible follow-up to this dissertation is completing the investigation on the mitigation of astrophysical foreground contamination by studying the effects of foreground subtraction on one-point statistics. This may be done in several ways. The most direct approach would be to simulate mock 21 cm observations that include models for Galactic diffuse emission and extragalactic radio point sources, implement various foreground subtraction methods on the mock observations, and investigate their effects on the measured one-point statistics. Computational overhead will be the primary limiting factor for this approach as the full interferometric calculation and visibility gridding must be done to simulate the foreground wedge contamination. This is probably best done using a combination of simulation tools that are currently being developed by the EoR community, such as, e.g., FHD, PRISim[8], and pyuvsim[9]. Another possible, much more simple, approach is to implement foreground subtraction directly on the 21 cm brightness temperature fluctuations, with no foreground, using polynomial fitting methods and measure one-point statistics of the fitting residuals. This analysis can offer insights into the bias from the subtraction on the fluctuations and resulting one-point statistics, as well as the requirement for the accuracy of subtraction. The approach that will be the most beneficial to the EoR community is, of course, a comprehensive study that consists all of the above approaches.

Another possible follow-up is to address the remaining challenge on the inferring of reionization physics from one-point statistics measurements. This is perhaps the most important work left to be done as it is the least well-understood aspect of any

[8]https://github.com/nithyanandan/PRISim

[9]https://github.com/RadioAstronomySoftwareGroup/pyuvsim

alternative 21 cm statistics that is not the power spectrum. There are a few ways to obtain constraints on reionization and astrophysical parameters. Sensitivity analysis can be conducted on an ensemble of 21 cm models that span a wide parameter space. This approach is a direct extension from the method used in this work, but computational cost will quickly becomes expensive as the parameter space grows. A technique such as Markov Chain Monte Carlo (MCMC) utilized in 21CMMC software (Greig and Mesinger, 2018) uses Bayesian statistics to significantly speed up the process and provide full probability distribution of the parameter constraints. A new version of 21CMMC that is currently being developed plan to include capability to adopt any input signals and statistics beyond the EoR and the power spectrum. Hence, this analysis should become straightforward and feasible in the near future.

Over the past few years, theoretical landscape in alternative 21 cm statistics has also seen a significant change in the preferred choice of statistics toward the bispectrum, a three-point correlation function of the 21 cm visibility (see, e.g., Pillepich et al., 2007; Yoshiura et al., 2015; Muñoz et al., 2015; Shimabukuro et al., 2016; Watkinson et al., 2017; Shimabukuro et al., 2017; Majumdar et al., 2018; Schmit et al., 2018). The primary advantage of the bispectrum to one-point statistics is that the bispectrum can probe non-Gaussianity at all scales. Deriving bispectrum still requires the visibility to be gridded, and thus require an accurate model of the telescope response. The recent experiment with the closure-phase bispectrum (Carilli et al., 2018) is also interesting and does not required the visibility to be gridded. Other alternative statistics that recently gained attention in literature include ionized bubble-size statistics and Minkowski Functionals (Shimabukuro et al., 2017; Kapahtia et al., 2017; Yoshiura et al., 2017; Bag et al., 2018; Giri et al., 2018), especially in the context of statistics of the images of the EoR with the SKA, and the cross power spectrum of 21 cm sig-

nal with other cosmological probes (Adshead and Furlanetto, 2008; Lidz et al., 2009; Tashiro et al., 2011; Wiersma, R. P. C. et al., 2013; Natarajan et al., 2013; Vrbanec et al., 2016; Kubota et al., 2018; Yoshiura et al., 2018a,b). These theoretical developments are interesting in their own rights and are crucial to the broader progress of the field. However, to really measure them from the observations, the above three challenges must be readdressed for each statistic.

As fore 21 cm one-point statistics, we strongly believe that it is an important topic to continue. For one, one-point statistics can be used to quantify the 21 cm brightness temperature PDF. Issues on the leakage of the foreground power into the EoR window may be improved with new array design (Murray and Trott, 2018). Recent work by Morales et al. (2019) has also suggested that the power spectrum derived from the gridded visibility may offer some advantages due to the foreground power being more concentrated at the lower k modes within the foreground wedge. In such a case, the brightness temperature intensity fluctuations is simply the Fourier transform of the gridded visibility product, and looking at one-point statistics would be an obvious and beneficial analysis choice to pursue.

REFERENCES

Adshead, P. J. and Furlanetto, S. R. (2008). Reionization and the large-scale 21-cm cosmic microwave background cross-correlation. *MNRAS*, 384(1):291–304.

Ali, Z. S., Parsons, A. R., Zheng, H., Pober, J. C., Liu, A., Aguirre, J. E., Bradley, R. F., Bernardi, G., Carilli, C. L., Cheng, C., DeBoer, D. R., Dexter, M. R., Grobbelaar, J., Horrell, J., Jacobs, D. C., Klima, P., MacMahon, D. H. E., Maree, M., Moore, D. F., Razavi, N., Stefan, I. I., Walbrugh, W. P., and Walker, A. (2015). PAPER-64 Constraints on Reionization: The 21 cm Power Spectrum at z = 8.4. *ApJ*, 809(1):61.

Bag, S., Mondal, R., Sarkar, P., Bharadwaj, S., Choudhury, T. R., and Sahni, V. (2018). Studying the morphology of HI isodensity surfaces during reionization using Shapefinders and percolation analysis. *arXiv*, page arXiv:1809.05520.

Barkana, R. (2018). Possible interaction between baryons and dark-matter particles revealed by the first stars. *Nature*, 555(7694):71–74.

Barry, N., Beardsley, A. P., Byrne, R., Hazelton, B., Morales, M. F., Pober, J. C., and Sullivan, I. (2019). The FHD/εppsilon Epoch of Reionization Power Spectrum Pipeline. *arXiv*, page arXiv:1901.02980.

Beardsley, A. P., Hazelton, B. J., Morales, M. F., Arcus, W., Barnes, D., Bernardi, G., Bowman, J. D., Briggs, F. H., Bunton, J. D., Cappallo, R. J., Corey, B. E., Deshpande, A., deSouza, L., Emrich, D., Gaensler, B. M., Goeke, R., Greenhill, L. J., Herne, D., Hewitt, J. N., Johnston-Hollitt, M., Kaplan, D. L., Kasper, J. C., Kincaid, B. B., Koenig, R., Kratzenberg, E., Lonsdale, C. J., Lynch, M. J., McWhirter, S. R., Mitchell, D. A., Morgan, E., Oberoi, D., Ord, S. M., Pathikulangara, J., Prabu, T., Remillard, R. A., Rogers, A. E. E., Roshi, A., Salah, J. E., Sault, R. J., Udaya Shankar, N., Srivani, K. S., Stevens, J., Subrahmanyan, R., Tingay, S. J., Wayth, R. B., Waterson, M., Webster, R. L., Whitney, A. R., Williams, A., Williams, C. L., and Wyithe, J. S. B. (2013). The EoR sensitivity of the Murchison Widefield Array. *MNRASL*, 429(1):L5–L9.

Beardsley, A. P., Hazelton, B. J., Morales, M. F., Capallo, R. J., Goeke, R., Emrich, D., Lonsdale, C. J., Arcus, W., Barnes, D., Bernardi, G., Bowman, J. D., Bunton, J. D., Corey, B. E., Deshpande, A., deSouza, L., Gaensler, B. M., Greenhill, L. J., Herne, D., Hewitt, J. N., Kaplan, D. L., Kasper, J. C., Kincaid, B. B., Koenig, R., Kratzenberg, E., Lynch, M. J., McWhirter, S. R., Mitchell, D. A., Morgan, E., Oberoi, D., Ord, S. M., Pathikulangara, J., Prabu, T., Remillard, R. A., Rogers, A. E. E., Roshi, A., Salah, J. E., Sault, R. J., Shankar, N. U., Srivani, K. S., Stevens, J., Subrahmanyan, R., Tingay, S. J., Wayth, R. B., Waterson, M., Webster, R. L., Whitney, A. R., Williams, A., Williams, C. L., and Wyithe, J. S. B. (2012). A new layout optimization technique

for interferometric arrays, applied to the Murchison Widefield Array. *MNRAS*, 425(3):1781–1788.

Beardsley, A. P., Hazelton, B. J., Sullivan, I. S., Carroll, P., Barry, N., Rahimi, M., Pindor, B., Trott, C. M., Line, J., Jacobs, D. C., Morales, M. F., Pober, J. C., Bernardi, G., Bowman, J. D., Busch, M. P., Briggs, F., Cappallo, R. J., Corey, B. E., de Oliveira-Costa, A., Dillon, J. S., Emrich, D., Ewall-Wice, A., Feng, L., Gaensler, B. M., Goeke, R., Greenhill, L. J., Hewitt, J. N., Hurley-Walker, N., Johnston-Hollitt, M., Kaplan, D. L., Kasper, J. C., Kim, H. S., Kratzenberg, E., Lenc, E., Loeb, A., Lonsdale, C. J., Lynch, M. J., McKinley, B., McWhirter, S. R., Mitchell, D. A., Morgan, E., Neben, A. R., Thyagarajan, N., Oberoi, D., Offringa, A. R., Ord, S. M., Paul, S., Prabu, T., Procopio, P., Riding, J., Rogers, A. E. E., Roshi, A., Udaya Shankar, N., Sethi, S. K., Srivani, K. S., Subrahmanyan, R., Tegmark, M., Tingay, S. J., Waterson, M., Wayth, R. B., Webster, R. L., Whitney, A. R., Williams, A., Williams, C. L., Wu, C., and Wyithe, J. S. B. (2016). First Season MWA EoR Power spectrum Results at Redshift 7. *ApJ*, 833(1):102.

Bharadwaj, S. and Pandey, S. K. (2005). Probing non-Gaussian features in the HI distribution at the epoch of re-ionization. *MNRAS*, 358(3):968–976.

BICEP2/Keck and Planck Collaborations, Ade, P. A. R., Aghanim, N., Ahmed, Z., Aikin, R. W., Alexander, K. D., Arnaud, M., Aumont, J., Baccigalupi, C., Banday, A. J., Barkats, D., Barreiro, R. B., Bartlett, J. G., Bartolo, N., Battaner, E., Benabed, K., Benoît, A., Benoit-Lévy, A., Benton, S. J., Bernard, J. P., Bersanelli, M., Bielewicz, P., Bischoff, C. A., Bock, J. J., Bonaldi, A., Bonavera, L., Bond, J. R., Borrill, J., Bouchet, F. R., Boulanger, F., Brevik, J. A., Bucher, M., Buder, I., Bullock, E., Burigana, C., Butler, R. C., Buza, V., Calabrese, E., Cardoso, J. F., Catalano, A., Challinor, A., Chary, R. R., Chiang, H. C., Christensen, P. R., Colombo, L. P. L., Combet, C., Connors, J., Couchot, F., Coulais, A., Crill, B. P., Curto, A., Cuttaia, F., Danese, L., Davies, R. D., Davis, R. J., de Bernardis, P., de Rosa, A., de Zotti, G., Delabrouille, J., Delouis, J. M., Désert, F. X., Dickinson, C., Diego, J. M., Dole, H., Donzelli, S., Doré, O., Douspis, M., Dowell, C. D., Duband, L., Ducout, A., Dunkley, J., Dupac, X., Dvorkin, C., Efstathiou, G., Elsner, F., Ensslin, T. A., Eriksen, H. K., Falgarone, E., Filippini, J. P., Finelli, F., Fliescher, S., Forni, O., Frailis, M., Fraisse, A. A., Franceschi, E., Frejsel, A., Galeotta, S., Galli, S., Ganga, K., Ghosh, T., Giard, M., Gjerlow, E., Golwala, S. R., González-Nuevo, J., Górski, K. M., Gratton, S., Gregorio, A., Gruppuso, A., Gudmundsson, J. E., Halpern, M., Hansen, F. K., Hanson, D., Harrison, D. L., Hasselfield, M., Helou, G., Henrot-Versillé, S., Herranz, D., Hildebrandt, S. R., Hilton, G. C., Hivon, E., Hobson, M., Holmes, W. A., Hovest, W., Hristov, V. V., Huffenberger, K. M., Hui, H., Hurier, G., Irwin, K. D., Jaffe, A. H., Jaffe, T. R., Jewell, J., Jones, W. C., Juvela, M., Karakci, A., Karkare, K. S., Kaufman, J. P., Keating, B. G., Kefeli, S., Keihänen, E., Kernasovskiy, S. A., Keskitalo, R., Kisner, T. S., Kneissl, R., Knoche, J., Knox,

L., Kovac, J. M., Krachmalnicoff, N., Kunz, M., Kuo, C. L., Kurki-Suonio, H., Lagache, G., Lähteenmäki, A., Lamarre, J. M., Lasenby, A., Lattanzi, M., Lawrence, C. R., Leitch, E. M., Leonardi, R., Levrier, F., Lewis, A., Liguori, M., Lilje, P. B., Linden-Vørnle, M., López-Caniego, M., Lubin, P. M., Lueker, M., Macías-Pérez, J. F., Maffei, B., Maino, D., Mandolesi, N., Mangilli, A., Maris, M., Martin, P. G., Martínez-González, E., Masi, S., Mason, P., Matarrese, S., Megerian, K. G., Meinhold, P. R., Melchiorri, A., Mendes, L., Mennella, A., Migliaccio, M., Mitra, S., Miville-Deschênes, M. A., Moneti, A., Montier, L., Morgante, G., Mortlock, D., Moss, A., Munshi, D., Murphy, J. A., Naselsky, P., Nati, F., Natoli, P., Netterfield, C. B., Nguyen, H. T., Nørgaard-Nielsen, H. U., Noviello, F., Novikov, D., Novikov, I., O'Brient, R., Ogburn, R. W., Orlando, A., Pagano, L., Pajot, F., Paladini, R., Paoletti, D., Partridge, B., Pasian, F., Patanchon, G., Pearson, T. J., Perdereau, O., Perotto, L., Pettorino, V., Piacentini, F., Piat, M., Pietrobon, D., Plaszczynski, S., Pointecouteau, E., Polenta, G., Ponthieu, N., Pratt, G. W., Prunet, S., Pryke, C., Puget, J. L., Rachen, J. P., Reach, W. T., Rebolo, R., Reinecke, M., Remazeilles, M., Renault, C., Renzi, A., Richter, S., Ristorcelli, I., Rocha, G., Rossetti, M., Roudier, G., Rowan-Robinson, M., Rubiño-Martín, J. A., Rusholme, B., Sandri, M., Santos, D., Savelainen, M., Savini, G., Schwarz, R., Scott, D., Seiffert, M. D., Sheehy, C. D., Spencer, L. D., Staniszewski, Z. K., Stolyarov, V., Sudiwala, R., Sunyaev, R., Sutton, D., Suur-Uski, A. S., Sygnet, J. F., Tauber, J. A., Teply, G. P., Terenzi, L., Thompson, K. L., Toffolatti, L., Tolan, J. E., Tomasi, M., Tristram, M., Tucci, M., Turner, A. D., Valenziano, L., Valiviita, J., Van Tent, B., Vibert, L., Vielva, P., Vieregg, A. G., Villa, F., Wade, L. A., Wandelt, B. D., Watson, R., Weber, A. C., Wehus, I. K., White, M., White, S. D. M., Willmert, J., Wong, C. L., Yoon, K. W., Yvon, D., Zacchei, A., Zonca, A., Keck, B., and Collaborations, P. (2015). Joint Analysis of BICEP2/Keck Array and Planck Data. *Phys. Rev. Lett.*, 114(1):101301.

Bowman, J. D., Cairns, I., Kaplan, D. L., Murphy, T., Oberoi, D., Staveley-Smith, L., Arcus, W., Barnes, D. G., Bernardi, G., Briggs, F. H., Brown, S., Bunton, J. D., Burgasser, A. J., Cappallo, R. J., Chatterjee, S., Corey, B. E., Coster, A., Deshpande, A., deSouza, L., Emrich, D., Erickson, P., Goeke, R. F., Gaensler, B. M., Greenhill, L. J., Harvey-Smith, L., Hazelton, B. J., Herne, D., Hewitt, J. N., Johnston-Hollitt, M., Kasper, J. C., Kincaid, B. B., Koenig, R., Kratzenberg, E., Lonsdale, C. J., Lynch, M. J., Matthews, L. D., McWhirter, S. R., Mitchell, D. A., Morales, M. F., Morgan, E. H., Ord, S. M., Pathikulangara, J., Prabu, T., Remillard, R. A., Robishaw, T., Rogers, A. E. E., Roshi, A. A., Salah, J. E., Sault, R. J., Shankar, N. U., Srivani, K. S., Stevens, J. B., Subrahmanyan, R., Tingay, S. J., Wayth, R. B., Waterson, M., Webster, R. L., Whitney, A. R., Williams, A. J., Williams, C. L., and Wyithe, J. S. B. (2013). Science with the Murchison Widefield Array. *PASA*, 30:31.

Bowman, J. D., Morales, M. F., and Hewitt, J. N. (2009). Foreground Contamination

in Interferometric Measurements of the Redshifted 21 cm Power Spectrum. *ApJ*, 695(1):183–199.

Bowman, J. D., Rogers, A. E. E., Monsalve, R. A., Mozdzen, T. J., and Mahesh, N. (2018). An absorption profile centred at 78 megahertz in the sky-averaged spectrum. *Nature*, 555(7):67–70.

Carilli, C. L., Nikolic, B., Thyagarayan, N., and Gale-Sides, K. (2018). H I 21-cm Cosmology and the Bispectrum: Closure Diagnostics in Massively Redundant Interferometric Arrays. *RS*, 53(6):845–865.

Chapman, E., Abdalla, F. B., Bobin, J., Starck, J. L., Harker, G., Jelić, V., Labropoulos, P., Zaroubi, S., Brentjens, M. A., de Bruyn, A. G., and Koopmans, L. V. E. (2013). The scale of the problem: recovering images of reionization with Generalized Morphological Component Analysis. *MNRAS*, 429(1):165–176.

Chapman, E., Abdalla, F. B., Harker, G., Jelić, V., Labropoulos, P., Zaroubi, S., Brentjens, M. A., de Bruyn, A. G., and Koopmans, L. V. E. (2012). Foreground removal using FASTICA: a showcase of LOFAR-EoR. *MNRAS*, 423(3):2518–2532.

Cheng, C., Parsons, A. R., Kolopanis, M., Jacobs, D. C., Liu, A., Kohn, S. A., Aguirre, J. E., Pober, J. C., Ali, Z. S., Bernardi, G., Bradley, R. F., Carilli, C. L., DeBoer, D. R., Dexter, M. R., Dillon, J. S., Klima, P., MacMahon, D. H. E., Moore, D. F., Nunhokee, C. D., Walbrugh, W. P., and Walker, A. (2018). Characterizing Signal Loss in the 21 cm Reionization Power Spectrum: A Revised Study of PAPER-64. *ApJ*, 868(1):26.

Ciardi, B. and Madau, P. (2003). Probing beyond the Epoch of Hydrogen Reionization with 21 Centimeter Radiation. *ApJ*, 596(1):1–8.

Cooray, A. (2006). 21-cm Background Anisotropies Can Discern Primordial Non-Gaussianity. *Phys. Rev. Lett.*, 97(2):261301.

Datta, A., Bowman, J. D., and Carilli, C. L. (2010). Bright Source Subtraction Requirements for Redshifted 21 cm Measurements. *ApJ*, 724(1):526–538.

Datta, K. K., Jensen, H., Majumdar, S., Mellema, G., Iliev, I. T., Mao, Y., Shapiro, P. R., and Ahn, K. (2014). Light cone effect on the reionization 21-cm signal - II. Evolution, anisotropies and observational implications. *MNRAS*, 442(2):1491–1506.

Datta, K. K., Mellema, G., Mao, Y., Iliev, I. T., Shapiro, P. R., and Ahn, K. (2012). Light-cone effect on the reionization 21-cm power spectrum. *MNRAS*, 424(3):1877–1891.

DeBoer, D. R., Parsons, A. R., Aguirre, J. E., Alexander, P., Ali, Z. S., Beardsley, A. P., Bernardi, G., Bowman, J. D., Bradley, R. F., Carilli, C. L., Cheng, C., de Lera Acedo, E., Dillon, J. S., Ewall-Wice, A., Fadana, G., Fagnoni, N., Fritz, R., Furlanetto, S. R., Glendenning, B., Greig, B., Grobbelaar, J., Hazelton, B. J., Hewitt, J. N., Hickish, J., Jacobs, D. C., Julius, A., Kariseb, M., Kohn, S. A., Lekalake, T., Liu, A., Loots, A., MacMahon, D., Malan, L., Malgas, C., Maree, M., Martinot, Z., Mathison, N., Matsetela, E., Mesinger, A., Morales, M. F., Neben, A. R., Patra, N., Pieterse, S., Pober, J. C., Razavi-Ghods, N., Ringuette, J., Robnett, J., Rosie, K., Sell, R., Smith, C., Syce, A., Tegmark, M., Thyagarajan, N., Williams, P. K. G., and Zheng, H. (2017). Hydrogen Epoch of Reionization Array (HERA). *PASP*, 129(9):045001–.

Di Matteo, T., Ciardi, B., and Miniati, F. (2004). The 21-cm emission from the reionization epoch: extended and point source foregrounds. *MNRAS*, 355(4):1053–1065.

Di Matteo, T., Perna, R., Abel, T., and Rees, M. J. (2002). Radio Foregrounds for the 21 Centimeter Tomography of the Neutral Intergalactic Medium at High Redshifts. *ApJ*, 564(2):576–580.

Dillon, J. S., Liu, A., and Tegmark, M. (2013). A fast method for power spectrum and foreground analysis for 21 cm cosmology. *Phys. Rev. D*, 87(4):043005.

Dillon, J. S., Liu, A., Williams, C. L., Hewitt, J. N., Tegmark, M., Morgan, E. H., Levine, A. M., Morales, M. F., Tingay, S. J., Bernardi, G., Bowman, J. D., Briggs, F. H., Cappallo, R. C., Emrich, D., Mitchell, D. A., Oberoi, D., Prabu, T., Wayth, R., and Webster, R. L. (2014). Overcoming real-world obstacles in 21 cm power spectrum estimation: A method demonstration and results from early Murchison Widefield Array data. *Phys. Rev. D*, 89(2):23002.

Dillon, J. S., Neben, A. R., Hewitt, J. N., Tegmark, M., Barry, N., Beardsley, A. P., Bowman, J. D., Briggs, F., Carroll, P., de Oliveira-Costa, A., Ewall-Wice, A., Feng, L., Greenhill, L. J., Hazelton, B. J., Hernquist, L., Hurley-Walker, N., Jacobs, D. C., Kim, H. S., Kittiwisit, P., Lenc, E., Line, J., Loeb, A., McKinley, B., Mitchell, D. A., Morales, M. F., Offringa, A. R., Paul, S., Pindor, B., Pober, J. C., Procopio, P., Riding, J., Sethi, S., Shankar, N. U., Subrahmanyan, R., Sullivan, I., Thyagarajan, N., Tingay, S. J., Trott, C., Wayth, R. B., Webster, R. L., Wyithe, S., Bernardi, G., Cappallo, R. J., Deshpande, A. A., Johnston-Hollitt, M., Kaplan, D. L., Lonsdale, C. J., McWhirter, S. R., Morgan, E., Oberoi, D., Ord, S. M., Prabu, T., Srivani, K. S., Williams, A., and Williams, C. L. (2015). Empirical covariance modeling for 21 cm power spectrum estimation: A method demonstration and new limits from early Murchison Widefield Array 128-tile data. *Phys. Rev. D*, 91(1):123011.

Dillon, J. S. and Parsons, A. R. (2016). Redundant Array Configurations for 21 cm Cosmology. *ApJ*, 826(2):181.

Feng, C. and Holder, G. (2018). Enhanced Global Signal of Neutral Hydrogen Due to Excess Radiation at Cosmic Dawn. *ApJL*, 858(2):L17.

Furlanetto, S. R., Oh, S. P., and Briggs, F. H. (2006). Cosmology at low frequencies: The 21 cm transition and the high-redshift Universe. *Phys. Rep.*, 433(4):181–301.

Furlanetto, S. R., Zaldarriaga, M., and Hernquist, L. (2004a). Statistical Probes of Reionization with 21 Centimeter Tomography. *ApJ*, 613(1):16–22.

Furlanetto, S. R., Zaldarriaga, M., and Hernquist, L. (2004b). The Growth of H II Regions During Reionization. *ApJ*, 613(1):1–15.

Giri, S. K., Mellema, G., Dixon, K. L., and Iliev, I. T. (2018). Bubble size statistics during reionization from 21-cm tomography. *MNRAS*, 473(3):2949–2964.

Gnedin, N. Y. and Shaver, P. A. (2004). Redshifted 21 Centimeter Emission from the Pre-Reionization Era. I. Mean Signal and Linear Fluctuations. *ApJ*, 608(2):611–621.

Greig, B. and Mesinger, A. (2015). 21CMMC: an MCMC analysis tool enabling astrophysical parameter studies of the cosmic 21 cm signal. *MNRAS*, 449(4):4246–4263.

Greig, B. and Mesinger, A. (2018). 21CMMC with a 3D light-cone: the impact of the co-evolution approximation on the astrophysics of reionization and cosmic dawn. *MNRAS*, 477(3):3217–3229.

Hanumantharaju, M. C., Jayalaxmi, H., Renuka, R. K., and Ravishankar, M. A High Speed Block Convolution Using Ancient Indian Vedic Mathematics. In *International Conference on Computational Intelligence and Multimedia Applications (ICCIMA 2007)*, pages 169–173. IEEE.

Harker, G. J. A., Zaroubi, S., Thomas, R. M., Jelić, V., Labropoulos, P., Mellema, G., Iliev, I. T., Bernardi, G., Brentjens, M. A., de Bruyn, A. G., Ciardi, B., Koopmans, L. V. E., Pandey, V. N., Pawlik, A. H., Schaye, J., and Yatawatta, S. (2009). Detection and extraction of signals from the epoch of reionization using higher-order one-point statistics. *MNRAS*, 393(4):1449–1458.

Hazelton, B. J., Morales, M. F., and Sullivan, I. S. (2013). The Fundamental Multi-baseline Mode-mixing Foreground in 21 cm Epoch of Reionization Observations. *ApJ*, 770(2):156.

Heald, G. H., Pizzo, R. F., Orrú, E., Breton, R. P., Carbone, D., Ferrari, C., Hardcastle, M. J., Jurusik, W., Macario, G., Mulcahy, D., Rafferty, D., Asgekar, A., Brentjens, M., Fallows, R. A., Frieswijk, W., Toribio, M. C., Adebahr, B., Arts, M., Bell, M. R., Bonafede, A., Bray, J., Broderick, J., Cantwell, T., Carroll, P., Cendes, Y., Clarke, A. O., Croston, J., Daiboo, S., de Gasperin, F., Gregson, J., Harwood, J., Hassall, T., Heesen, V., Horneffer, A., van der Horst, A. J., Iacobelli, M., Jelic, V.,

Jones, D., Kant, D., Kokotanekov, G., Martin, P., McKean, J. P., Morabito, L. K., Nikiel-Wroczyński, B., Offringa, A., Pandey, V. N., Pandey-Pommier, M., Pietka, M., Pratley, L., Riseley, C., Rowlinson, A., Sabater, J., Scaife, A. M. M., Scheers, L. H. A., Sendlinger, K., Shulevski, A., Sipior, M., Sobey, C., Stewart, A. J., Stroe, A., Swinbank, J., Tasse, C., Trüstedt, J., Varenius, E., van Velzen, S., Vilchez, N., van Weeren, R. J., Wijnholds, S., Williams, W. L., de Bruyn, A. G., Nijboer, R., Wise, M., Alexov, A., Anderson, J., Avruch, I. M., Beck, R., Bell, M. E., van Bemmel, I., Bentum, M. J., Bernardi, G., Best, P., Breitling, F., Brouw, W. N., Bruggen, M., Butcher, H. R., Ciardi, B., Conway, J. E., de Geus, E., de Jong, A., de Vos, M., Deller, A., Dettmar, R. J., Duscha, S., Eisloffel, J., Engels, D., Falcke, H., Fender, R., Garrett, M. A., Griessmeier, J., Gunst, A. W., Hamaker, J. P., Hessels, J. W. T., Hoeft, M., Horandel, J., Holties, H. A., Intema, H., Jackson, N. J., Jütte, E., Karastergiou, A., Klijn, W. F. A., Kondratiev, V. I., Koopmans, L. V. E., Kuniyoshi, M., Kuper, G., Law, C., van Leeuwen, J., Loose, M., Maat, P., Markoff, S., McFadden, R., McKay-Bukowski, D., Mevius, M., Miller-Jones, J. C. A., Morganti, R., Munk, H., Nelles, A., Noordam, J. E., Norden, M. J., Paas, H., Polatidis, A. G., Reich, W., Renting, A., Röttgering, H., Schoenmakers, A., Schwarz, D., Sluman, J., Smirnov, O., Stappers, B. W., Steinmetz, M., Tagger, M., Tang, Y., ter Veen, S., Thoudam, S., Vermeulen, R., Vocks, C., Vogt, C., Wijers, R. A. M. J., Wucknitz, O., Yatawatta, S., and Zarka, P. (2015). The LOFAR Multifrequency Snapshot Sky Survey (MSSS). I. Survey description and first results. *A&A*, 582:A123.

Hills, R., Kulkarni, G., Meerburg, P. D., and Puchwein, E. (2018). Concerns about Modelling of Foregrounds and the 21-cm Signal in EDGES data. *arXiv*, page arXiv:1805.01421.

Hurley-Walker, N., Callingham, J. R., Hancock, P. J., Franzen, T. M. O., Hindson, L., Kapińska, A. D., Morgan, J., Offringa, A. R., Wayth, R. B., Wu, C., Zheng, Q., Murphy, T., Bell, M. E., Dwarakanath, K. S., For, B., Gaensler, B. M., Johnston-Hollitt, M., Lenc, E., Procopio, P., Staveley-Smith, L., Ekers, R., Bowman, J. D., Briggs, F., Cappallo, R. J., Deshpande, A. A., Greenhill, L., Hazelton, B. J., Kaplan, D. L., Lonsdale, C. J., McWhirter, S. R., Mitchell, D. A., Morales, M. F., Morgan, E., Oberoi, D., Ord, S. M., Prabu, T., Shankar, N. U., Srivani, K. S., Subrahmanyan, R., Tingay, S. J., Webster, R. L., Williams, A., and Williams, C. L. (2017). GaLactic and Extragalactic All-sky Murchison Widefield Array (GLEAM) survey - I. A low-frequency extragalactic catalogue. *MNRAS*, 464(1):1146–1167.

Iliev, I. T., Mellema, G., Pen, U. L., Merz, H., Shapiro, P. R., and Alvarez, M. A. (2006). Simulating cosmic reionization at large scales - I. The geometry of reionization. *MNRAS*, 369(4):1625–1638.

Jacobs, D. C., Bowman, J., and Aguirre, J. E. (2013). The Precision and Accuracy of

Early Epoch of Reionization Foreground Models: Comparing MWA and PAPER 32-antenna Source Catalogs. *ApJ*, 769(1):5.

Jacobs, D. C., Hazelton, B. J., Trott, C. M., Dillon, J. S., Pindor, B., Sullivan, I. S., Pober, J. C., Barry, N., Beardsley, A. P., Bernardi, G., Bowman, J. D., Briggs, F., Cappallo, R. J., Carroll, P., Corey, B. E., de Oliveira-Costa, A., Emrich, D., Ewall-Wice, A., Feng, L., Gaensler, B. M., Goeke, R., Greenhill, L. J., Hewitt, J. N., Hurley-Walker, N., Johnston-Hollitt, M., Kaplan, D. L., Kasper, J. C., Kim, H. S., Kratzenberg, E., Lenc, E., Line, J., Loeb, A., Lonsdale, C. J., Lynch, M. J., McKinley, B., McWhirter, S. R., Mitchell, D. A., Morales, M. F., Morgan, E., Neben, A. R., Thyagarajan, N., Oberoi, D., Offringa, A. R., Ord, S. M., Paul, S., Prabu, T., Procopio, P., Riding, J., Rogers, A. E. E., Roshi, A., Udaya Shankar, N., Sethi, S. K., Srivani, K. S., Subrahmanyan, R., Tegmark, M., Tingay, S. J., Waterson, M., Wayth, R. B., Webster, R. L., Whitney, A. R., Williams, A., Williams, C. L., Wu, C., and Wyithe, J. S. B. (2016). The Murchison Widefield Array 21 cm Power Spectrum Analysis Methodology. *ApJ*, 825(2):114.

Jacobs, D. C., Pober, J. C., Parsons, A. R., Aguirre, J. E., Ali, Z. S., Bowman, J., Bradley, R. F., Carilli, C. L., DeBoer, D. R., Dexter, M. R., Gugliucci, N. E., Klima, P., Liu, A., MacMahon, D. H. E., Manley, J. R., Moore, D. F., Stefan, I. I., and Walbrugh, W. P. (2015). Multiredshift Limits on the 21 cm Power Spectrum from PAPER. *ApJ*, 801(1):51.

Kapahtia, A., Chingangbam, P., Appleby, S., and Park, C. (2017). A novel probe of bubble size statistics and time scales of the epoch of reionization using the contour Minkowski Tensor. *arXiv*, page arXiv:1712.09195.

Kern, N. S., Liu, A., Parsons, A. R., Mesinger, A., and Greig, B. (2017). Emulating Simulations of Cosmic Dawn for 21 cm Power Spectrum Constraints on Cosmology, Reionization, and X-Ray Heating. *ApJ*, 848(1):23.

Kittiwisit, P., Bowman, J. D., Jacobs, D. C., Beardsley, A. P., and Thyagarajan, N. (2018). Sensitivity of the Hydrogen Epoch of Reionization Array and its build-out stages to one-point statistics from redshifted 21 cm observations. *MNRAS*, 474(4):4487–4499.

Kohn, S., Chichura, P. M., Igarashi, A. S., Fortino, A. F., Aguirre, J. E., Benefo, R. K., Billings, T. S., Gallardo, S., La Plante, P., Martinot, Z. E., Nunhokee, C. D., Alexander, P., Ali, Z. S., Beardsley, A. P., Bernardi, G., Bowman, J. D., Bradley, R. F., Carilli, C. L., Cheng, C., DeBoer, D. R., de Lera Acedo, E., Dillon, J. S., Ewall-Wice, A., Fadana, G., Fagnoni, N., Fritz, R., Furlanetto, S. R., Glendenning, B., Greig, B., Grobbelaar, J., Hazelton, B. J., Hewitt, J. N., Hickish, J., Jacobs, D. C., Julius, A., Kariseb, M., Kern, N. S., Kolopanis, M., Lekalake, T., Liu, A., Loots, A., MacMahon, D., Malan, L., Malgas, C., Maree, M., Mathison, N., Matsetela, E., Mesinger,

A., Morales, M. F., Neben, A. R., Nikolic, B., Parsons, A. R., Patra, N., Pieterse, S., Pober, J. C., Razavi-Ghods, N., Ringuette, J., Robnett, J., Rosie, K., Sell, R., Smith, C., Syce, A., Tegmark, M., Thyagarajan, N., Williams, P. K. G., and Zheng, H. (2018). Polarized Foreground Power Spectra from the HERA-19 Commissioning Array. *arXiv*, page arXiv:1802.04151.

Kubota, K., Yoshiura, S., Takahashi, K., Hasegawa, K., Yajima, H., Ouchi, M., Pindor, B., and Webster, R. L. (2018). Detectability of the 21-cm signal during the epoch of reionization with 21-cm Lyman α emitter cross-correlation - I. *MNRAS*, 479(2):2754–2766.

Lidz, A. and Malloy, M. (2014). On Modeling and Measuring the Temperature of the z ~ 5 Intergalactic Medium. *ApJ*, 788(2):175.

Lidz, A., Zahn, O., Furlanetto, S. R., McQuinn, M., Hernquist, L., and Zaldarriaga, M. (2009). Probing Reionization with the 21 cm Galaxy Cross-Power Spectrum. *ApJ*, 690(1):252–266.

Lidz, A., Zahn, O., McQuinn, M., Zaldarriaga, M., Dutta, S., and Hernquist, L. (2007). Higher Order Contributions to the 21 cm Power Spectrum. *ApJ*, 659(2):865–876.

Liu, A., Parsons, A. R., and Trott, C. M. (2014). Epoch of reionization window. II. Statistical methods for foreground wedge reduction. *Phys. Rev. D*, 90(2):023019.

Liu, A. and Tegmark, M. (2011). A method for 21 cm power spectrum estimation in the presence of foregrounds. *Phys. Rev. D*, 83(1):103006.

Liu, A., Tegmark, M., Bowman, J., Hewitt, J., and Zaldarriaga, M. (2009). An improved method for 21-cm foreground removal. *MNRAS*, 398(1):401–406.

Loeb, A. (2006). The dark ages of the Universe. *Scientific American*, 295.

Madau, P., Meiksin, A., and Rees, M. J. (1997). 21 Centimeter Tomography of the Intergalactic Medium at High Redshift. *ApJ*, 475(2):429–444.

Majumdar, S., Pritchard, J. R., Mondal, R., Watkinson, C. A., Bharadwaj, S., and Mellema, G. (2018). Quantifying the non-Gaussianity in the EoR 21-cm signal through bispectrum. *MNRAS*, 476(3):4007–4024.

McQuinn, M., Lidz, A., Zahn, O., Dutta, S., Hernquist, L., and Zaldarriaga, M. (2007). The morphology of HII regions during reionization. *MNRAS*, 377(3):1043–1063.

McQuinn, M., Zahn, O., Zaldarriaga, M., Hernquist, L., and Furlanetto, S. R. (2006). Cosmological Parameter Estimation Using 21 cm Radiation from the Epoch of Reionization. *ApJ*, 653(2):815–834.

Mellema, G., Iliev, I. T., Pen, U.-L., and Shapiro, P. R. (2006). Simulating cosmic reionization at large scales - II. The 21-cm emission features and statistical signals. *MNRAS*, 372(2):679–692.

Mellema, G., Koopmans, L. V. E., Abdalla, F. A., Bernardi, G., Ciardi, B., Daiboo, S., de Bruyn, A. G., Datta, K. K., Falcke, H., Ferrara, A., Iliev, I. T., Iocco, F., Jelić, V., Jensen, H., Joseph, R., Labroupoulos, P., Meiksin, A., Mesinger, A., Offringa, A. R., Pandey, V. N., Pritchard, J. R., Santos, M. G., Schwarz, D. J., Semelin, B., Vedantham, H., Yatawatta, S., and Zaroubi, S. (2013). Reionization and the Cosmic Dawn with the Square Kilometre Array. *Exp Astron*, 36(1):235–318.

Mesinger, A., Furlanetto, S., and Cen, R. (2011). 21CMFAST: a fast, seminumerical simulation of the high-redshift 21-cm signal. *MNRAS*, 411(2):955–972.

Mitchell, D. A., Greenhill, L. J., Wayth, R. B., Sault, R. J., Lonsdale, C. J., Cappallo, R. J., Morales, M. F., and Ord, S. M. (2008). Real-Time Calibration of the Murchison Widefield Array. *IEEE J. Sel. Topics Signal Process.*, 2(5):707–717.

Mondal, R., Bharadwaj, S., Majumdar, S., Bera, A., and Acharyya, A. (2015). The effect of non-Gaussianity on error predictions for the Epoch of Reionization (EoR) 21-cm power spectrum. *MNRASL*, 449(1):L41–L45.

Morales, M. F., Beardsley, A., Pober, J., Barry, N., Hazelton, B., Jacobs, D., and Sullivan, I. (2019). Understanding the diversity of 21 cm cosmology analyses. *MNRAS*, 483(2):2207–2216.

Morales, M. F., Bowman, J. D., and Hewitt, J. N. (2006). Improving Foreground Subtraction in Statistical Observations of 21 cm Emission from the Epoch of Reionization. *ApJ*, 648(2):767–773.

Morales, M. F., Hazelton, B., Sullivan, I., and Beardsley, A. (2012). Four Fundamental Foreground Power Spectrum Shapes for 21 cm Cosmology Observations. *ApJ*, 752(2):137.

Morales, M. F. and Hewitt, J. (2004). Toward Epoch of Reionization Measurements with Wide-Field Radio Observations. *ApJ*, 615(1):7–18.

Morales, M. F. and Wyithe, J. S. B. (2010). Reionization and Cosmology with 21-cm Fluctuations. *ARA&A*, 48:127–171.

Mozdzen, T. J., Bowman, J. D., Monsalve, R. A., and Rogers, A. E. E. (2016). Limits on foreground subtraction from chromatic beam effects in global redshifted 21 cm measurements. *MNRAS*, 455(4):3890–3900.

Muñoz, J. B., Ali-Haïmoud, Y., and Kamionkowski, M. (2015). Primordial non-gaussianity from the bispectrum of 21-cm fluctuations in the dark ages. *Phys. Rev. D*, 92(8):083508.

Murray, S. G. and Trott, C. M. (2018). The effect of baseline layouts on the EoR foreground wedge: a semi-analytical approach. *arXiv*, page arXiv:1810.10712.

Natarajan, A., Battaglia, N., Trac, H., Pen, U. L., and Loeb, A. (2013). Reionization on Large Scales. II. Detecting Patchy Reionization through Cross-correlation of the Cosmic Microwave Background. *ApJ*, 776(2):82.

Oh, S. P. and Mack, K. J. (2003). Foregrounds for 21-cm observations of neutral gas at high redshift. *MNRAS*, 346(3):871–877.

Paciga, G., Albert, J. G., Bandura, K., Chang, T.-C., Gupta, Y., Hirata, C., Odegova, J., Pen, U.-L., Peterson, J. B., Roy, J., Shaw, J. R., Sigurdson, K., and Voytek, T. (2013). A simulation-calibrated limit on the H I power spectrum from the GMRT Epoch of Reionization experiment. *MNRAS*, 433(1):639–647.

Parsons, A. R., Backer, D. C., Foster, G. S., Wright, M. C. H., Bradley, R. F., Gugliucci, N. E., Parashare, C. R., Benoit, E. E., Aguirre, J. E., Jacobs, D. C., Carilli, C. L., Herne, D., Lynch, M. J., Manley, J. R., and Werthimer, D. J. (2010). The Precision Array for Probing the Epoch of Re-ionization: Eight Station Results. *AJ*, 139(4):1468–1480.

Parsons, A. R., Liu, A., Aguirre, J. E., Ali, Z. S., Bradley, R. F., Carilli, C. L., DeBoer, D. R., Dexter, M. R., Gugliucci, N. E., Jacobs, D. C., Klima, P., MacMahon, D. H. E., Manley, J. R., Moore, D. F., Pober, J. C., Stefan, I. I., and Walbrugh, W. P. (2014). New Limits on 21 cm Epoch of Reionization from PAPER-32 Consistent with an X-Ray Heated Intergalactic Medium at z = 7.7. *ApJ*, 788(2):106.

Parsons, A. R., Pober, J. C., Aguirre, J. E., Carilli, C. L., Jacobs, D. C., and Moore, D. F. (2012). A Per-baseline, Delay-spectrum Technique for Accessing the 21 cm Cosmic Reionization Signature. *ApJ*, 756(2):165.

Patil, A. H., Yatawatta, S., Koopmans, L. V. E., de Bruyn, A. G., Brentjens, M. A., Zaroubi, S., Asad, K. M. B., Hatef, M., Jelic, V., Mevius, M., Offringa, A. R., Pandey, V. N., Vedantham, H., Abdalla, F. B., Brouw, W. N., Chapman, E., Ciardi, B., Gehlot, B. K., Ghosh, A., Harker, G., Iliev, I. T., Kakiichi, K., Majumdar, S., Mellema, G., Silva, M. B., Schaye, J., Vrbanec, D., and Wijnholds, S. J. (2017). Upper Limits on the 21 cm Epoch of Reionization Power Spectrum from One Night with LOFAR. *ApJ*, 838(1):65.

Paul, S., Sethi, S. K., Morales, M. F., Dwarkanath, K. S., Udaya Shankar, N., Subrahmanyan, R., Barry, N., Beardsley, A. P., Bowman, J. D., Briggs, F., Carroll,

P., de Oliveira-Costa, A., Dillon, J. S., Ewall-Wice, A., Feng, L., Greenhill, L. J., Gaensler, B. M., Hazelton, B. J., Hewitt, J. N., Hurley-Walker, N., Jacobs, D. J., Kim, H.-S., Kittiwisit, P., Lenc, E., Line, J., Loeb, A., McKinley, B., Mitchell, D. A., Neben, A. R., Offringa, A. R., Pindor, B., Pober, J. C., Procopio, P., Riding, J., Sullivan, I. S., Tegmark, M., Thyagarajan, N., Tingay, S. J., Trott, C. M., Wayth, R. B., Webster, R. L., Wyithe, J. S. B., Cappallo, R., Johnston-Hollitt, M., Kaplan, D. L., Lonsdale, C. J., McWhirter, S. R., Morgan, E., Oberoi, D., Ord, S. M., Prabu, T., Srivani, K. S., Williams, A., and Williams, C. L. (2016). Delay Spectrum with Phase-tracking Arrays: Extracting the HI Power Spectrum from the Epoch of Reionization. *ApJ*, 833(2):213.

Pearson, K. (1905). "Das Fehlergesetz und Seine Verallgemeinerungen Durch Fechner und Pearson." A Rejoinder. *Biometrika*, 4(1/2):169.

Pillepich, A., Porciani, C., and Matarrese, S. (2007). The Bispectrum of Redshifted 21 Centimeter Fluctuations from the Dark Ages. *ApJ*, 662(1):1–14.

Planck Collaboration, Aghanim, N., Akrami, Y., Ashdown, M., Aumont, J., Baccigalupi, C., Ballardini, M., Banday, A. J., Barreiro, R. B., Bartolo, N., Basak, S., Battye, R., Benabed, K., Bernard, J. P., Bersanelli, M., Bielewicz, P., Bock, J. J., Bond, J. R., Borrill, J., Bouchet, F. R., Boulanger, F., Bucher, M., Burigana, C., Butler, R. C., Calabrese, E., Cardoso, J. F., Carron, J., Challinor, A., Chiang, H. C., Chluba, J., Colombo, L. P. L., Combet, C., Contreras, D., Crill, B. P., Cuttaia, F., de Bernardis, P., de Zotti, G., Delabrouille, J., Delouis, J. M., Di Valentino, E., Diego, J. M., Doré, O., Douspis, M., Ducout, A., Dupac, X., Dusini, S., Efstathiou, G., Elsner, F., Ensslin, T. A., Eriksen, H. K., Fantaye, Y., Farhang, M., Fergusson, J., Fernandez-Cobos, R., Finelli, F., Forastieri, F., Frailis, M., Franceschi, E., Frolov, A., Galeotta, S., Galli, S., Ganga, K., Génova-Santos, R. T., Gerbino, M., Ghosh, T., González-Nuevo, J., Górski, K. M., Gratton, S., Gruppuso, A., Gudmundsson, J. E., Hamann, J., Handley, W., Herranz, D., Hivon, E., Huang, Z., Jaffe, A. H., Jones, W. C., Karakci, A., Keihänen, E., Keskitalo, R., Kiiveri, K., Kim, J., Kisner, T. S., Knox, L., Krachmalnicoff, N., Kunz, M., Kurki-Suonio, H., Lagache, G., Lamarre, J. M., Lasenby, A., Lattanzi, M., Lawrence, C. R., Le Jeune, M., Lemos, P., Lesgourgues, J., Levrier, F., Lewis, A., Liguori, M., Lilje, P. B., Lilley, M., Lindholm, V., López-Caniego, M., Lubin, P. M., Ma, Y. Z., Macías-Pérez, J. F., Maggio, G., Maino, D., Mandolesi, N., Mangilli, A., Marcos-Caballero, A., Maris, M., Martin, P. G., Martinelli, M., Martínez-González, E., Matarrese, S., Mauri, N., McEwen, J. D., Meinhold, P. R., Melchiorri, A., Mennella, A., Migliaccio, M., Millea, M., Mitra, S., Miville-Deschênes, M. A., Molinari, D., Montier, L., Morgante, G., Moss, A., Natoli, P., Nørgaard-Nielsen, H. U., Pagano, L., Paoletti, D., Partridge, B., Patanchon, G., Peiris, H. V., Perrotta, F., Pettorino, V., Piacentini, F., Polastri, L., Polenta, G., Puget, J. L., Rachen, J. P., Reinecke, M., Remazeilles, M., Renzi, A., Rocha, G., Rosset, C., Roudier, G., Rubiño-Martín, J. A., Ruiz-Granados, B., Salvati, L., San-

dri, M., Savelainen, M., Scott, D., Shellard, E. P. S., Sirignano, C., Sirri, G., Spencer, L. D., Sunyaev, R., Suur-Uski, A. S., Tauber, J. A., Tavagnacco, D., Tenti, M., Toffolatti, L., Tomasi, M., Trombetti, T., Valenziano, L., Valiviita, J., Van Tent, B., Vibert, L., Vielva, P., Villa, F., Vittorio, N., Wandelt, B. D., Wehus, I. K., White, M., White, S. D. M., Zacchei, A., and Zonca, A. (2018). Planck 2018 results. VI. Cosmological parameters. *arXiv*, page arXiv:1807.06209.

Pober, J. C., Parsons, A. R., Aguirre, J. E., Ali, Z., Bradley, R. F., Carilli, C. L., DeBoer, D., Dexter, M., Gugliucci, N. E., Jacobs, D. C., Klima, P. J., MacMahon, D., Manley, J., Moore, D. F., Stefan, I. I., and Walbrugh, W. P. (2013). Opening the 21 cm Epoch of Reionization Window: Measurements of Foreground Isolation with PAPER. *ApJL*, 768(2):L36.

Prabu, T., Srivani, K. S., Roshi, D. A., Kamini, P. A., Madhavi, S., Emrich, D., Crosse, B., Williams, A. J., Waterson, M., Deshpande, A. A., Shankar, N. U., Subrahmanyan, R., Briggs, F. H., Goeke, R. F., Tingay, S. J., Johnston-Hollitt, M., R, G. M., Morgan, E. H., Pathikulangara, J., Bunton, J. D., Hampson, G., Williams, C., Ord, S. M., Wayth, R. B., Kumar, D., Morales, M. F., deSouza, L., Kratzenberg, E., Pallot, D., McWhirter, R., Hazelton, B. J., Arcus, W., Barnes, D. G., Bernardi, G., Booler, T., Bowman, J. D., Cappallo, R. J., Corey, B. E., Greenhill, L. J., Herne, D., Hewitt, J. N., Kaplan, D. L., Kasper, J. C., Kincaid, B. B., Koenig, R., Lonsdale, C. J., Lynch, M. J., Mitchell, D. A., Oberoi, D., Remillard, R. A., Rogers, A. E., Salah, J. E., Sault, R. J., Stevens, J. B., Tremblay, S., Webster, R. L., Whitney, A. R., and Wyithe, S. B. (2015). A digital-receiver for the MurchisonWidefield Array. *Exp Astron*, 39(1):73–93.

Pritchard, J. R. and Loeb, A. (2012). 21 cm cosmology in the 21st century. *Rep. Prog. Phys.*, 75(8):6901.

Robertson, B. E., Ellis, R. S., Furlanetto, S. R., and Dunlop, J. S. (2015). Cosmic Reionization and Early Star-forming Galaxies: A Joint Analysis of New Constraints from Planck and the Hubble Space Telescope. *ApJL*, 802(2):L19.

Robertson, B. E., Furlanetto, S. R., Schneider, E., Charlot, S., Ellis, R. S., Stark, D. P., McLure, R. J., Dunlop, J. S., Koekemoer, A., Schenker, M. A., Ouchi, M., Ono, Y., Curtis-Lake, E., Rogers, A. B., Bowler, R. A. A., and Cirasuolo, M. (2013). New Constraints on Cosmic Reionization from the 2012 Hubble Ultra Deep Field Campaign. *ApJ*, 768(1):71.

Santos, M. G., Cooray, A., and Knox, L. (2005). Multifrequency Analysis of 21 Centimeter Fluctuations from the Era of Reionization. *ApJ*, 625(2):575–587.

Schmit, C. J., Heavens, A. F., and Pritchard, J. R. (2018). The gravitational and lensing-ISW bispectrum of 21cm radiation. *arXiv*, page arXiv:1810.00973.

Schmit, C. J. and Pritchard, J. R. (2018). Emulation of reionization simulations for Bayesian inference of astrophysics parameters using neural networks. *MNRAS*, 475(1):1213–1223.

Scott, D. and Rees, M. J. (1990). The 21-cm line at high redshift: a diagnostic for the origin of large scale structure. *MNRAS*, 247:510–.

Shimabukuro, H., Yoshiura, S., Takahashi, K., Yokoyama, S., and Ichiki, K. (2015). Studying 21cm power spectrum with one-point statistics. *MNRAS*, 451(1):467–474.

Shimabukuro, H., Yoshiura, S., Takahashi, K., Yokoyama, S., and Ichiki, K. (2016). 21 cm line bispectrum as a method to probe cosmic dawn and epoch of reionization. *MNRAS*, 458(3):3003–3011.

Shimabukuro, H., Yoshiura, S., Takahashi, K., Yokoyama, S., and Ichiki, K. (2017). Constraining the epoch-of-reionization model parameters with the 21-cm bispectrum. *MNRAS*, 468(2):1542–1550.

Sullivan, I. S., Morales, M. F., Hazelton, B. J., Arcus, W., Barnes, D., Bernardi, G., Briggs, F. H., Bowman, J. D., Bunton, J. D., Cappallo, R. J., Corey, B. E., Deshpande, A., deSouza, L., Emrich, D., Gaensler, B. M., Goeke, R., Greenhill, L. J., Herne, D., Hewitt, J. N., Johnston-Hollitt, M., Kaplan, D. L., Kasper, J. C., Kincaid, B. B., Koenig, R., Kratzenberg, E., Lonsdale, C. J., Lynch, M. J., McWhirter, S. R., Mitchell, D. A., Morgan, E., Oberoi, D., Ord, S. M., Pathikulangara, J., Prabu, T., Remillard, R. A., Rogers, A. E. E., Roshi, A., Salah, J. E., Sault, R. J., Udaya Shankar, N., Srivani, K. S., Stevens, J., Subrahmanyan, R., Tingay, S. J., Wayth, R. B., Waterson, M., Webster, R. L., Whitney, A. R., Williams, A., Williams, C. L., and Wyithe, J. S. B. (2012). Fast Holographic Deconvolution: A New Technique for Precision Radio Interferometry. *ApJ*, 759(1):17.

Tashiro, H., Aghanim, N., Langer, M., Douspis, M., Zaroubi, S., and Jelić, V. (2011). Second order cross-correlation between kinetic Sunyaev-Zel'dovich effect and 21-cm fluctuations from the epoch of reionization. *MNRAS*, 414(4):3424–3433.

Tegmark, M. (1997a). CMB mapping experiments: A designer's guide. *Physical Review D (Particles*, 56(8):4514–4529.

Tegmark, M. (1997b). Measuring Cosmological Parameters with Galaxy Surveys. *Phys. Rev. Lett.*, 79(2):3806–3809.

Thompson, A. R., Moran, J. M., and Swenson, G. W. J. (2017). *Interferometry and Synthesis in Radio Astronomy, 3rd Edition*. Interferometry and Synthesis in Radio Astronomy, National Radio Astronomy Observatory.

Thyagarajan, N., Jacobs, D. C., Bowman, J. D., Barry, N., Beardsley, A. P., Bernardi, G., Briggs, F., Cappallo, R. J., Carroll, P., Corey, B. E., de Oliveira-Costa, A., Dillon, J. S., Emrich, D., Ewall-Wice, A., Feng, L., Goeke, R., Greenhill, L. J., Hazelton, B. J., Hewitt, J. N., Hurley-Walker, N., Johnston-Hollitt, M., Kaplan, D. L., Kasper, J. C., Kim, H.-S., Kittiwisit, P., Kratzenberg, E., Lenc, E., Line, J., Loeb, A., Lonsdale, C. J., Lynch, M. J., McKinley, B., McWhirter, S. R., Mitchell, D. A., Morales, M. F., Morgan, E., Neben, A. R., Oberoi, D., Offringa, A. R., Ord, S. M., Paul, S., Pindor, B., Pober, J. C., Prabu, T., Procopio, P., Riding, J., Rogers, A. E. E., Roshi, A., Udaya Shankar, N., Sethi, S. K., Srivani, K. S., Subrahmanyan, R., Sullivan, I. S., Tegmark, M., Tingay, S. J., Trott, C. M., Waterson, M., Wayth, R. B., Webster, R. L., Whitney, A. R., Williams, A., Williams, C. L., Wu, C., and Wyithe, J. S. B. (2015a). Foregrounds in Wide-field Redshifted 21 cm Power Spectra. *ApJ*, 804(1):14.

Thyagarajan, N., Jacobs, D. C., Bowman, J. D., Barry, N., Beardsley, A. P., Bernardi, G., Briggs, F., Cappallo, R. J., Carroll, P., Deshpande, A. A., de Oliveira-Costa, A., Dillon, J. S., Ewall-Wice, A., Feng, L., Greenhill, L. J., Hazelton, B. J., Hernquist, L., Hewitt, J. N., Hurley-Walker, N., Johnston-Hollitt, M., Kaplan, D. L., Kim, H.-S., Kittiwisit, P., Lenc, E., Line, J., Loeb, A., Lonsdale, C. J., McKinley, B., McWhirter, S. R., Mitchell, D. A., Morales, M. F., Morgan, E., Neben, A. R., Oberoi, D., Offringa, A. R., Ord, S. M., Paul, S., Pindor, B., Pober, J. C., Prabu, T., Procopio, P., Riding, J., Udaya Shankar, N., Sethi, S. K., Srivani, K. S., Subrahmanyan, R., Sullivan, I. S., Tegmark, M., Tingay, S. J., Trott, C. M., Wayth, R. B., Webster, R. L., Williams, A., Williams, C. L., and Wyithe, J. S. B. (2015b). Confirmation of Wide-field Signatures in Redshifted 21 cm Power Spectra. *ApJL*, 807(2):L28.

Thyagarajan, N., Parsons, A. R., DeBoer, D. R., Bowman, J. D., Ewall-Wice, A. M., Neben, A. R., and Patra, N. (2016). Effects of Antenna Beam Chromaticity on Redshifted 21 cm Power Spectrum and Implications for Hydrogen Epoch of Reionization Array. *ApJ*, 825(1):9.

Thyagarajan, N., Udaya Shankar, N., Subrahmanyan, R., Arcus, W., Bernardi, G., Bowman, J. D., Briggs, F., Bunton, J. D., Cappallo, R. J., Corey, B. E., deSouza, L., Emrich, D., Gaensler, B. M., Goeke, R. F., Greenhill, L. J., Hazelton, B. J., Herne, D., Hewitt, J. N., Johnston-Hollitt, M., Kaplan, D. L., Kasper, J. C., Kincaid, B. B., Koenig, R., Kratzenberg, E., Lonsdale, C. J., Lynch, M. J., McWhirter, S. R., Mitchell, D. A., Morales, M. F., Morgan, E. H., Oberoi, D., Ord, S. M., Pathikulangara, J., Remillard, R. A., Rogers, A. E. E., Anish Roshi, D., Salah, J. E., Sault, R. J., Srivani, K. S., Stevens, J. B., Thiagaraj, P., Tingay, S. J., Wayth, R. B., Waterson, M., Webster, R. L., Whitney, A. R., Williams, A. J., Williams, C. L., and Wyithe, J. S. B. (2013). A Study of Fundamental Limitations to Statistical Detection of Redshifted H I from the Epoch of Reionization. *ApJ*, 776(1):6.

Tingay, S. J., Goeke, R., Bowman, J. D., Emrich, D., Ord, S. M., Mitchell, D. A., Morales, M. F., Booler, T., Crosse, B., Wayth, R. B., Lonsdale, C. J., Tremblay, S., Pallot, D., Colegate, T., Wicenec, A., Kudryavtseva, N., Arcus, W., Barnes, D., Bernardi, G., Briggs, F., Burns, S., Bunton, J. D., Cappallo, R. J., Corey, B. E., Deshpande, A., deSouza, L., Gaensler, B. M., Greenhill, L. J., Hall, P. J., Hazelton, B. J., Herne, D., Hewitt, J. N., Johnston-Hollitt, M., Kaplan, D. L., Kasper, J. C., Kincaid, B. B., Koenig, R., Kratzenberg, E., Lynch, M. J., McKinley, B., McWhirter, S. R., Morgan, E., Oberoi, D., Pathikulangara, J., Prabu, T., Remillard, R. A., Rogers, A. E. E., Roshi, A., Salah, J. E., Sault, R. J., Udaya Shankar, N., Schlagenhaufer, F., Srivani, K. S., Stevens, J., Subrahmanyan, R., Waterson, M., Webster, R. L., Whitney, A. R., Williams, A., Williams, C. L., and Wyithe, J. S. B. (2013). The Murchison Widefield Array: The Square Kilometre Array Precursor at Low Radio Frequencies. *PASA*, 30:7.

Tozzi, P., Madau, P., Meiksin, A., and Rees, M. J. (2000). Radio Signatures of H I at High Redshift: Mapping the End of the "Dark Ages". *ApJ*, 528(2):597–606.

Trott, C. M., Pindor, B., Procopio, P., Wayth, R. B., Mitchell, D. A., McKinley, B., Tingay, S. J., Barry, N., Beardsley, A. P., Bernardi, G., Bowman, J. D., Briggs, F., Cappallo, R. J., Carroll, P., de Oliveira-Costa, A., Dillon, J. S., Ewall-Wice, A., Feng, L., Greenhill, L. J., Hazelton, B. J., Hewitt, J. N., Hurley-Walker, N., Johnston-Hollitt, M., Jacobs, D. C., Kaplan, D. L., Kim, H. S., Lenc, E., Line, J., Loeb, A., Lonsdale, C. J., Morales, M. F., Morgan, E., Neben, A. R., Thyagarajan, N., Oberoi, D., Offringa, A. R., Ord, S. M., Paul, S., Pober, J. C., Prabu, T., Riding, J., Udaya Shankar, N., Sethi, S. K., Srivani, K. S., Subrahmanyan, R., Sullivan, I. S., Tegmark, M., Webster, R. L., Williams, A., Williams, C. L., Wu, C., and Wyithe, J. S. B. (2016). CHIPS: The Cosmological H i Power Spectrum Estimator. *ApJ*, 818(2):139.

Trott, C. M., Wayth, R. B., and Tingay, S. J. (2012). The Impact of Point-source Subtraction Residuals on 21 cm Epoch of Reionization Estimation. *ApJ*, 757(1):101.

van Haarlem, M. P., Wise, M. W., Gunst, A. W., Heald, G., McKean, J. P., Hessels, J. W. T., de Bruyn, A. G., Nijboer, R., Swinbank, J., Fallows, R., Brentjens, M., Nelles, A., Beck, R., Falcke, H., Fender, R., Horandel, J., Koopmans, L. V. E., Mann, G., Miley, G., Röttgering, H., Stappers, B. W., Wijers, R. A. M. J., Zaroubi, S., van den Akker, M., Alexov, A., Anderson, J., Anderson, K., van Ardenne, A., Arts, M., Asgekar, A., Avruch, I. M., Batejat, F., Bähren, L., Bell, M. E., Bell, M. R., van Bemmel, I., Bennema, P., Bentum, M. J., Bernardi, G., Best, P., Birzan, L., Bonafede, A., Boonstra, A. J., Braun, R., Bregman, J., Breitling, F., van de Brink, R. H., Broderick, J., Broekema, P. C., Brouw, W. N., Bruggen, M., Butcher, H. R., van Cappellen, W., Ciardi, B., Coenen, T., Conway, J., Coolen, A., Corstanje, A., Damstra, S., Davies, O., Deller, A. T., Dettmar, R. J., van Diepen, G., Dijkstra, K., Donker, P., Doorduin, A., Dromer, J., Drost, M., van Duin, A., Eisloffel, J., van Enst, J., Ferrari, C.,

Frieswijk, W., Gankema, H., Garrett, M. A., de Gasperin, F., Gerbers, M., de Geus, E., Grießmeier, J. M., Grit, T., Gruppen, P., Hamaker, J. P., Hassall, T., Hoeft, M., Holties, H. A., Horneffer, A., van der Horst, A., van Houwelingen, A., Huijgen, A., Iacobelli, M., Intema, H., Jackson, N., Jelic, V., de Jong, A., Juette, E., Kant, D., Karastergiou, A., Koers, A., Kollen, H., Kondratiev, V. I., Kooistra, E., Koopman, Y., Koster, A., Kuniyoshi, M., Kramer, M., Kuper, G., Lambropoulos, P., Law, C., van Leeuwen, J., Lemaitre, J., Loose, M., Maat, P., Macario, G., Markoff, S., Masters, J., McFadden, R. A., McKay-Bukowski, D., Meijering, H., Meulman, H., Mevius, M., Middelberg, E., Millenaar, R., Miller-Jones, J. C. A., Mohan, R. N., Mol, J. D., Morawietz, J., Morganti, R., Mulcahy, D. D., Mulder, E., Munk, H., Nieuwenhuis, L., van Nieuwpoort, R., Noordam, J. E., Norden, M., Noutsos, A., Offringa, A. R., Olofsson, H., Omar, A., Orrú, E., Overeem, R., Paas, H., Pandey-Pommier, M., Pandey, V. N., Pizzo, R., Polatidis, A., Rafferty, D., Rawlings, S., Reich, W., de Reijer, J. P., Reitsma, J., Renting, G. A., Riemers, P., Rol, E., Romein, J. W., Roosjen, J., Ruiter, M., Scaife, A., van der Schaaf, K., Scheers, B., Schellart, P., Schoenmakers, A., Schoonderbeek, G., Serylak, M., Shulevski, A., Sluman, J., Smirnov, O., Sobey, C., Spreeuw, H., Steinmetz, M., Sterks, C. G. M., Stiepel, H. J., Stuurwold, K., Tagger, M., Tang, Y., Tasse, C., Thomas, I., Thoudam, S., Toribio, M. C., van der Tol, B., Usov, O., van Veelen, M., van der Veen, A. J., ter Veen, S., Verbiest, J. P. W., Vermeulen, R., Vermaas, N., Vocks, C., Vogt, C., de Vos, M., van der Wal, E., van Weeren, R., Weggemans, H., Weltevrede, P., White, S., Wijnholds, S. J., Wilhelmsson, T., Wucknitz, O., Yatawatta, S., Zarka, P., Zensus, A., and van Zwieten, J. (2013). LOFAR: The LOw-Frequency ARray. *A&A*, 556:A2.

Vedantham, H., Udaya Shankar, N., and Subrahmanyan, R. (2012). Imaging the Epoch of Reionization: Limitations from Foreground Confusion and Imaging Algorithms. *ApJ*, 745(2):176.

Vrbanec, D., Ciardi, B., Jelić, V., Jensen, H., Zaroubi, S., Fernandez, E. R., Ghosh, A., Iliev, I. T., Kakiichi, K., Koopmans, L. V. E., and Mellema, G. (2016). Predictions for the 21 cm-galaxy cross-power spectrum observable with LOFAR and Subaru. *MNRAS*, 457(1):666–675.

Wang, J., Xu, H., An, T., Gu, J., Guo, X., Li, W., Wang, Y., Liu, C., Martineau-Huynh, O., and Wu, X.-P. (2013). Exploring the Cosmic Reionization Epoch in Frequency Space: An Improved Approach to Remove the Foreground in 21 cm Tomography. *ApJ*, 763(2):90.

Wang, X., Tegmark, M., Santos, M. G., and Knox, L. (2006). 21 cm Tomography with Foregrounds. *ApJ*, 650(2):529–537.

Watkinson, C. A., Majumdar, S., Pritchard, J. R., and Mondal, R. (2017). A fast estimator for the bispectrum and beyond - a practical method for measuring non-Gaussianity in 21-cm maps. *MNRAS*, 472:2436–2446.

Watkinson, C. A., Mesinger, A., Pritchard, J. R., and Sobacchi, E. (2015). 21-cm signatures of residual H I inside cosmic H II regions during reionization. *MNRAS*, 449(3):3202–3211.

Watkinson, C. A. and Pritchard, J. R. (2014). Distinguishing models of reionization using future radio observations of 21-cm 1-point statistics. *MNRAS*, 443(4):3090–3106.

Watkinson, C. A. and Pritchard, J. R. (2015). The impact of spin-temperature fluctuations on the 21-cm moments. *MNRAS*, 454(2):1416–1431.

Wayth, R. B., Tingay, S. J., Trott, C. M., Emrich, D., Johnston-Hollitt, M., McKinley, B., Gaensler, B. M., Beardsley, A. P., Booler, T., Crosse, B., Franzen, T. M. O., Horsley, L., Kaplan, D. L., Kenney, D., Morales, M. F., Pallot, D., Sleap, G., Steele, K., Walker, M., Williams, A., Wu, C., Cairns, I. H., Filipovic, M. D., Johnston, S., Murphy, T., Quinn, P., Staveley-Smith, L., Webster, R., and Wyithe, J. S. B. (2018). The Phase II Murchison Widefield Array: Design Overview. *arXiv*, page arXiv:1809.06466.

Wiersma, R. P. C., Ciardi, B., Thomas, R. M., Harker, G. J. A., Zaroubi, S., Bernardi, G., Brentjens, M., de Bruyn, A. G., Daiboo, S., Jelic, V., Kazemi, S., Koopmans, L. V. E., Labropoulos, P., Martinez, O., Mellema, G., Offringa, A., Pandey, V. N., Schaye, J., Veligatla, V., Vedantham, H., and Yatawatta, S. (2013). LOFAR insights into the epoch of reionization from the cross-power spectrum of 21 cm emission and galaxies. *MNRAS*, page 1257.

Yoshiura, S., Ichiki, K., Pindor, B., Takahashi, K., Tashiro, H., and Trott, C. M. (2018a). First Limits on the Cross Power Spectrum of 21 cm Line and Cosmic Microwave Background using Murchison Widefield Array Data. *arXiv*, page arXiv:1803.00756.

Yoshiura, S., Line, J. L. B., Kubota, K., Hasegawa, K., and Takahashi, K. (2018b). Detectability of 21 cm-signal during the Epoch of Reionization with 21 cm-Lyman-α emitter cross-correlation - II. Foreground contamination. *MNRAS*, 479(2):2767–2776.

Yoshiura, S., Shimabukuro, H., Takahashi, K., and Matsubara, T. (2017). Studying topological structure of 21-cm line fluctuations with 3D Minkowski functionals before reionization. *MNRAS*, 465(1):394–402.

Yoshiura, S., Shimabukuro, H., Takahashi, K., Momose, R., Nakanishi, H., and Imai, H. (2015). Sensitivity for 21 cm bispectrum from Epoch of Reionization. *MNRAS*, 451(1):266–274.

Zahn, O., Lidz, A., McQuinn, M., Dutta, S., Hernquist, L., Zaldarriaga, M., and Furlanetto, S. R. (2007). Simulations and Analytic Calculations of Bubble Growth during Hydrogen Reionization. *ApJ*, 654(1):12–26.

Zaldarriaga, M., Furlanetto, S. R., and Hernquist, L. (2004). 21 Centimeter Fluctuations from Cosmic Gas at High Redshifts. *ApJ*, 608(2):622–635.

Zawada, K., Semelin, B., Vonlanthen, P., Baek, S., and Revaz, Y. (2014). Light-cone anisotropy in the 21 cm signal from the epoch of reionization. *MNRAS*, 439(2):1615–1627.

Zheng, H., Tegmark, M., Dillon, J. S., Kim, D. A., Liu, A., Neben, A. R., Jonas, J., Reich, P., and Reich, W. (2017). An improved model of diffuse galactic radio emission from 10 MHz to 5 THz. *MNRAS*, 464(3):3486–3497.

APPENDIX A

KURTOSIS UNCERTAINTY PROPAGATION

The method of uncertainty propagation for one-point statistics is first described in Watkinson and Pritchard (2014). Here, we summarise and expand on their work, deriving uncertainty propagation for the kurtosis in addition to variance and skewness.

To recap, for a 21 cm intensity map with pixel value x_i, mean $\overline{x}$ and N_{pix} pixels, the p-th central moment of the map is defined as,

$$m_p = \frac{1}{N_{pix}} \sum_{i=0}^{N_{pix}} (x_i - \overline{x})^p. \tag{A.1}$$

The variance, skewness and kurtosis are standardisations of 2nd, 3rd and 4th central moments defined as follows.

$$\text{variance:} \quad S_2 = m_2, \tag{A.2}$$

$$\text{skewness:} \quad S_3 = \frac{m_3}{(m_2)^{3/2}}, \tag{A.3}$$

$$\text{kurtosis:} \quad S_4 = \frac{m_4}{(m_2)^2} - 3. \tag{A.4}$$

If every pixel x_i consists of only an independent signal with no noise contribution, we can simply substitute $x_i = \delta T_i$ and $\overline{x} = \overline{\delta T}$ to compute the "true" moments and one-point statistics of the map.

Adding noise n_i with standard deviation σ_i to the signal, each pixel now consists of the signal plus the noise, $x_i = \delta T_i + n_i$, and the noise will bias the moment measurements. An unbiased estimator for the p-th moments ($\hat{m}_p$) can be estimated by averaging the moment equations over noise realisation. Assuming that the noise is Gaussian and independent in each pixel, the averaged noise terms can be rewritten as functions of standard deviation of the noise, using Gaussian moment identities derivable from the following formula,

$$\langle n_i^l \rangle = \begin{cases} (1)(3)(5)\cdots(l-1)\sigma_i^l & \text{if } l \text{ is even} \\ 0 & \text{if } l \text{ is odd} \end{cases} \tag{A.5}$$

where the angle bracket designates an average. Table 3 in this work provide additional identities necessary for the derivation of the kurtosis uncertainty in addition to Equation A.5 and the identities given in the Table A1 in Watkinson and Pritchard (2014).

Using these identities, the estimator variance and covariance of the unbiased estimator of the moments can be derived,

$$V_{\hat{m}_p} = \langle \hat{m}_p {\hat{m}_p}^\dagger \rangle - \langle \hat{m}_p \rangle^2, \tag{A.6}$$

$$C_{\hat{m}_p \hat{m}_q} = \langle \hat{m}_p \hat{m}_q \rangle - \langle \hat{m}_p \rangle \langle \hat{m}_q \rangle, \tag{A.7}$$

and propagate to skewness and kurtosis with Taylor expansion,

$$V_{f(X,Y)} \approx \left(\frac{\partial f}{\partial X}\right)^2 V_X + \left(\frac{\partial f}{\partial Y}\right)^2 V_Y + 2\left(\frac{\partial f}{\partial X}\right)\left(\frac{\partial f}{\partial Y}\right) C_{XY}. \tag{A.8}$$

Here, $f(X,Y)$ is a function of two non-independent variables X and Y. In other word, $X = \hat{m_2}$ and $Y = \hat{m_3}$ for skewness, and $X = \hat{m_2}$ and $Y = \hat{m_4}$ for kurtosis. The uncertainty for each statistic is then just the square root of the estimator variance.

Equations A.9 to A.17 summarise results from Watkinson and Pritchard (2014). For this work, σ_i is assumed to be equal to σ_n in Equation 2.2 in the main text for all pixels. We also simply use N in the main text instead of N_{pix} to emphasise that an individual pixel in an image from an observation may not represent an independent sample.

$$\hat{m}_2 = \frac{1}{N_{pix}} \sum_{i=0}^{N_{pix}} (x_i - \overline{x})^2 - \sigma_n^2 \tag{A.9}$$

$$= m_2 - \sigma_n^2, \tag{A.10}$$

$$\hat{m}_3 = \frac{1}{N_{pix}} \sum_{i=0}^{N_{pix}} (x_i - \overline{x})^3 \tag{A.11}$$

$$= m_3 \tag{A.12}$$

$$= \frac{1}{N_{pix}} \sum_{i=0}^{N_{pix}} (\delta T_i - \overline{\delta T})^3, \tag{A.13}$$

$$C_{\hat{m}_2 \hat{m}_3} = \frac{6}{N_{pix}} m_3 \sigma_n^2, \tag{A.14}$$

$$V_{\hat{m}_2} = V_{\hat{S}_2} = \frac{2}{N_{pix}} (2 m_2 \sigma_n^2 + \sigma_n^4), \tag{A.15}$$

$$V_{\hat{m}_3} = \frac{3}{N_{pix}} (3 m_4 \sigma_n^2 + 12 m_2 \sigma_n^4 + 5 \sigma_n^6), \tag{A.16}$$

$$V_{\hat{S}_3} \approx \frac{1}{(m_2)^3} V_{\hat{m}_3} + \frac{9}{4} \frac{(m_3)^2}{(m_2)^5} V_{\hat{m}_2} - 3 \frac{m_3}{(m_2)^4} C_{\hat{m}_2 \hat{m}_3}. \tag{A.17}$$

We follow the procedure in Watkinson and Pritchard (2014) and are able to confirm their results. In addition, we derive the estimator variance for kurtosis as follows.

First the 4th moment with noise bias is constructed.

$$m_4^{biased} = \frac{1}{N_{pix}} \sum_{i=0}^{N_{pix}} (x_i - \overline{x})^4$$

$$= \frac{1}{N_{pix}} \sum_{i=0}^{N_{pix}} [(\delta T_i - \overline{\delta T}) + n_i]^4. \tag{A.18}$$

Then, we expand the equation and average over the noise.

$$\begin{aligned}
\langle m_4^{biased} \rangle &= \frac{1}{N_{pix}} \sum_{i=0}^{N_{pix}} [(\delta T_i - \overline{\delta T})^4 + 4(\delta T_i - \overline{\delta T})^3 \langle n_i \rangle \\
&\quad + 6(\delta T_i - \overline{\delta T})^2 \langle n_i^2 \rangle + 4(\delta T_i - \overline{\delta T}) \langle n_i^3 \rangle + \langle n_i^4 \rangle] \\
&= \frac{1}{N_{pix}} \sum_{i=0}^{N_{pix}} (\delta T_i - \overline{\delta T})^4 \\
&\quad + 6 \frac{1}{N_{pix}} \sum_{i=0}^{N_{pix}} (\delta T_i - \overline{\delta T})^2 \sigma_i^2 + 3\sigma_i^4 \\
&= \frac{1}{N_{pix}} \sum_{i=0}^{N_{pix}} (\delta T_i - \overline{\delta T})^4 + 6 m_2 \sigma_n^2 + 3\sigma_n^4. \qquad \text{(A.19)}
\end{aligned}$$

The first term in Equation A.19 is simply the 4th moment while other terms arise from the added noise. This implies that an unbiased estimator of the 4th moment is,

$$\begin{aligned}
\hat{m}_4 &= \frac{1}{N_{pix}} \sum_{i=0}^{N_{pix}} (x_i - \overline{x})^4 - 6 m_2 \sigma_n^2 - 3\sigma_n^4 \\
&= m_4 - 6 m_2 \sigma_n^2 - 3\sigma_n^4 \qquad \text{(A.20)} \\
&= m_4 - \frac{3}{2} N_{pix} V_{\hat{m}_2}. \qquad \text{(A.21)}
\end{aligned}$$

Next we derive the estimator variance of the 4th moment. We substitute $\mu_i = \delta T_i - \overline{\delta T}$ and $\kappa = 3 N_{pix} V_{\hat{m}_2}/2$ to simplify Equation A.21 before plugging into Equation A.6 to obtain,

$$V_{\hat{m}_4} = \left\langle \frac{1}{N_{pix}^2} \sum_{i=0}^{N_{pix}} \sum_{j=0}^{N_{pix}} [(\mu_i + n_i)^4 - \kappa] \times [(\mu_j + n_j)^4 - \kappa] \right\rangle - (m_4)^2, \qquad \text{(A.22)}$$

where the second term is reduced to the square of the unbiased 4th moment.

Expanding this expression and moving the noise averaging brackets inside the

summation gives,

$$
\begin{aligned}
V_{\hat{m}_4} =& \frac{1}{N_{pix}^2} \sum_{i=0}^{N_{pix}} \sum_{j=0}^{N_{pix}} \Big[\mu_i^4 \mu_j^4 + 4\mu_i^4 \mu_j^3 \langle n_j \rangle \\
&+ 6\mu_i^4 \mu_j^2 \langle n_j^2 \rangle + 4\mu_i^4 \mu_j \langle n_j^3 \rangle + \mu_i^4 \langle n_j^4 \rangle - \kappa \mu_i^4 \\
&+ 4\mu_i^3 \mu_j^4 \langle n_i \rangle + 16\mu_i^3 \mu_j^3 \langle n_i n_j \rangle + 24\mu_i^3 \mu_j^2 \langle n_i n_j^2 \rangle \\
&+ 16\mu_i^3 \mu_j \langle n_i n_j^3 \rangle + 4\mu_i^3 \langle n_i n_j^4 \rangle - 4\kappa \mu_i^3 \langle n_i \rangle \\
&+ 6\mu_i^2 \mu_j^4 \langle n_i^2 \rangle + 24\mu_i^2 \mu_j^3 \langle n_i^2 n_j \rangle + 36\mu_i^2 \mu_j^2 \langle n_i^2 n_j^2 \rangle \\
&+ 24\mu_i^2 \mu_j \langle n_i^2 n_j^3 \rangle + 6\mu_i^2 \langle n_i^2 n_j^4 \rangle - 6\kappa \mu_i^2 \langle n_i^2 \rangle \\
&+ 4\mu_i \mu_j^4 \langle n_i^3 \rangle + 16\mu_i \mu_j^3 \langle n_i^3 n_j \rangle + 24\mu_i \mu_j^2 \langle n_i^3 n_j^2 \rangle \\
&+ 16\mu_i \mu_j \langle n_i^3 n_j^3 \rangle + 4\mu_i \langle n_i^3 n_j^4 \rangle - 4\kappa \mu_i \langle n_i^3 \rangle \\
&+ \mu_j^4 \langle n_i^4 \rangle + 4\mu_j^3 \langle n_i^4 n_j \rangle + 6\mu_j^2 \langle n_i^4 n_j^2 \rangle \\
&+ 4\mu_j \langle n_i^4 n_j^3 \rangle + \langle n_i^4 n_j^4 \rangle - \kappa \langle n_i^4 \rangle \\
&- \kappa \mu_j^4 - 4\kappa \mu_j^3 \langle n_j \rangle - 6\kappa \mu_j^2 \langle n_j^2 \rangle - 4\kappa \mu_j \langle n_j^3 \rangle \\
&- \kappa \langle n_j^4 \rangle + \kappa^2 \Big] - (m_4)^2. \qquad \text{(A.23)}
\end{aligned}
$$

Applying Gaussian noise identities will reduce the expression to,

$$
\begin{aligned}
V_{\hat{m}_4} =& \frac{1}{N_{pix}^2} \sum_{i=0}^{N_{pix}} \sum_{j=0}^{N_{pix}} \Big[\mu_i^4 \mu_j^4 + 6\mu_i^4 \mu_j^2 \sigma_j^2 + 3\mu_i^4 \sigma_j^4 - \kappa \mu_i^4 \\
&+ 16\mu_i^3 \mu_j^3 \delta_{ij} \sigma_j^2 + 48\mu_i^3 \mu_j \delta_{ij} \sigma_i^4 + 6\mu_i^2 \mu_j^4 \sigma_i^2 \\
&+ 36\mu_i^2 \mu_j^2 (1 + 2\delta_{ij}) \sigma_i^2 \sigma_j^2 + 6\mu_i^2 (3 + 12\delta_{ij}) \sigma_i^2 \sigma_j^4 \\
&- 6\kappa \mu_i^2 \sigma_i^2 + 48\mu_i \mu_j^3 \delta_{ij} \sigma_j^4 + 240\mu_i \mu_j \delta_{ij} \sigma_i^6 \\
&+ 3\mu_j^4 \sigma_i^4 + 6\mu_j^2 (3 + 12\delta_{ij}) \sigma_i^4 \sigma_j^2 + (9 + 96\delta_{ij}) \sigma_i^4 \sigma_j^4 \\
&- 3\kappa \sigma_i^4 - \kappa \mu_j^4 - 6\kappa \mu_j^2 \sigma_j^2 - 3\kappa \sigma_j^4 + \kappa^2 \Big] \\
&- (m_4)^2. \qquad \text{(A.24)}
\end{aligned}
$$

Doing the summation to perform index conversion via δ_{ij}, substituting all $\frac{1}{N_{pix}} \sum_{i=0}^{N_{pix}} \mu_i^k$ terms with the unbiased p-th moments m_p and σ_i with σ_n, re-substituting $\kappa = 3N_{pix} V_{\hat{m}_2}/2 = 6m_2\sigma_n^2 + 3\sigma_n^4$ back to the expression, and cancelling out many terms will yield the estimator variance of the 4th moment,

$$
V_{\hat{m}_4} = \frac{8}{N_{pix}} (2m_6\sigma_n^2 + 21m_4\sigma_n^4 + 48m_2\sigma_n^6 + 12\sigma_n^8). \qquad \text{(A.25)}
$$

$\langle n_i n_j^4 \rangle$	$\langle n_i^5 \rangle = 0$	$(i = j)$	0
	$\langle n_i \rangle \langle n_j^4 \rangle = 0$	$(i \neq j)$	
$\langle n_i^2 n_j^4 \rangle$	$\langle n_i^6 \rangle = 15\sigma_i^6$	$(i = j)$	$(3 + 12\delta_{ij})\sigma_i^2\sigma_j^4$
	$\langle n_i^2 \rangle \langle n_j^4 \rangle = 3\sigma_i^2\sigma_j^4$	$(i \neq j)$	
$\langle n_i^3 n_j^4 \rangle$	$\langle n_i^7 \rangle = 0$	$(i = j)$	0
	$\langle n_i^3 \rangle \langle n_j^4 \rangle = 0$	$(i \neq j)$	
$\langle n_i^4 n_j^4 \rangle$	$\langle n_i^8 \rangle = 105\sigma_i^8$	$(i = j)$	$(9 + 96\delta_{ij})\sigma_i^4\sigma_j^4$
	$\langle n_i^4 \rangle \langle n_j^4 \rangle = 9\sigma_i^4\sigma_j^4$	$(i \neq j)$	

Table 3. Additional Gaussian noise identities for derivation of estimator variance of kurtosis. Please see Table A1 in Watkinson and Pritchard (2014) for more identities.

The estimator covariance between 2nd and 4th moment can be found in a similar manner, resulting in,

$$C_{\hat{m}_2\hat{m}_4} = \frac{4}{N_{pix}}(2m_4\sigma_n^2 + 9m_2\sigma_n^4 + 3\sigma_n^6). \tag{A.26}$$

Finally, we can propagate Equation A.25 and A.26 using Equation A.8 to obtain the estimator variance for kurtosis,

$$V_{\hat{S}_4} = \frac{1}{(m_2)^4}V_{\hat{m}_4} + 4\frac{(m_4)^2}{(m_2)^6}V_{\hat{m}_2} - 4\frac{m_4}{(m_2)^5}C_{\hat{m}_2\hat{m}_4}. \tag{A.27}$$

APPENDIX B

MODELING A FULL-SKY LIGHTCONE

The observable sky at a particular redshift is a sphere in comoving space. No existing 21 cm simulation spans a volume large enough to contain the whole observable sky at the redshifts of interest for reionization. The typical size of a large 21 cm simulation box presently is ∼2 Gpc while a comoving distance to redshift 8.5 ($\nu_{obs} \approx 150$ MHz) is ∼9.3 Gpc. To create a full-sky 21 cm model, we exploit the periodic boundary condition of the 21 cm simulations and effectively tile the simulation volume in comoving space to obtain a sufficiently large volume before gridding on to the sky sphere. The process is repeat at each redshift of interest to create maps for the full lightcone. Figure 32 shows a schematic diagram of our tiling and gridding process.

We start with a suite of theoretical 21 cm cubes from the semi-analytic simulations of Lidz and Malloy (2014). The cubes span the redshift range $9.3 > z > 6.2$, with $\Delta z = 0.1$ steps, representing the universe from $\sim 30\%$ to 96% ionised. The simulation volume is $1\,\mathrm{Gpc}^3$ in a 512^3 pixel box with periodic boundary. We linearly interpolate the simulated 21 cm cubes across redshift to produce new cubes that more-closely match the redshifts observed by HERA in steps of 80 kHz spectral channels between $\sim 139 - 195$ MHz. The interpolation step is not required to construct the lightcone if simulation cubes matching the redshift of interests are available. For each of the redshifts, we tile the interpolated cube with itself in three dimensions to construct an arbitrarily large simulated volume for that redshift. Then, we draw an observable sky at that redshift as a sphere of radius equal to the comoving distance of that redshift from a fixed origin inside the volume and interpolate the nearest neighbouring pixel from the cube to the corresponding HEALPix pixel location on the sphere. We use HEALPix pixel area that is ~ 10 times smaller than the resolution of the simulations (NSIDE=4096) to avoid sampling artefacts. This process is repeated for every observed redshift to produce a suit of full-sky maps that accurately represent the redshifted 21 cm lightcone model.

Before tiling and gridding, we degrade each simulation cube to 128^3 box to reduced computing resources needed to perform the gridding. This step does smooth out the smallest scales in the original simulation cubes and slightly changes its PDF, which more resemble two overlapping Delta functions at $\delta T_b = 0$ and $\delta T_b > 0$ (see Figure 3 for the PDF of our output for a comparison), but all size scales that can be probed by HERA are still retained after the degradation. In addition, hydrodynamic simulations of 21 cm signal, such as in (Ciardi and Madau, 2003) and (Mellema et al., 2006), *do* show Gaussian-like one-point PDFs similar to our results at scales smaller than the original Lidz and Malloy (2014) models. Therefore, we conclude that the highly Delta-function PDFs in the original Lidz and Malloy (2014) models are due to approximations made in their semi-analytic calculations.

Compared to flat-field approximations for tiling and gridding that do not take into account the spherical surface of the sky, our method is equivalent to slicing a simulation cube from different angles and rotational axes and mapping the slices onto a sphere at different locations. Thus, even within the ~ 9 degree HERA fields, we see significantly reduced repetition of spatial structure in the resulted maps in comparison to the flat-

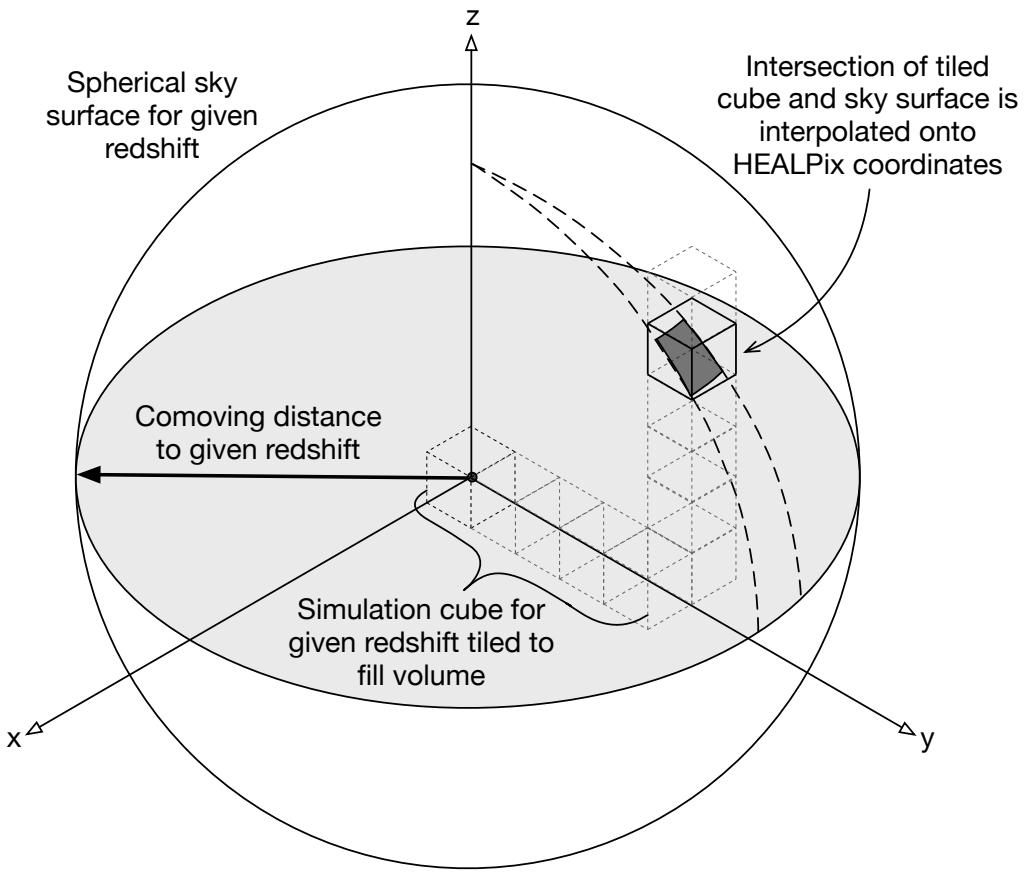

Figure 32. Schematic diagram illustrating the tiling of simulation cubes with periodic boundary conditions to produce a full-sky lightcone. The diagram shows the process for a single redshift. The process is repeated for every observed redshift using an evolved simulation cube for each redshift and the appropriate comoving distance diameter for each redshift. The (x, y, z) coordinates in the diagram represent both the comoving coordinates of the simulation cubes and the Cartesian coordinates of the HEALPix sphere.

field approximation. Figure 33 illustrate this point, where we use the method from Zawada et al. (2014) to produce a standard flat-field lightcone cube and compare it with a lightcone cube produced by gridding onto spherical surfaces. The full-sky HEALPix maps produced with spherical surface gridding preserve one-point statistics of the original simulations, showing changes less than 0.001% of the original values for our simulation sets.

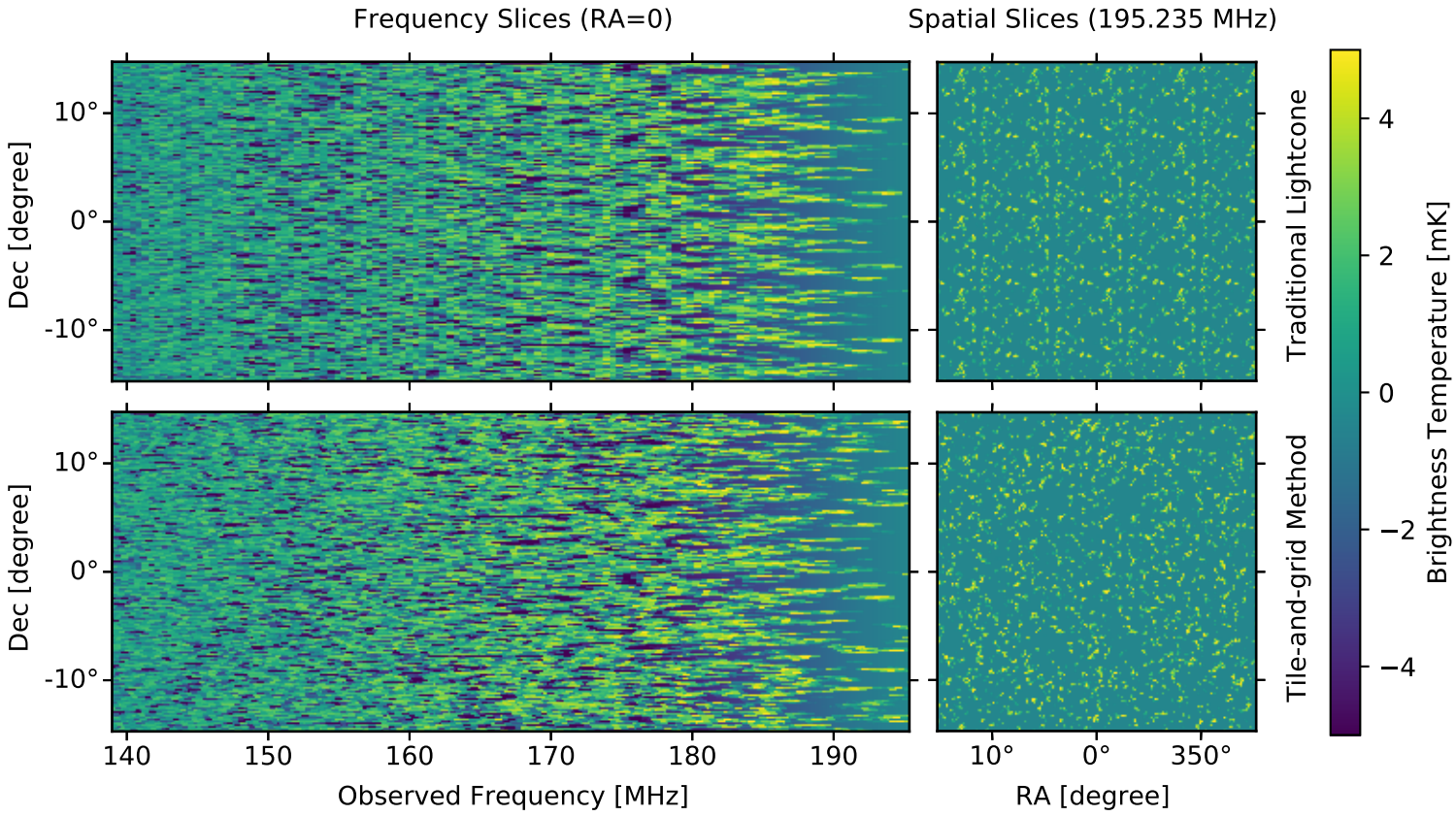

Figure 33. Comparison of flat-field lightcone tiling with our spherical surface projection. Top panel shows the flat-field lightcone and the bottom panel shows the spherical surface lightcone. Even over the relatively small area plotted, repetition of structure is visible in the flat-field lightcone, whereas the spherical surface method results in a random appearance while still preserving the one-point statistics of the original simulation cubes. The flat-field lightcone cube is interpolated from comoving (x, y, z) directly to celestial image coordinates. The two images are identical along Dec=0 degree row.

BIOGRAPHICAL SKETCH

Piyanat (Boom) Kittiwisit was born in Nakhon Ratchasima, Thailand, to Thaninchai and Supapan Kittiwisit. After completing high school in Khon Kaen, Thailand, he received a scholarship from the Development and Promotion of Science and Technology Talent Project to pursue further studies in the United States. He attended Cornell University for his undergraduate studies, where he became active in physics research working on analysis of the data from particle physics experiments at Cornell and Fermilab with Professor Peter Wittich and Professor Ivan Bazarov. Boom graduated with a BA in physics at Cornell before moving to Arizona State University to pursue a graduate study in astronomy, his life-long interest. He was introduced to radio astronomy during the summer of his first year through an international research opportunity in Germany. Afterward, he join Professor Judd Bowman's low-frequency cosmology group to work on simulation and statistical analysis of 21 cm observations. Following graduation from Arizona State, Boom will continue working on 21 cm observations as a postdoctoral fellow at the University of KwaZulu-Natal in Durban, South Africa, and Shanghai Astronomical Observatory in China, before going back to Thailand to contribute his knowledge and experience back to the astronomy community in Thailand.